Effect of Cold Wire TSAW on Weld Geometry and CGHAZ Microstructure of Heavy Gauge X70

by

Tailin Ren

A thesis submitted in partial fulfillment of the requirements for the degree of

Master of Science

in
Materials Engineering

Department of Chemical and Materials Engineering

University of Alberta

Abstract

Heavy gauge (>11 mm wall thickness) X70 pipe is one of the products produced using submerged arc welding (SAW) and is the subject of this thesis. The SAW process offers substantial advantages, including a high deposition rate, deep penetration, and reduced welding times. These attributes are beneficial for welding thick-walled pipes. To increase the process productivity, tandem submerged arc welding (TSAW), containing two or more electrodes, has been developed for welding of line-pipes to achieve a high deposition rate. The use of multi-electrode TSAW may, however, result in an increase in the overall heat input which influences the metallurgical characteristics and mechanical properties of the weld metal (WM) and heat-affected zone (HAZ), especially the coarse grain heat-affected zone (CGHAZ). To minimize the detrimental effects of excessive heat input, cold wire tandem submerged arc welding (CWTSAW) has been developed. This technique can improve the WM and HAZ geometry, mechanical properties, especially fracture toughness, and the microstructure in the CGHAZ. An understanding of the effect of welding parameters on the welding geometry and properties is needed for the application of CWTSAW.

A series of CWTSAW trials were conducted on thick-wall (19.1 mm) American Petroleum Institute (API) X70 steel plates to investigate the effect of cold wire feed speed, heat input, voltage, travel speed, and bevel design on the resulting geometry (e.g., bead width, penetration depth, height of reinforcement area, reinforcement area, bead toe angle, and CGHAZ area), and micro-hardness of the WM and HAZ. The characteristics of weld geometry and hardness were analyzed using three statistical methods including analysis of variance, multiple regression analysis, and Taguchi's signal-to-noise ratio. Charpy V-notch (CVN) impact tests of the weld CGHAZ were conducted. The microstructure of the weld was examined using optical microscopy, scanning

electron microscopy and electron backscatter diffraction for phase identification and grain size measurement.

The statistical results showed that the bevel design had a significant effect on the height of reinforcement area, reinforcement area, bead toe angle, and CGHAZ area but only a minor effect on the weld metal and CGHAZ micro-hardness. Cold wire feed speed had the most dominant effect on the weld metal and CGHAZ micro-hardness profiles, since the cold wire addition altered the local thermal cycle by consuming heat from the molten pool.

The CVN results indicated that the averaged absorbed energy of the CGHAZ was improved by 60% (from 85 J to 137 J) for the sample with a cold wire feed speed of 40 in/min (16.9 mm/s), a travel speed of 50 in/min (21.2 mm/s) and a heat input of 2.9 kJ/mm. The fracture toughness improvement is attributed to a decrease in the actual heat input (2.6 kJ/mm) introduced to the weld and an intermediate cooling rate (36.3 °C/s) in the CGHAZ. However, inferior fracture toughness was obtained if the cold wire feed speed was increased to 80 in/min (33.9 mm/s), due to the relatively fast cooling rate (40.9 °C/s). A cold wire feed speed of 40 in/min (16.9 mm/s) was suitable for the welding process. Additionally, considering the thermodynamic based heat balance calculations for the CWTSAW process, a 20% increase in the welding travel speed was achieved (from 21.2 to 25.4 mm/s) by addition of a cold wire at a feed speed of 40 in/min (16.9 mm/s) while maintaining the improved fracture toughness.

Microstructure analysis showed that refinement of prior austenite grains and ferrite/bainite grains was achieved by cold wire addition. The sample with a cold wire feed speed of 40 in/min (16.9 mm/s) and a travel speed of 50 in/min (21.2 mm/s) had reduced martensite-austenite (MA) constituent fraction and finely dispersed MA constituents, which provided a favorable morphology in terms of fracture toughness. Elongated and massive block MA constituents formed in the sample

with an 80 in/min (33.9 mm/s) of cold wire feed speed, as a result of the faster cooling rate; theses were detrimental to the fracture toughness in the HAZ of welded steel. The prior austenite grain size and MA morphology were significantly influenced by the peak temperature and cooling rate in the CGHAZ by additional cold wire during welding.

Acknowledgements

I would like to express my sincerest gratitude to Dr. Hani Henein for his patient guidance and supervision for my research work. His invaluable inspiration, support and advice helped me to become a better researcher and mentally strong people. My sincerest appreciation also goes to Dr. Douglas G. Ivey for his fundamental and technical guidance in my research work. I would especially like to extend my appreciation to Dr. Barry J. Wiskel for his detailed and continuous guidance for my presentation and writing. This thesis and my whole MSc experience could not have been possible without their support.

I would like to offer my sincere thanks to Mohsen Mohammadijoo (Evraz Inc. NA) for his technical assistance and support for my research work at the R&D division of Evraz inc. NA. I would like to acknowledge and thank Jonas and Aziz for their assistance in my research work at the AMPL. Many thanks also go to my friends and colleagues at the AMPL, Mehdi, Steffen, Lu, Rishav, Vanda, Mingzhang for their advices through discussion. Thank you all!

I also appreciate the assistance of Curtis Finch, Diwakar Parashar and Jon Jackson from Evraz Inc. NA for training equipment, etching process, and conducting Charpy tests, respectively.

I would like to acknowledge the Natural Sciences and Engineering Research Council (NSERC) of Canada, Evraz Inc. NA and TC Energy for finical support.

Finally, I wish to thank my parents for their support and encouragement in my life. Thank you, Mom and Dad, for this most sincere selfless love!

Contents

List of Tables

List of Figures

Chapter 1: Introduction

Heavy gauge (>11 mm wall thickness) X70 pipe is one of the products produced using submerged arc welding (SAW) and is the subject of this thesis. SAW offers substantial advantage, including a high deposition rate, deep penetration, and reduced welding times. These attributes are beneficial for welding thick-walled pipes and plates [1], [2]. To increase productivity, tandem submerged arc welding (TSAW), containing two or more electrodes, has been developed for welding of line pipe to achieve a high deposition rate [2], [3]. The use of multi-electrode TSAW may, however, result in an increase in overall heat input which influences the metallurgical/properties of the weld metal (WM) and heat-affected zone (HAZ), especially in the coarse grain heat-affected zone (CGHAZ). Therefore, the quality of weldments such as toughness and microstructure may deteriorate [4]–[6]. To increase productivity while maintaining the quality of TSAW pipeline products, cold wire tandem submerged arc welding (CWTSAW) was developed [7].

CWTSAW is defined as a TSAW process where an additional electrode with no arc is introduced within the molten pool. The primary objective of involving a cold wire is to increase the deposition rate and decrease the overall heat input into the weld. Previous studies [6], [8]–[11] showed that the cold wire addition was involved in SAW and TSAW process for enhancing welding capabilities and improving weld productivity in terms of reduction in the number of passes, reduced flux consumption and increased deposition rate. Also, CWTSAW produced weldments with qualified weld geometry and improved fracture toughness. Therefore, an understanding of the effect of cold wire addition on the quality and metallurgy of heavy gauge pipeline products is undertaken in this study. The following post welding factors are analyzed:

1) Weld geometrical characteristics (i.e. bead shape and CGHAZ area)
2) Hardness and fracture toughness
3) Grain size and grain misorientation
4) Martensite-austenite (MA) constituent morphologies: fraction, size, shape, size distribution, and inter-particle spacing

This research aims to elucidate:

1. The correlation between CWTSAW process parameters and the weld geometrical characteristics and hardness of the CGHAZ and WM.
2. The effect of cold wire feed speed on the CGHAZ hardness, fracture toughness, and microstructure (i.e., grain size, grain misorientation, and MA morphologies).

A series of CWTSAW trials were conducted on 19.1 mm gauge American Petroleum Institute (API) X70 steel plates to investigate the effect of cold wire feed speed (CWFS), heat input (HI), voltage (V), travel speed (TS) and bevel design (BD) on the resulting geometry (e.g., bead width (BW), penetration depth (PD), height of reinforcement area (HRA), reinforcement area (RA), bead toe angle (BTA), and coarse grain heat-affected zone (CGHAZ) area) and micro-hardness of the WM and HAZ.

The weld geometrical characteristics and hardness were analyzed using three statistical methods including analysis of variance (ANOVA), multiple regression analysis, and Taguchi's signal-to-noise (S/N) ratio. The microstructure of the weld was examined using optical microscopy (OM), scanning electron microscopy (SEM) and electron backscatter diffraction (EBSD) for phase identification, grain size measurement and angle misorientation of ferrite/bainite (α/B) grain boundaries. Hardness measurements were taken from both the HAZ and WM. Charpy impact tests were conducted in the CGHAZ of the weld.

Six chapters (6) are included in the thesis. Chapter 2 contains an introduction to X70 microalloyed steel for pipeline manufacturing and SAW and a review of cold wire addition in TSAW, the Taguchi method for statistical methods and the metallurgical factors associated with fracture toughness and hardness. Chapter 3 includes a description of the steel studied, the composition, welding procedure and experimental/testing techniques employed in the study. Chapter 4 discusses the effect of welding parameters on the measured weld geometrical values and hardness of the WM and CGHAZ using the aforementioned statistical methods. Chapter 5 contains discussion on the correlation between microstructural results and mechanical properties of the weld. Finally, Chapter 6 presents a summary of the conclusions and future work.

Chapter 2: Literature Review

This chapter contains a review of microalloyed steels, weldability, and thermo-mechanical controlled processing (TMCP) in pipeline manufacturing. Conventional submerged arc welding (SAW), tandem submerged arc welding (TSAW), cold wire TSAW (CWTSAW), weld zones, geometric characteristics, and welding parameters are also reviewed. Additionally, a review of Taguchi design and statistical methods such as analysis of variance (ANOVA), multiple regression analysis, and signal-to-noise (S/N) ratio are presented. A description of Charpy V-notch impact testing and a review of metallurgical factors on fracture toughness and hardness are presented as well.

2.1 Microalloyed steels

Microalloyed steels are employed widely in a variety of application, such as pipelines, rail plates, and wind turbines, due to their low cost and outstanding mechanical properties such as high strength, good toughness and improved corrosion resistance [12]–[14]. The general composition of microalloyed steel consists of 0.05 to 0.12 wt.% carbon and less than 0.1 wt.% of microalloying elements such as niobium (Nb), titanium (Ti), and vanadium (V) [15], [16]. These added microalloying elements play important roles in strength enhancement and toughness improvement. For instance, Nb in microalloyed steel promotes grain refinement and precipitate strengthening due to the solubility of Nb in the austenite phase [17]. Therefore, a relatively low amount of microalloying element results in improved mechanical properties are the most common benefits of using microalloyed steels. American Petroleum Institute (API) X70 microalloyed steel with 19.1 mm wall thickness is studied in this thesis and is fabricated by Evraz, Inc. NA.

2.1.1 Weldability

Weldability is the ability of a material to be welded under a given set of conditions. The steel experiences a thermal cycle during welding leading to phase transformations which are dependent on the peak temperature and cooling rate in the HAZ and WM. If the final microstructures contain a brittle phase, such as martensite, the weld is susceptible to brittle fracture. To evaluate this susceptibility, weldability is used to measure cracking resistance such as the resistance to brittle and ductile fracture initiation and propagation after the welding process [18]. Good weldability means a crack is difficult to initiate and propagate.

The carbon equivalent carbon (CE) value, a quantitative factor to evaluate the weldability, is calculated by including the composition of carbon and the rest of the alloying elements. A high concentration of carbon and other alloying elements increases the CE value and hardenability of the steel, which decreases the weldability due to the formation of the martensitic phase [19]. Generally, microalloyed steels contain low carbon content and low alloying element content to reduce the CE value and improve weldability. The CE for the microalloyed steel with low carbon content (< 0.12 wt.%) can be expressed by a weld crack susceptibility index (P_{cm}) [20].

$$P_{cm} = \%C + 5\%B + \frac{\%Ni}{60} + \frac{\%Si}{30} + \frac{\%V}{10} + \frac{\%Mo}{15} + \frac{\%Mn+\%Cu+\%Cr}{20} \quad (2.1)$$

where all components in Equation 2.1 are in wt.%. A low P_{cm} value is considered good weldability and the level of P_{cm} for the studied steel is described in the Chapter 3.

2.1.2 Pipeline Manufacturing

High-performance steel plates are also dependent on the processing condition used in thermo-mechanical controlled processing (TMCP). The objective of TMCP is to refine the microstructure of the steel plate to achieve high strength and improved toughness. A schematic schedule of TMCP is shown in Figure 2.1. Slab reheating is the first step for austenite homogenization and precipitate dissolution. The slab then experiences rough rolling to reduce the austenite grain size; this is followed by finish rolling to obtain pancaked austenite and reduced thickness. The last step is the cooling process to further refine the grain size of the steel and transform its structure. The product obtained from TMCP has a fine microstructure which promotes high strength and toughness [21].

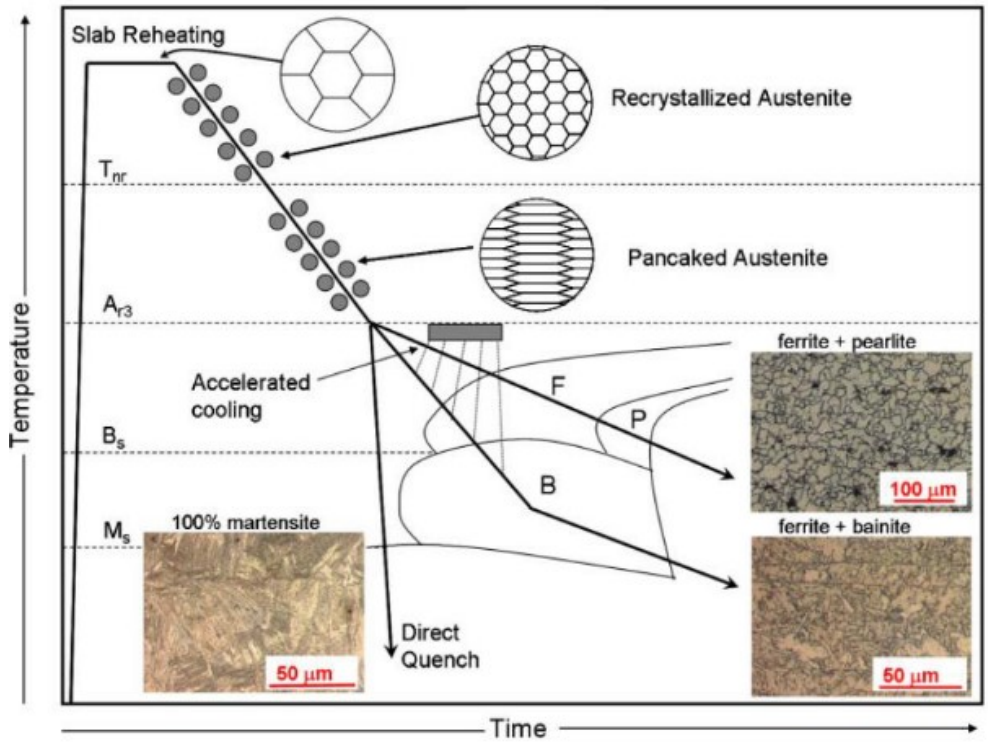

Figure 2.1 Schematic diagram of TMCP [22].

Spiral welding is one of the primary processes to manufacture pipelines. First, the skelp is uncoiled and leveled by passing through a series of rolls, as shown schematically in Figure 2.2 [23]. The spiral angle and skelp width control the thickness of the spiral weld pipe. Then, two welding passes, inside diameter (ID) and outside diameter (OD) welding, are employed to fill the beveled area. Finally, each length of the weld goes through either radiographic inspection or ultrasonic testing to check for weld defects. The advantages of spiral welded pipe are wall thickness uniformity and flexible welding operation with continuous production.

Spiral welding is a high productivity process using high heat input; one example is SAW, which can be used to produce thick-walled spiral welded pipe (heavy gauge pipeline). The pipeline industry has explored manufacturing of heavy gauge pipeline using microalloyed steel. Heavy gauge pipelines are beneficial for long distance transmission and high operating pressures. Evraz Inc. NA recently updated their steel mill to meet the increased demand and a major achievement was the production of 19.1 mm thick X70 pipe meeting quality specifications [2]. Therefore, the SAW process is necessary for the fabrication of heavy gauge pipeline and is reviewed in the following subsection.

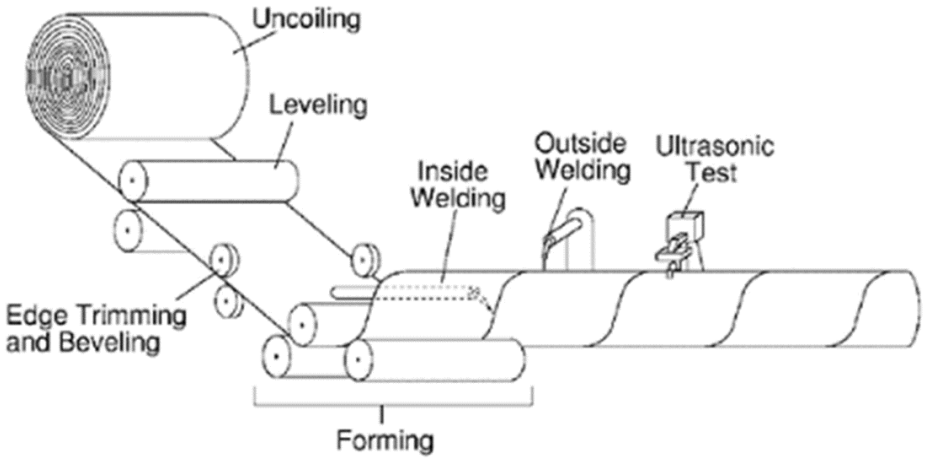

Figure 2.2 Schematic diagram of a spiral weld pipe [23].

2.2 Submerged Arc Welding (SAW)

Submerged arc welding (SAW) is a traditional arc welding process which occurs by heating a steel plate and a consumable electrode with an arc. A solid granular flux is utilized in the process which protects the weld pool from the ambient atmosphere to avoid the formation of oxides. High current densities using large diameter electrodes are possible with SAW, which allows for high deposition rates and deep penetration [24]. In addition, a less visible arc and lower fume generation, due to the granular flux protection, make the process an appropriate welding process from an environmental and safety perspective. Therefore, SAW is employed extensively in pipe manufacturing, pressure vessel fabrication, and ship building [25].

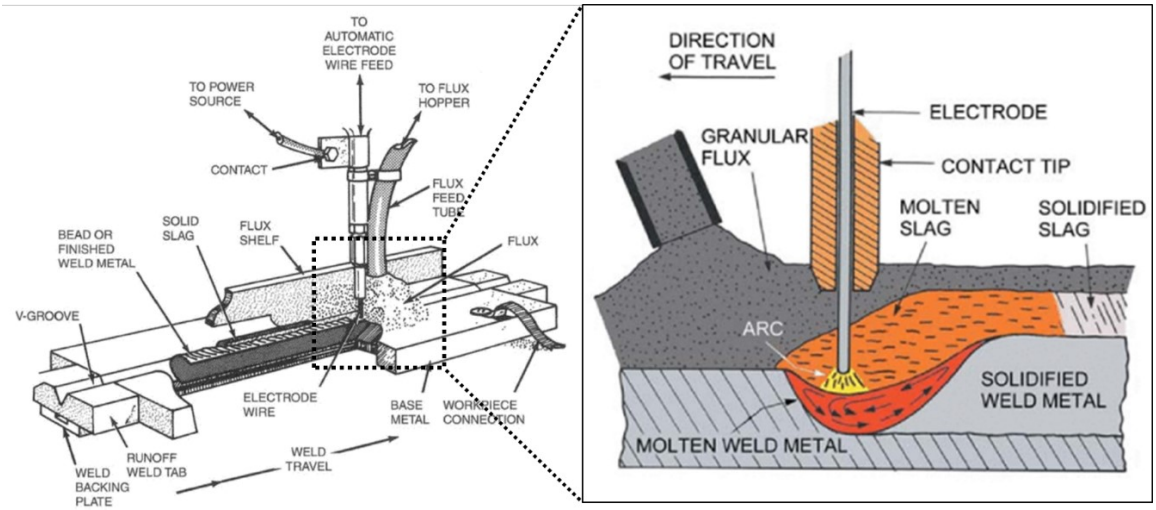

Figure 2.3 Schematic of SAW[24] [25].

2.2.1 Tandem Submerged Arc Welding (TSAW)

SAW offers substantial benefits including a high deposition rate, good penetration, and reduced welding times. These attributes are beneficial for welding thick-walled plates [1], [2]. As discussed in Section 2.1.2, the production of heavy gauge pipeline is being explored in the pipeline industry, due to the desire to increase pipeline productivity for long distance transmission under high pressures. Typically, increased welding productivity can be obtained by using multiple electrodes (more than one and up to five electrodes) to increase the deposition rate in the SAW process; this is referred to as TSAW. The number of electrodes varies with the thickness of the base steel and the objectives for different pipeline industrial applications. Figure 2.4 exhibits a schematic of the TSAW process with five electrodes to weld a thick-walled pipe (11 mm or greater) [26]. In addition to the flexibility of employing multiple electrodes, another advantage of TSAW is the ability to control arc type for each electrode independently which means that the polarity of each electrode can be adjusted for different welding conditions. The effect of electrode polarity on penetration and selection of polarity for CWTSAW are discussed in Section 2.2.3.

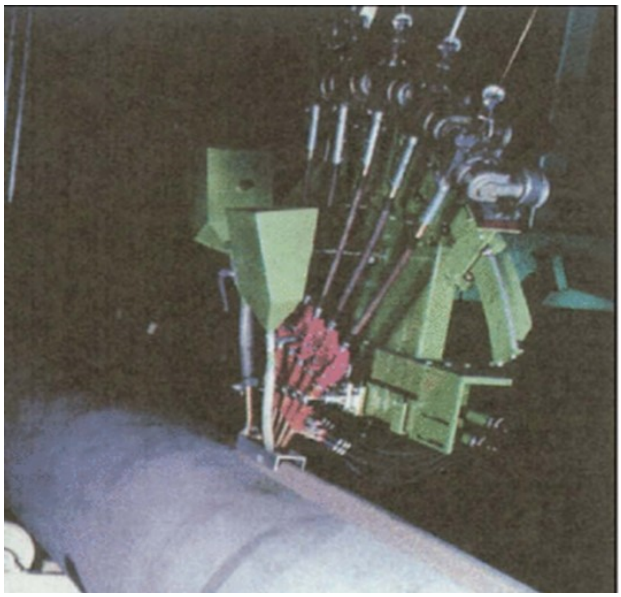

Figure 2.4 Image of TSAW with five electrodes [26].

The use of multi-electrode TSAW may, however, result in an increase in the overall heat input of the weld, which can affect the metallurgy/properties of the weld metal (WM) and heat-affected zone (HAZ), especially the coarse grain heat-affected zone (CGHAZ). Suryana et al. [27] and Yan et al. [28] reported that the higher heat input in the SAW process resulted in a larger HAZ region area and width and increased grain size. Moeinifar et al. concluded that a high heat input TSAW process contributed to inferior toughness in the HAZ and the formation of a hard and brittle phase, i.e., martensite-austenite (MA) constituents, in CGHAZ [4]. According to Kozuki at al. [21], improvement in toughness and refinement of grain size in the HAZ of heavy wall line pipe can be achieved by decreasing the overall heat input by using small diameter wire for the lead electrode in TSAW. In summary, weld quality, in terms of toughness and microstructure, may deteriorate due to the high heat input of SAW and TSAW. To increase productivity, while maintaining the quality of TSAW pipeline products, cold wire tandem submerged arc welding (CWTSAW) was developed [6].

2.2.2 Cold Wire TSAW (CWTSAW)

CWTSAW is a welding process where an additional electrode is introduced into the molten pool with no arc. The primary objective for involving a cold wire is to increase deposition rate and decrease the overall heat input into the weld, while maintaining the properties of the weld [6], [8], [9], [11], [29]–[32].

This method was first developed by Mruczek et al. [6] for a single wire SAW process for enhancing welding capabilities and improving weld productivity by increasing the deposition rate. Figure 2.5 shows the setup of the lead electrode and cold wire in SAW. Mruczek et al. compared the single wire SAW process with the cold wire addition SAW process for X65 steel in terms of deposition rate, Charpy V-notch testing, and micro-hardness. The welding parameters were identical for both tests with the only difference being the cold wire addition. The results showed that the cold wire addition SAW process improved the deposition rates for the root pass and fill pass by 43% and 37%, respectively. The absorbed energy in the WM increased by 22%. The transverse hardness profile was higher for the cold wire for both the HAZ and WM, as compared to the conventional SAW weld. These data were a good indicator that cold wire addition in the single wire SAW process improved the deposition rate and enhanced the fracture toughness by reducing the overall heat input into the weld. The overall heat input is reduced due to the heat consumption by cold wire addition in the molten pool which results in the low peak temperature in the weld and HAZ. The amount of deposited material with the low heat input and a reduction in the arcing time cause the formation of the smaller molten pool. In an addition, the refinement of prior austenite grains (PAG) and reduction of MA constituents in HAZ due to the reduced overall heat input are contributed to enhancing fracture toughness [30]. These specified advantages of using cold wire retain adequate weld geometry and properties without increasing heat input. The effect of cold wire addition in TSAW (multiple wires), studied by other researchers, is reviewed next.

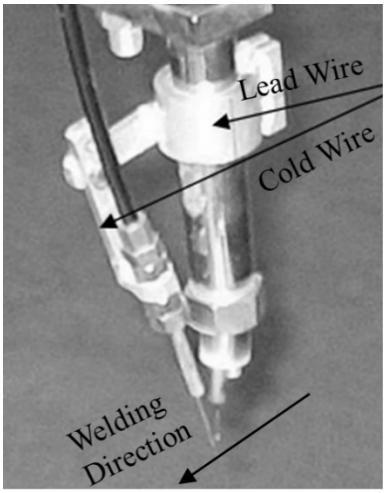

Figure 2.5 Setup of lead wire and cold wire in SAW [6].

Júnior et al. studied the effect of cold wire in TSAW of duplex stainless steels (12 mm thickness) on the amount of dilution and corrosion resistance [29]. Reduced dilution and fewer localized corrosion pits were observed, indicating improved corrosion resistance. Ramakrishnan et al. published several studies related to cold wire addition, such as butt welds of pressure vessels [9], comparison of three or four wires in SAW welds [10], and fracture toughness for narrow groove SAW processes [11]. The addition of a cold wire led to a 40% reduction in the number of passes and a 30% saving in flux consumption.

Mohammadijoo et al. [8] applied cold wire addition to the TSAW (CWTSAW) process of an intermediate thickness X70 line pipe (13.4 mm) with the setup of electrodes and cold wire are shown in Figure 2.6. The cold wire was placed at a lagging position adjacent to the trail electrode, where it consumes excess heat from the weld pool. In addition, placing the cold wire at a lagging position angle of 63° resulted in an overall improvement in the weld geometry and mechanical properties [8]. Cold wire addition at 25.4 cm/min feed rate showed a reduction in the fraction of MA constituents and a finer distribution of MA in the CGHAZ. This phenomenon was related to the reduced actual heat input and prior austenite grains (PAG) size, which led to an improvement in fracture toughness in the HAZ [31]. The 25.4 cm/min cold wire feed speed also resulted in refined grain size and high misorientation angle distribution of the ferrite and bainite boundary (>15°) in the CGHAZ, as determined from EBSD analysis [30]. In summary, the work contributed several achievements through cold wire addition including decreased overall heat input, increased deposition rate, increased travel speed, improved fracture toughness, refined grain size, and

reduced MA volume fraction for intermediate gauge X70 line pipe steels. The fundamental relationship between weld parameters and characteristics is reviewed next.

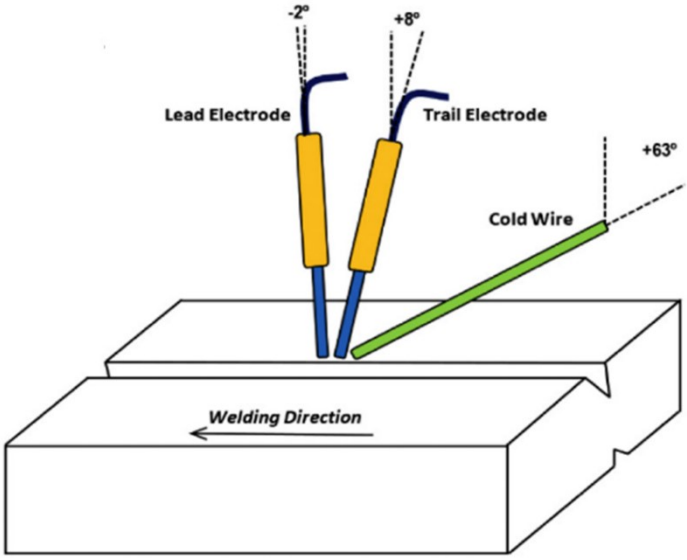

Figure 2.6 Schematic of CWTSAW [32].

2.2.3 Welding Metallurgy

This section includes a description to the weld zones and characteristics of weld geometry in welding metallurgy.

Weld Zones

A typical weld zone is consisted of the WM, HAZ and base metal (BM). Four (4) regions in the HAZ are the coarse grain HAZ (CGHAZ), fine grain HAZ (FGHAZ), inter-critical HAZ (ICHAZ) and sub-critical HAZ (SCHAZ), as shown in Figure 2.7.

The WM is defined as a mixture of the melted filler electrode and BM when the temperature is above the melting point of the weldment. The WM has good mechanical properties such as enhanced strength and improved toughness in micro-alloyed steels welding. The CGHAZ exhibited the inferior properties relative to the remaining weld zones, especially toughness [33]. The CGHAZ temperature range (1100 - 1450 °C) in Figure 2.7 is higher than the rest of the weld zones which promotes the austenite grain growth and precipitate dissolution. In temperature range (A_{C3} - 1100 °C) of the FGHAZ, the fine grain microstructure is shown due to the nucleation of the

grains. The amount of the precipitates is not dissolved completely in the FGHAZ since the peak temperature is lower than the peak temperature in the CGHAZ. The temperature range of the ICHAZ is between A_{c1} and A_{c3}. The SCHAZ undergoes no microstructure transformation.

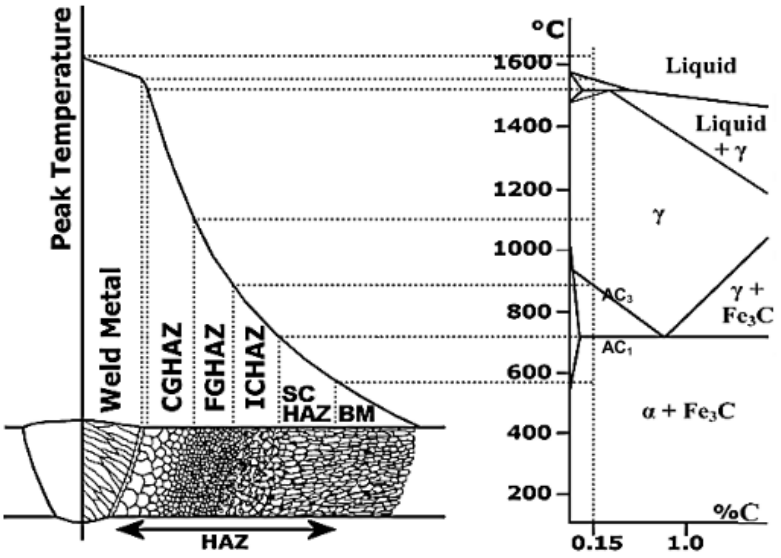

Figure 2.7 Schematic diagram of different regions of the heat-affected zone of a 0.15 wt.% C steel formed during single pass welding. The temperature range in each region is correlated to the Fe-Fe_3C phase diagram [33].

Characteristics of Weld Geometry

Typical characteristics of weld geometry are shown in Figure 2.8. In this thesis, the reinforcement shape (area and height), bead width, penetration depth and CGHAZ area are necessary to define here for the further analysis on the correlation between the welding parameters and the characteristics of welding geometry. The influence of welding parameters on the characteristics of weld geometry is reviewed fundamentally in Subsection 2.2.4.

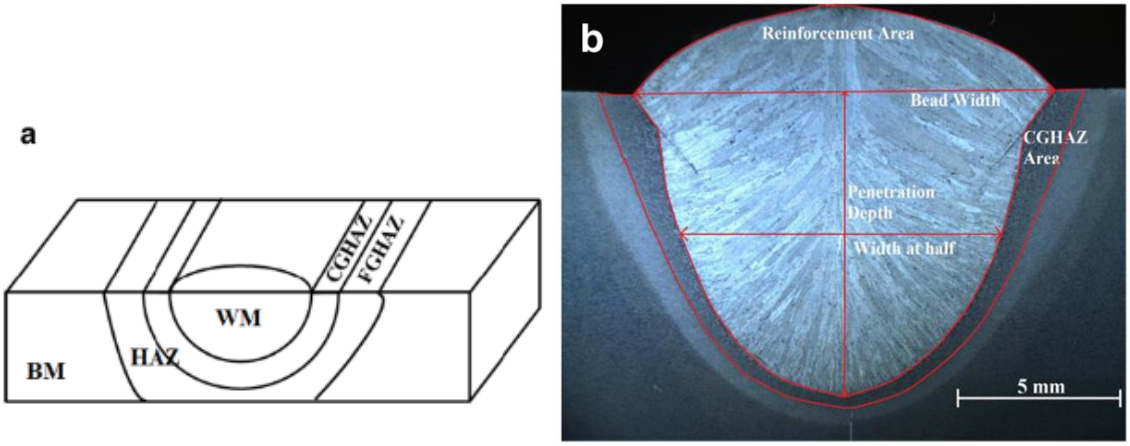

Figure 2.8 a) Schematic of the weld indicating different weld zones. b) Optical macrograph of X70 steel welded by CWTSAW indicating the geometric characteristics [8].

2.2.4 Welding Parameters

In the current section, the main variables related to both the SAW and CWTSAW processes are presented. The effect of input variables on weld geometrical variables is discussed. In addition, a review of cold wire parameters, such as wire position and feeding angle, is discussed.

Current

As one of the primary parameters in the SAW process, current (I) plays an important role in the penetration profile. It is generally accepted that a high current density promotes a deep penetration depth [25], [34]. An increase in current flow creates a magnetic field to produce a plasma jet force and this force accelerates the droplets of the electrode falling into the weld pool [35]. Additionally, welding current controls the base metal melted. An excessively high current density, however, results in electrode waste forming extra reinforcement and distortion of the weld. Conversely, too low a current input may result in incomplete penetration or lack of weld fusion [36]. Therefore, a suitable range of welding current is considered necessary when multiple electrodes and cold wire addition are involved.

Voltage

Voltage (V) is the pressure from an electric circuit pushing electrons and ions through a conducting loop. This parameter has little effect on the electrode deposition rate, but it is mainly responsible for weld bead shape and weld appearance, as shown in Figure 2.9. A high arc voltage

leads to a wider bead shape; however, it can also lead to undercutting due to the increased arc length [36], [37]. Mohammadijoo et al. [8] reported that the lead and trail electrode voltage in the CWTSAW process influences the bead width and penetration depth of the weld and both voltage parameters provide around 50% effective contribution to the bead shape.

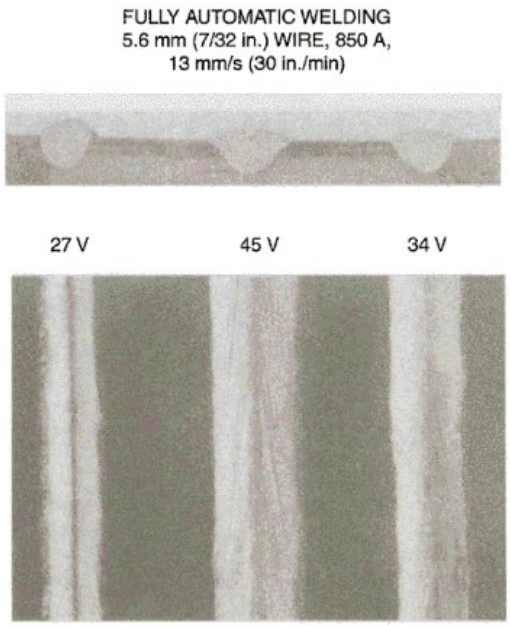

Figure 2.9 Effect of arc voltage on weld bead shape and penetration [34].

Travel speed

Travel speed (TS) is defined as the welding rate and is used to describe the productivity of a welding process. A higher TS reduces the heat input per unit length of the weld and filler metal per unit length of the weld, so that less weld reinforcement is formed [34]. The effect of travel speed on weld bead shape and penetration is exhibited in Figure 2.10. TS has a greater influence on penetration of the weld than current. A narrow weld with little penetration is the main outcome of a high TS and may produce a risk of undercutting, pores, root defects, poor fusion and magnetic blow effect (uncontrolled deflection of the arc current) [37]. In a CWTSAW process, one study reported that a 25% increase in TS, with a 58 cm/min cold wire feed speed, resulted in ~12% increase in deposition rate, while the geometry, appearance, and properties of the weld were retained [7].

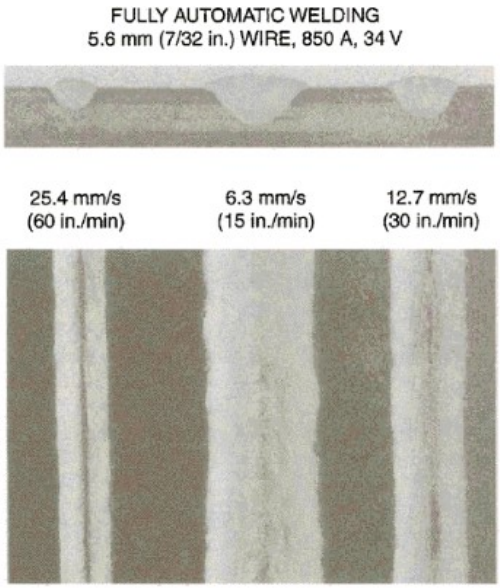

Figure 2.10 Effect of travel speed on weld bead shape [34].

Heat input

The interplay of current, voltage, and travel speed influences the welding process by changing weld bead geometry. As discussed in previous subsections, these parameters have their own effects on the weld. In the arc welding process, heat is the form of energy coming from electricity. This heat energy is a combination of current, voltage and welding time (travel speed). The relationship among the three parameters to produce welding energy is called heat input (HI) [27].

$$\mathrm{HI} = \mu * \frac{60*\mathrm{V}*\mathrm{I}}{1000*\mathrm{TS}} \tag{2.2}$$

where HI, V, I and TS are heat input (kJ/mm), voltage (V), current (A), and travel speed (mm/min), respectively. The weld heat efficiency (μ) is different for various arc welding processes. For SAW, μ is equal to 0.9 - 1.0 [27].

The effect of HI on the weld bead shape is also considerable. An increase in HI generates an increase in weld characteristics such as penetration depth, reinforcement area and bead width. This trend is expected since the voltage and current could increase and the travel speed may decrease, as discussed previously. In addition, the deposition rate also can be increased by

increasing HI, which is important for productivity. An increase in HI, however, produces a wider heat affected zone (HAZ) which contains the CGHAZ, i.e., the region with inferior properties. Therefore, HI, which depends on A, V, and TS, is necessarily used in statistical analysis.

Polarity

Polarity is defined as the direction of electron flow during the process of electrode consumption. Direct current electrode positive (DCEP) and direct current electrode negative (DCEN) are two conventional polarities using in a consumable electrode welding, and are schematically shown in Figure 2.11. DCEP is described as involving electron flow from the base metal to the electrode. Conversely, electrons flowing away from the electrode to the base metal is referred to as DCEN.

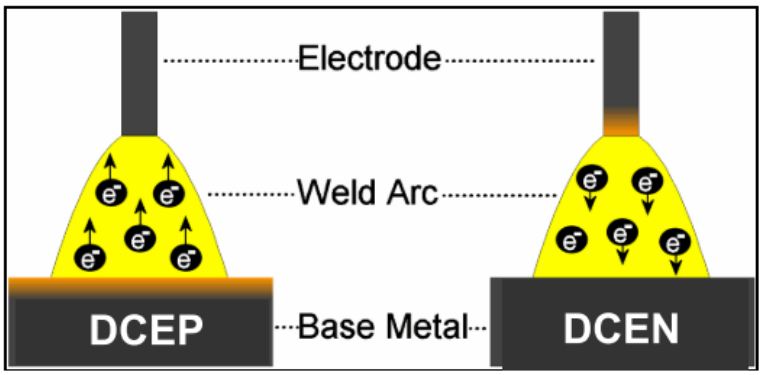

Figure 2.11 Schematic of polarity for a welding process of a consumable electrode [38].

The polarity influences the bead shape, as shown in Figure 2.12. The use of DCEP polarity increased penetration depth and area, since additional base metal is melted. The use of DCEN increases reinforcement height and area due to the additional electrode consumed.

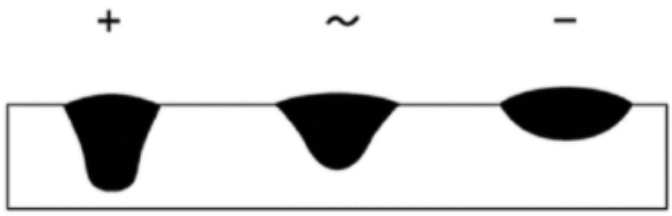

Figure 2.12 Effect of wire polarity on bead shape [37]

Another common welding power source uses sinusoidal alternating current (AC), which can balance the pros and cons of DCEP and DCEN [39]. Sinusoidal AC; however, spends insufficient time at the peak current (Figure 2.13-a) leading to incomplete penetration and deficient deposition rates [39]. Fisher et al. [39] studied square wave AC (ACSQ) polarity to overcome the difficulties in the use of sinusoidal AC. Arc stability was achieved as well as increased dwell time at the peak current (Figure 2.13-b).

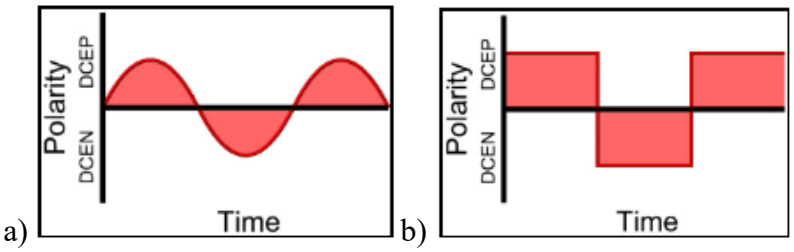

Figure 2.13 a) Current waveforms for sinusoidal AC and b) square wave AC [38].

The power source for each electrode in TSAW affects the penetration and deposition rate separately [40], [41]. Pepin et al. [38] studied the polarity in a TSAW process with two electrodes and they reported that using DCEP for the first electrode provided deep penetration into the joint root face, while higher deposition rates and minimal arc blow were achieved using ACSQ for the second electrode. This configuration is used for the current study, and is described in Chapter 3.

Wire Position

The feed position of the filler wire has a considerable effect on the penetration and bead shape of the weld, as shown in Figure 2.14. The forehand wire feeding position may result in a wider bead and shallower penetration than the other positions, such as vertical and backhand positions. The arrangement needs more consideration for TSAW or cold wire addition TSAW.

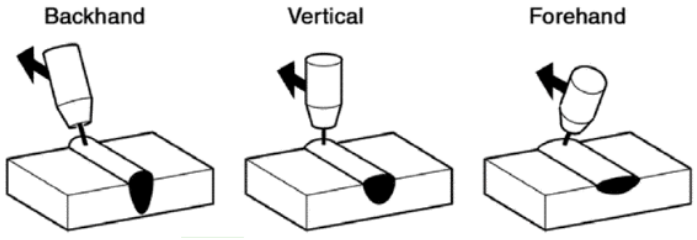

Figure 2.14 Effect of wire angle position [37]

Mruczek et al. [6] developed cold wire technology into the SAW process to increase the deposition rate and they discovered the effect of cold wire feed position in terms of lagging and leading configuration (Figure 2.15). The lagging configuration for the cold wire resulted in a greater penetration compared with the leading position since a slightly higher heat input was required. Additionally, Mohammadijoo et al. [8] reported a similar finding for cold wire addition in the TSAW process. A cold wire fed at the lagging position close to the trail electrode caused no reduction in the penetration. The consumption of heat from the lead electrode when the cold wire is at the leading position is considered the reason for a slightly shallower penetration.

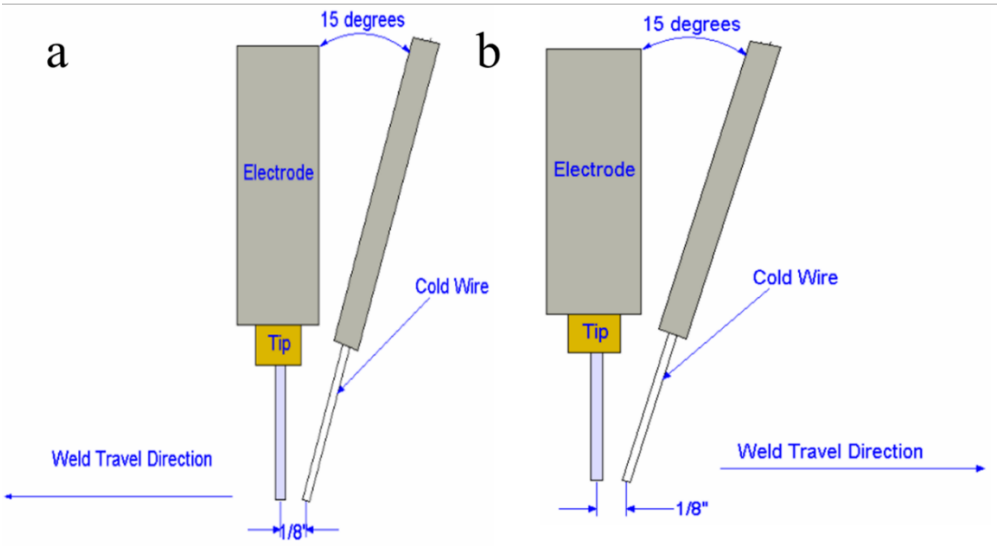

Figure 2.15 Cold wire position: a) lagging configuration and b) leading configuration [6].

2.3 Design of Experiments

This section contains an introduction to the Taguchi method and a description of the designed steps for an orthogonal array (OA). Three statistical analyses, including analysis of variance (ANOVA), multiple regression analysis, and signal-to-noise (S/N) ratio, are also reviewed.

2.3.1 Taguchi Method

The Taguchi method is a statistical technique used to analyze and improve manufacturing processes by conducting the minimum number of tests [42], [43]. Taguchi replaced a full factorial experiment with an orthogonal array (OA). The number of tests in an OA is dependent on the number and input levels of independent variables (welding parameters) and is insensitive to noise variables such as ambient temperature and atmospheric pressure. After conducting OA tests, the response factors (weld characteristics) are correlated with each level of independent variable based on the assumptions of the Taguchi method. The assumptions imply that the main effects of the independent variables on response factors are separable, which means there are no interactions among the independent variables [42], [44], [45].

The Taguchi method has been used in numerous studies on optimizing the welding process. Tarng et al. [44] determined the optimal welding parameters of the SAW process with a small number of tests utilizing Taguchi analysis. Sarkar et al. [46] employed Taguchi techniques to analyze the effective contribution of bead geometry on tensile strength and validated the results with confirmatory SAW tests process. Shahraki et al. [45] predicted the weld geometry for the SAW process in terms of nano powder thickness, voltage, current and welding speed using Taguchi analysis ss. Additionally, Mohammadijoo et al. [8] used the Taguchi method to optimize the CWTSAW process for intermediate gauge X70 steels by defining significant welding parameters and suitable levels of the process parameters.

The steps for designing an OA experiment using the Taguchi method are listed in the following [42], [47], [48]:

1. Selection of independent variables

The selection of independent variables is the most important step in the Taguchi method. Identifying the variables which may influence the response variables requires comprehensive

fundamental knowledge of the product and process. Feedback from all the members in the project was utilized to generate a robust design.

2. Selection of level settings for each independent variable

After the selection of the independent variables, the number of level settings for each independent variable is selected based on the linear or nonlinear relationship between the variables and response factors. If response factors are a linear function of the variables, the number of level settings may be 2. If the function is not linearly related, three, four, or higher level settings are selected. The levels for independent variables also relies on the judgment and experience of the researchers associated with the project.

3. Selection of OA

Once the selection of independent variables and level settings are completed, the minimum number of tests is fixed based on the total number of degrees of freedom. A commercial software, called Minitab, provided guidelines for the selection of the OA in this study.

4. Selection of level values for each independent variable

The actual level values for each variable needs to be selected. The level range of variables may correlate with the performance of dummy tests before the OA experiments. It is noted that the significance and the effective contribution of the variables strongly depend on the level values. This step requires careful consideration.

5. Performance of the designed OA

Once the above steps are finished, the selected OA is conducted following the level combinations.

6. Analysis of the measured results

The response factors measured for each test in the OA are further analyzed. Three statistical methods are used in this thesis and are reviewed in the following sections.

2.3.2 Analysis of Variance (ANOVA)

Analysis of variance (ANOVA) is a standard statistical technique to evaluate the significance of the independent variables to the response factors in the group of tests [41], [43], [46], [49]. Generally, ANOVA is utilized to understand the significance of independent variables (welding parameters) on the response variables (measured characteristics). Sarkar et al. used ANOVA to investigate the influence of SAW process parameters on the weld geometrical results such as penetration, bead width, and reinforcement [46]. Additionally, Lafdani et al. ensured suitable fitting in a quadratic model by using ANOVA to eliminate insignificant terms [49]. There were several quantities that were computed and displayed in a standard ANOVA table. In this thesis, two representative quantities, P value and sum of squares (SS), are described.

The P value is a measure of the probability that an observed difference occurred randomly in the data. Specifically, a lower P value indicates the independent variables are more statistically significance for the observed difference. Sarkar et al. [46] and Lafdani et al. [49] calculated P values at a 95% confidence level to select statistically significant parameters based on lower P values (less than 0.05). The SS is a measure of the deviation of the experimental data from the mean value of the data and the effective contribution for the independent variable is obtained by the total SS for that response factor [43]. Mohammadijoo et al. [8] used the total SS for the effective contribution of welding parameters on bead shape profile and the objective was to understand the effect of welding parameters on weld geometry at the first stage of developing a welding process.

2.3.3 Multiple Regression Analysis

Multiple regression analysis is a crucial tool in statistical modeling. The use of regression analysis is the estimation of the relationships between a dependent variable and one or more independent variables, namely predictors. The empirical equation is the most important result from the regression analysis, which consists of independent variables with their coefficients. Several aspects, such as the number of predictors, input levels of independent variables, and the predicting power in empirical equations need more consideration at the beginning of the analysis [50].

Multiple regression analysis is generally categorized by a linear and nonlinear regression model which depends on the objectives of the simulation and the relationship between the dependent variable and independent variables. Gowthaman et al. [51] and Sailender et al. [52] studied the effect of welding parameters, such as welding current and wire feed rate on the

dependent variables such as bead width, micro-hardness of the WM, and the size of HAZ, using linear multiple regression (MLR) analysis. In addition, Mohammadijoo et al. [8] studied the effects of parameter interactions in the welding process containing eight parameters using the nonlinear regression model (three order multiple regression analysis). A good correlation between predicted values and measured values is beneficial for the process in industry.

2.3.4 Signal-to-Noise (S/N) Ratio Analysis

The use of signal-to-noise (S/N) ratio in the analysis of the data can provide process improvement by optimizing independent parameters. The most important information received from the S/N ratio is optimized parameters based on the desired quality of the measured response variables. Any deviation in the response variables can be reduced using the desired quality of S/N ratio. The most common S/N ratios are lower-the-better and higher-the-better quality for the response variables, according to Equation 2.3 and 2.4 [53]**:**

$$\eta_{(\text{lower-the-bettter})} = -10\log_{10}\left(\frac{1}{n}\sum_{i=1}^{n} y_{ij}^2\right) \tag{2.3}$$

$$\eta_{(\text{higher-the-bettter})} = -10\log_{10}\left(\frac{1}{n}\sum_{i=1}^{n} \frac{1}{y_{ij}^2}\right) \tag{2.4}$$

where η is the S/N value and y_{ij} are the experimental values of the ith response characteristics in the jth test and n is the number of tests.

The use of the S/N ratio is combined with the use of ANOVA and multiple regression analysis in an orthogonal array designed by the Taguchi method. Mason et al. [52] and Shahverdi et al. [45] applied S/N ratio analysis to the optimization of SAW parameters and the suitable levels of SAW process parameters were selected based on the strategy where a higher S/N ratio for a parameter level generated an optimal effect on the response characteristics. The detailed use of the S/N ratio in this thesis is presented in Chapter 4. A review of Charpy V-notch impacted testing is presented in Section 2.4.

2.4 Fracture Toughness

This section includes a review of Charpy V-notch (CVN) fracture toughness. In addition, the metallurgical effects from prior austenite grains (PAG) and martensite-austenite (MA) constituents on fracture toughness are reviewed.

2.4.1 Impact Fracture Toughness

Impact fracture toughness is a measure of the fracture resistance of a material based on absorbed energy during failure. The evaluation of impact fracture toughness is significant for ferritic or body-centered-cubic (BCC) alloys since a transition from ductile to brittle behavior is exhibited when the samples are tested over a range of temperatures [54]. At temperature above the transition temperature, a ductile mechanism (dimple features) is dominant and the sample absorbs a relatively large amount of energy in failure (Figure 2.16-a). At temperatures below the transition temperature, a brittle fracture mechanism (cleavage fracture) occurs and appears as river patterns on the fracture surface (Figure 2.16-b). A relatively small amount of energy is absorbed during brittle failure, which represents poor fracture resistance. Within the transition range, the fracture is a mixture of ductile and brittle behavior and the sample transitions from ductile to brittle at a temperature range. This is defined as the ductile to brittle transition temperature (DBTT). In the pipeline industry, low temperature fracture toughness and DBTT are two primary factors to evaluate the quality of pipeline products. A detailed description of Charpy Impact testing is presented in Subsection 2.4.2.

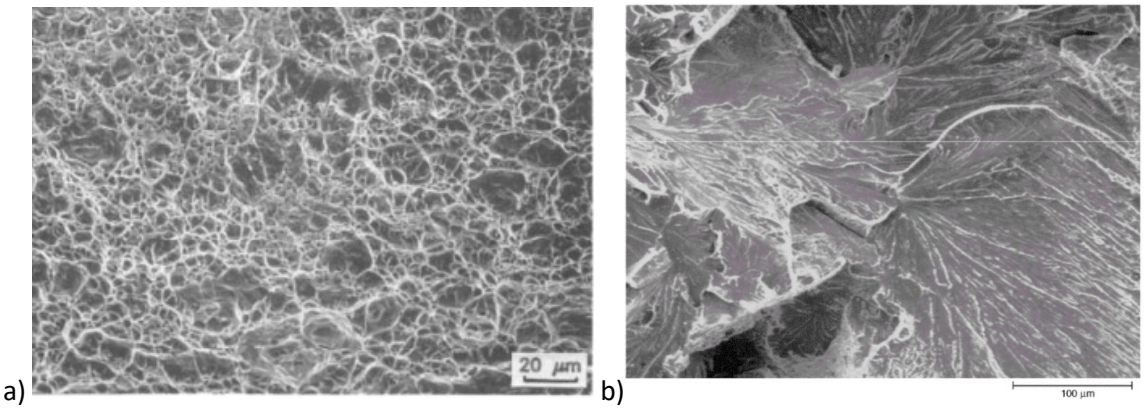

Figure 2.16 SEM secondary electron (SE) micrographs of a) a ductile fracture surface [55] and b) a cleavage fracture surface [54].

The setup for Charpy impact testing is schematically shown in Figure 2.17. A standard notched sample is placed on a support and is broken by a pendulum with a fixed weight. Firstly, the pendulum is released from a fixed height. The pendulum then impacts the sample. After fracturing the sample, the pendulum rises to a height equivalent to the kinetic energy remaining in the pendulum. The height difference before the release of the pendulum and after striking the sample is related to the energy absorbed by the sample during fracture [56]. The CVN testing used in this thesis is presented in Chapter 3 and a detailed discussion of CVN results of CWTSAW samples is presented in Chapter 5. A review of toughness and metallurgical factors is presented next.

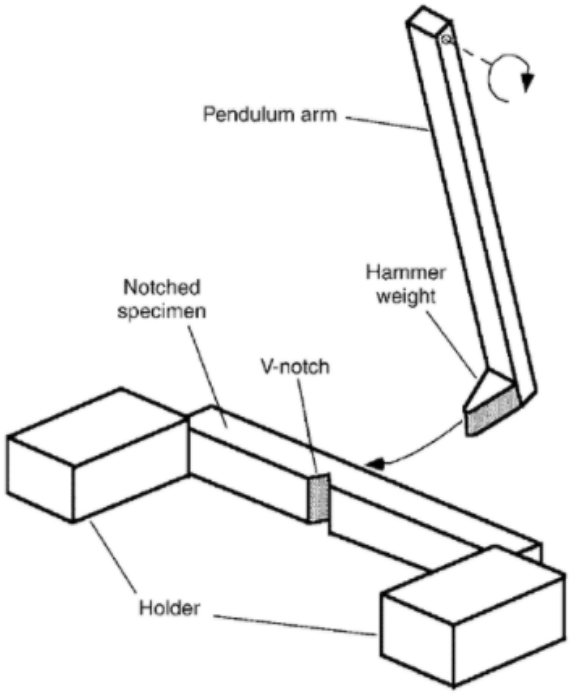

Figure 2.17 Schematic of impact testing in Charpy impact toughness testing [54]**.**

2.4.2 Effect of Prior Austenite Grains (PAG) on Fracture Toughness

Prior austenite grains (PAG) are the existing austenite grains prior to the transformation to ferrite, bainite or martensite [57][58][59]. In welding metallurgy, PAG size influences the phase transformation and MA constituents when the steel experiences different thermal cycles, such as different peak temperatures and cooling rates. The properties of the weld are also affected. The effect of PAG size on the properties and microstructure of welds associated with pipeline steel is reviewed.

Roberts et al. [58] studied the effect of peak temperature on different tool steels and confirmed that the PAG size increased as the austenitizing temperature increased (Figure 2.18). No information about the correlation between PAG size and MA constituents was presented.

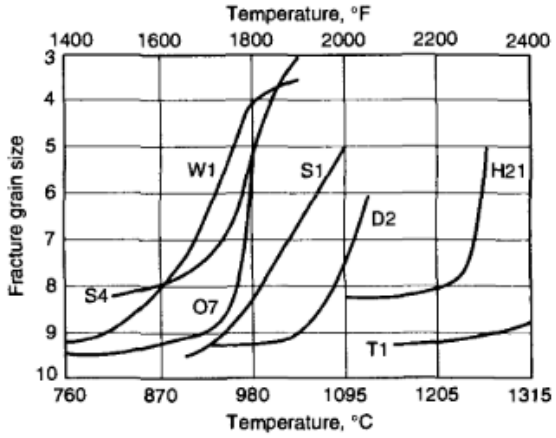

Figure 2.18 Austenitic grain size as a function of austenitizing temperature for various tool steels [58].

Lan et al. [60] studied the effect of peak temperature (austenitizing temperature) on the PAG size and reported that increasing the peak temperature promoted the growth of PAG (Figure 2.19). A smaller PAG size can lead to a combined increase in strength, ductility and toughness due to refinement of bainite and the stability of retained austenite.

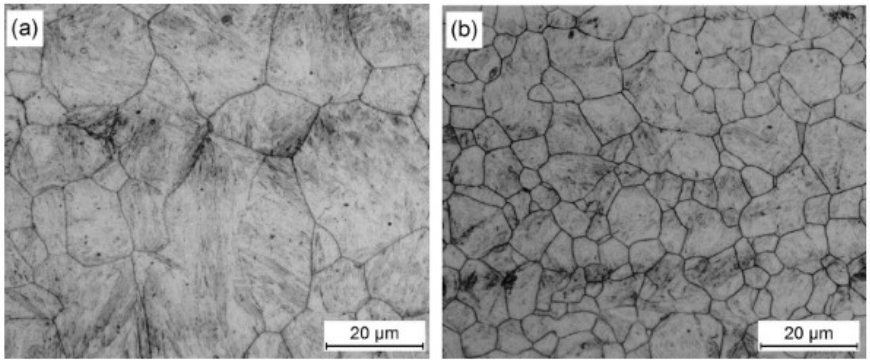

Figure 2.19 Austenite grain structure for the two austenitizing conditions: a) 1100 °C and b) 950 °C [60].

Li et al. [61], [62] studied the effect of PAG size on the morphology of MA constituents and correlated this with fracture toughness for various peak temperatures and a constant cooling rate. The highest peak temperature resulted in the largest PAG and necklacing MA (elongated MA) was formed at PAG boundaries, leading to the highest fraction of MA and inferior toughness. Conversely, a finer PAG size resulted in smaller MA constituents and better toughness.

Khan et al. [63] investigated the correlation between heat treated microstructure and cooling rate for a constant peak temperature; the cooling rate ranged from 6 to 1 °C/s. The PAG size was similar in all cases because of the constant peak temperature. The highest cooling rate of 6 °C/s resulted in the formation of martensite, bainite, and ferrite with minimal pearlite. More pearlite and less martensite formed in samples with cooling rates from 4 to 1 °C/s. The lowest toughness was obtained for the sample containing the highest fraction of martensitic, i.e., the highest cooling rate of 6 °C/s. Additionally, the best fracture toughness was obtained for the sample with a cooling rate of 4 °C/s. Therefore, the PAG size was mainly determined by the peak temperature and phase transformation was sensitive to the cooling rate profile. The correlation between MA and PAG is reviewed in Subsection 2.4.3.

2.4.3 Effect of Martensite-Austenite (MA) Constituents on Fracture Toughness

The low temperature fracture toughness of the HAZ, especially the CGHAZ, is crucial for pipeline products since the fracture toughness may deteriorate due to the high heat input and a local thermal cycle of a welding process, such as submerged arc welding (SAW) [64], [65]. The deterioration of the fracture toughness is significantly related to local brittle zones (LBZ). Coarser

LBZ promote the initiation and propagation of brittle fracture [66]. Specifically, the LBZ consists of MA constituents forming within or along PAG boundaries [67]. Fracture toughness deterioration was studied by Kim et al. [55] and they reported that cleavage initiation points formed at martensitic islands (Figure 2.20-a). Additionally, Li et al. [68] showed that necklacing MA at PAG boundaries created LBZ which are detrimental to fracture toughness (Figure 2.20-b). A description and illustration of the metallurgical effects of PAG and MA constituents are given below.

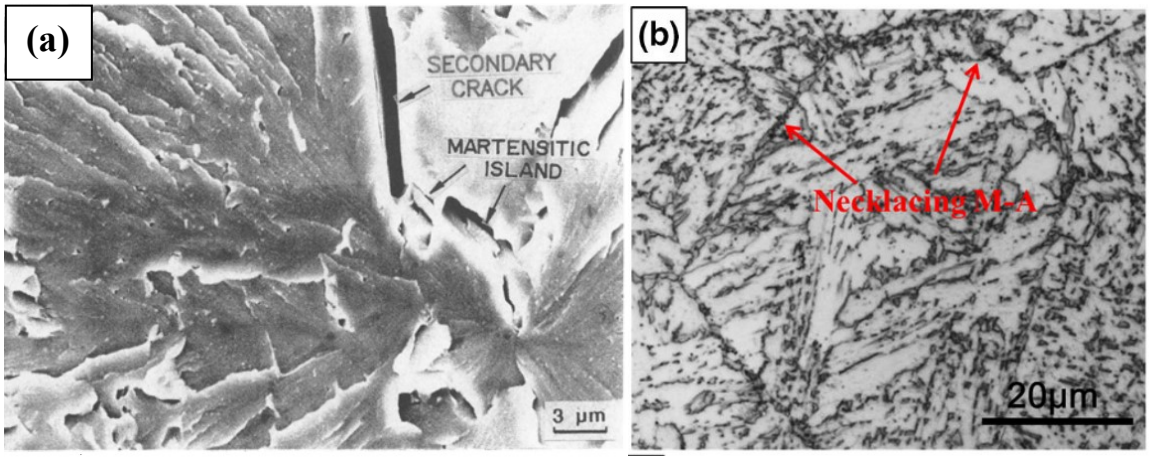

Figure 2.20 a) A cleavage initiation point at a martensitic island [55] and b) necklacing MA of LBZ [68].

Martensite-austenite (MA) constituents consist of a combination of martensite and retained austenite which forms during rapid cooling. Retained austenite is austenite not fully decomposed into ferrite/carbide or martensite [69]. The effect of morphology and MA fraction on fracture toughness has been extensively studied. The crucial studies based on the correlation between PAG size and morphology of MA constituents are reviewed.

Based on the PAG size effect on martensitic transformation, Fisher et al. [70] developed a geometrical partitioning model and reported that the volume fraction of martensite formed in the early stages of transformation is proportional to the cube of the austenite grain size, due to the dependence of the martensite start temperature (Ms). Yang et al. [71] developed a model of geometrical partitioning into a quantitative framework to estimate the variation of Ms as a function of PAG size.

In terms of fracture behavior, Zhang et al. [72] reported that elongated MA constituents in the CGHAZ promote crack initiation and this type of MA constituent tends to form along PAG boundaries. Eroglu et al. [57] recommended that a reduced volume fraction of MA constituents with fine distribution is favorable for fracture toughness. Shome et al. [73] and Lambert et al. [66] [67] confirmed the relatively fast cooling rate in the HAZ facilitated the formation of carbon enriched, martensite which significantly increased the MA constituent fraction.

Overall, the peak temperature and cooling rate in the CGHAZ are primary factors influencing the PAG size and MA constituents. However, thermal cycles in real weld tests are complicated when a cold wire is involved, since the peak temperature and cooling rate are influenced concurrently. The review of the published works in this subsection provides background information which is utilized in the discussion in Chapter 5.

2.5 Hardness

This section includes a review of the influence of martensite-austenite (MA) constituents and cooling rate on the hardness profile in the HAZ.

2.5.1 Effect of Martensite-Austenite (MA) Constituents on Hardness

Hardness, which is influenced by the MA fraction, is a crucial factor for the evaluation of cold crack resistance [7], [74]–[76]. MA contains both the martensitic matrix and retained austenite. It is generally accepted that a high amount of martensitic matrix leads to higher hardness. Li et al. [62] reported that high carbon martensite in MA is characterized by high hardness. Zhu et al. [75] studied the microstructural changes in simulated CGHAZ and reported that the hardness increases as the fraction of MA increases (Figure 2.21). Also, Mohammadijoo et al. [7] confirmed that a higher fraction of MA constituents contributed to higher hardness and inferior toughness in the CGHAZ. The effect of cooling rate on hardness is reviewed in Subsection 2.5.2.

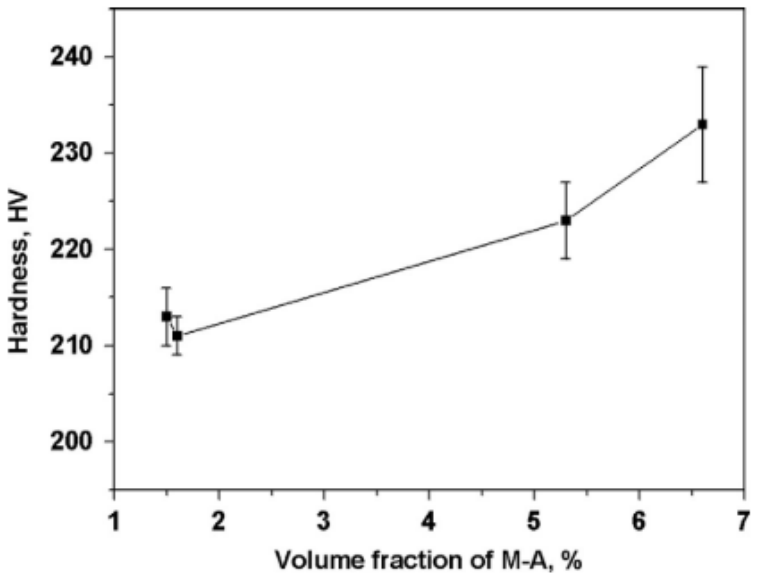

Figure 2.21 Correlation of hardness with total fraction of MA [75].

2.5.2 Effect of Cooling Rate on Hardness

An accelerated cooling rate significantly influences the HAZ microstructures and increases hardness, which increases the susceptibility to cold cracking [7], [66], [67], [77]. Lambert et al. [66], [67] studied simulated HAZ using the time from 800 ºC to 500 ºC ($\Delta t_{8/5}$) to evaluate the cooling rate and reported that decreased $\Delta t_{8/5}$, which represents a fast cooling rate, results in increased hardness due to a higher fraction of MA. The presence of MA being correlated with a rapid cooling rate is generally accepted due to the nature of the martensite phase transformation. Mohammadijoo et al. [7] calculated the cooling rate based on $\Delta t_{8/5}$ to correlate CGHAZ hardness and reported that faster cooling rate resulted in increased hardness combined with inferior toughness. In addition, Mohammadijoo et al. [7] reported that lower hardness values due to the slower cooling rate were generally associated with improved toughness since the formation of ferrite was promoted and the amount of MA constituents was reduced. Li et al. [77] confirmed this behavior by showing that a 13 s time for $\Delta t_{8/5}$ resulted in the lowest hardness reading, but the absorbed energy in failure decreased (Figure 2.22). More discussion on the correlation of microstructure and properties of the weld (toughness and hardness) is presented in Chapter 5.

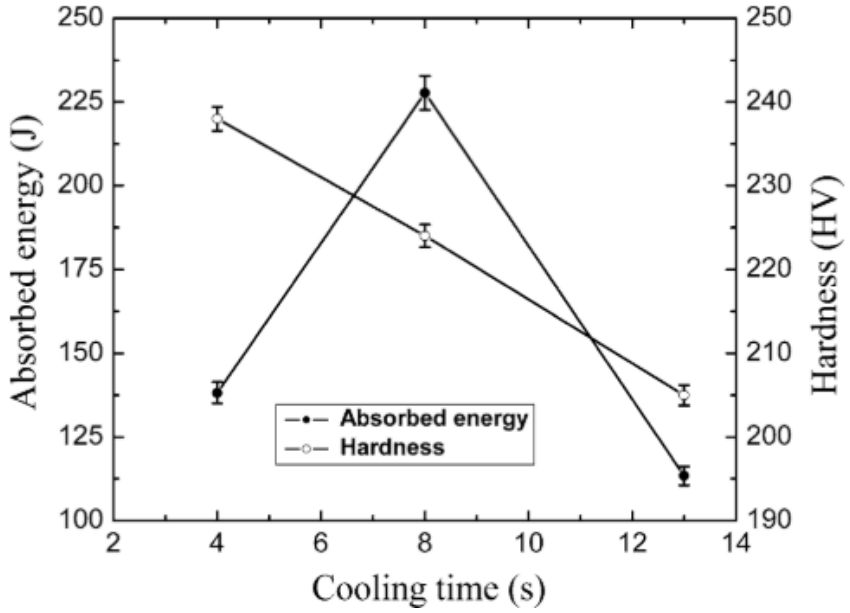

Figure 2.22 Change of absorbed energy and hardness versus the cooling time from 800 ^{0}C and 500 ^{0}C ($\Delta t_{8/5}$) [77].

2.6 Summary

This section summarizes the findings of the Literature Review. First, a summary of microalloyed steels in terms of weldability and pipeline manufacturing is presented. Then effect of a cold wire addition to the SAW and TSAW process and the associated welding parameters are summarized. In addition, Taguchi method and statistical methods, including ANOVA, MRA, and S/N Ratio, are summed up. Finally, the effects of metallurgical factors, including PAG size, MA constituent, and LBZ, on fracture toughness and hardness are summarized.

2.6.1 Microalloyed Steels

The selection of microalloyed steels using in pipeline manufacturing relies on good weldability, high strength, improved corrosion resistance, and toughness. Specifically, the CE value is employed to evaluate weldability. The API X70 microalloyed steel with 19.1 mm wall thickness is the subject of the thesis. The TMCP process refines microstructure to achieve high strength and improved toughness. From a welding quality point of view, steel plates maintaining good properties, or even improved properties, after a welding process are necessary.

2.6.2 Cold Wire Tandem Submerged Arc Welding (CWTSAW)

SAW in spiral welding manufacturing is a suitable application for the fabrication of >11 mm gauge pipeline due to its good penetration and deposition rate. To increase the deposition rate, TSAW containing multiple electrodes (up to five electrodes) is used to fabricate thick-walled pipelines. The number of multiple electrodes and the power source of each electrode (i.e., AC or DC polarity) are flexible and controllable in the TSAW process. The quality of weldments such as toughness and microstructure modification; however, may deteriorate due to the high heat input of the use of multiple electrodes. Therefore, the primary objective of cold wire addition in TSAW is to increase the deposition rate and reduce heat input while maintaining the properties of the weld.

Cold wire addition in the SAW and TSAW processes produces an increased deposition rate of up to 43% and improved toughness for both the HAZ and WM. In addition, asuitable cold wire feed speed promotes grain size refinement, high misorientation angle (> 15°) of grain boundaries, and low MA volume fraction in the CGHAZ.

The interplay of current, voltage, and travel speed influence the weld bead shape independently. Heat input incorporates all three effects. An increase in heat input generates an increase in penetration depth and reinforcement shape. In addition, the use of DCEP on the first electrode and ACSQ on the second electrode achieves deep penetration, high deposition rate, and minimal arc blow in TSAW. Lastly, placing the cold electrode at the lagging position leads to deep penetration and increased deposition rate in the CWTSAW process.

2.6.3 Taguchi and Statistical Methods

The Taguchi method is a common technique used in optimization when numerous independent factors (weld parameters) and response factors (weld characteristics) are involved in the process. The Taguchi method consists of a series of steps that are suitable for parametric study at the beginning of this thesis work, including the analysis of the correlation of parameters and characteristics, by setting up an orthogonal array.

ANOVA analysis is beneficial for the understanding of parameter significance on characteristics by using P values. MRA predicts the correlation between parameters and measured characteristics. The combination of ANOVA and MRA is beneficial for this thesis work to statistically understand the effect of cold wire addition. S/N ratio analysis provides the optimized setup of weld parameters based on the designed criteria.

2.6.4 Fracture Toughness

The deterioration in fracture toughness is significantly related to the PAG size and the presence and morphology of the MA constituent in LBZ. The PAG size is a function of peak temperature in the HAZ and influences the morphology and volume fraction of MA during the early phase transformation stage. Cleavage fractures initiate and propagate at elongated MA particles and a high volume fraction of MA may deteriorate the fracture toughness of the weld. In addition, the presence and morphologies of MA are sensitive to the cooling rate, since the M_s varies with PAG size and peak temperature in the HAZ. Therefore, the peak temperature and cooling rate influence the PAG size and morphology of the MA constituent concurrently.

2.6.5 Hardness

Hardness is related to the fraction of the hard phases in the HAZ, especially the MA constituent. The fraction of the MA is significantly influenced by the cooling rate. Increasing the cooling rate increases the amount of MA, contributing to an increase in hardness. A hardness profile is necessary to assist in associating fracture toughness with microstructure to evaluate the effect of welding parameters on the weld.

2.6.6 Research Contribution

In this thesis, an ANOVA and multiple regression analysis are done to correlate welding parameters and weld geometrical characteristics in heavy gauge (19.1 mm) X70 line pipe steels. The setup for heat input of the lead and trail electrodes, travel speed, and bevel design are then optimized using S/N ratio analysis. Conventional TSAW and CWTSAW using optimized levels of parameters are compared in terms of micro-hardness, fracture toughness, and metallurgical perspectives under various cold wire feed speeds. Furthermore, the productivity and actual heat input analysis in the CWTSAW are presented.

Chapter 3: Materials and Welding Procedure

This chapter includes a description of the X70 micro-alloyed steel used in the welding trails and a summary of the cold wire tandem submerged arc welding (CWTSAW) procedure. A description of weld sample preparation, electrode composition and welding parameters is also included. The techniques used to analyze the welds include optical microscopy (OM) for geometric analysis, scanning electron microscopy (SEM) for phase identification, hardness and Charpy V-notch impact testing are described.

3.1 Microalloyed Steel

The steel welded in this study is X70 skelp. The skelp is 19.1 mm thick with the composition shown in Table 3.1. The levels of each element are typical for an X70 steel although the wt.% Mn level is on the lower end. The wt.% Ti level is 0.015% which is lower than the typical value for an X70 steel. The studied X70 microalloyed steel was fabricated by Evraz Inc. NA through thermo-mechanical controlled processing (TMCP) [2].

Table 3.1 Composition and carbon equivalency of X70 steel (wt.%)

C	P	S	Mn	Si	N	V+Mo+Ti+Nb	Cu+Ni+Cr+Al+Ca	Fe	P_{cm}
0.04	0.01	0.003	1.32	0.28	0.007	0.34	0.63	bal.	0.16

For a steel with a low carbon level, the carbon equivalency, P_{cm}, can be calculated according to the Ito-Bessyo Equation 3.1 [20]. P_{cm} is expressed in terms of the carbon equivalent value to estimate hardenability, since carbon produces hardness more efficiently than the other elements. A high P_{cm} value indicates that the steel has a high hardenability and low weldability, since high hardenability increases the risk of heat-affected zone (HAZ) cracking. According to American Welding Society (AWS) guide D1.7, a P_{cm} value lower than 0.35% is considered good weldability which means the weldment will have a low risk of weld cracking such as cold cracking and hydrogen-induced cracking [78]. The level of P_{cm} for the studied X70 steel (Table3.1) is 0.16%.

$$P_{cm} = \%C + \frac{\%Si}{30} + \frac{\%Mn+\%Cu+\%Cr}{20} + \frac{\%Mo}{15} + \frac{\%V}{10} + \frac{\%Ni}{60} + 5\%B \quad (3.1)$$

3.2 Welding Procedure

This section describes the weld bevels and type of electrodes used, the welding setup and parameters, and the experimental welding matrix developed for this study.

3.2.1 Weld Bevel Specifications

Weld samples were fabricated and machined in two different bevel designs. Figure 3.1 compares the two bevel types used. Each bevel is generated on the same thickness of weld skelp, but the cross-sectional areas are different. For instance, the 60° bevel with 4.5 mm depth has a 12 mm^2 cross-sectional area while the 90° bevel with 5 mm depth has a larger cross-sectional area, 25 mm^2. The quantitative description of the bevel specification is convenient for the representation of the two bevel types in statistical analysis of Chapter 4.

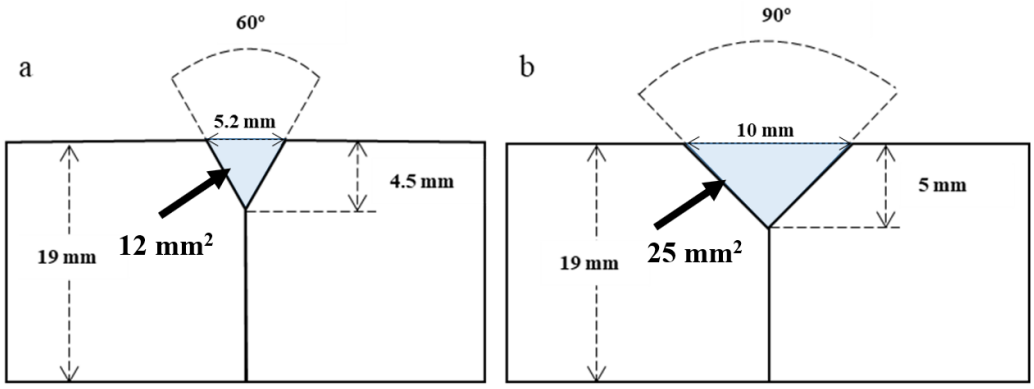

Figure 3.1 Schematic view of bevel specifications.

3.2.2 Type of Electrodes

According to American Welding Society (AWS) A5.17/A5.23 and Bavaria, Germany EN756/EN14295 classifications, a 4 mm diameter BA-S2Mo solid wire was selected for the electrodes and cold wire. The composition is shown in Table 3.2.

Table 3.2 Composition of the weld electrode (wt.%)

C	P	S	Mn	Si	Mo	Ni	Cr	Cu
0.1	0.007	0.01	1.04	0.1	0.56	0.02	0.03	0.03

3.2.3 *CWTSAW Welding Setup*

The CWTSAW process, shown in Figure 3.2, consisted of lead, trail and cold electrodes. The actual welding set up (Figure 3.2a) shows that the electrically cold electrode is located at a lagging position relative to the trail electrode. All welding process configurations, including the position angle of all electrodes, stick length and distance between tip of lead and trail electrode, are shown in Figure 3.2b.

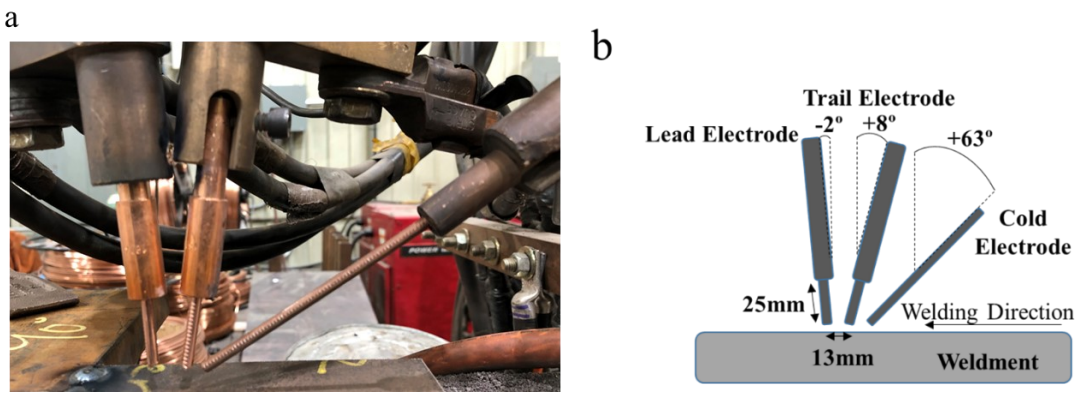

Figure 3.2 Setup for CWTSAW process: a) Actual welding set up and b) schematic view of fixed welding variables.

The power source to operate the lead and trail electrodes using constant current is shown in Table 3.3. Direct current and alternating current were selected for the lead and trail electrodes, respectively, generating deep penetration of the weldment and a high deposition rate. There was no power source for cold electrode. As a basic feature in submerged arc welding (SAW), a consumable granular flux is needed to shield the welding pool and to fill the bevel area. The BF6.5 consumable flux produced by Bavaria in Germany, according to EN 760, is used in CWTSAW process.

Table 3.3 Power source for the electrodes in CWTSAW

Electrodes	Power source
Lead	Direct current electrode positive (DCEP)
Trail	Square wave alternating current (ACSQ)
Cold	Not available

3.2.4 Welding Parameters

The four fundamental welding parameters are current, voltage, travel speed and feed speed of electrodes. For the CWTSAW process, there are additional welding parameters based on the use of multiple electrodes. However, in order to understand the effect of heat input on the weldments and to avoid too many welding tests, the current of the lead and trail electrodes was not varied independently, and the feed speed of the trail and lead electrodes was kept constant. The heat input (HI) and voltage (V) are key welding parameters and the current was calculated and set during welding according to Equation 3.2 [8].

$$\mathrm{HI}\left(\frac{\mathrm{kJ}}{\mathrm{mm}}\right) = \frac{\eta \cdot \mathrm{V} \cdot \mathrm{I}}{1000} \cdot \mathrm{TS} \tag{3.2}$$

where HI, V, I and TS represent heat input, voltage, current and travel speed. The arc efficiency (η) is the range of 0.9-1.0 for SAW [8].

Seven welding parameters with mixed levels, including five main welding parameters such as heat input and voltage of lead and trail electrodes and travel speed, were selected for CWTSAW tests. These are shown in Table 3.4. The heat input, voltage and travel speed are fundamental and crucial parameters for a welding process which are necessary to include. Moreover, the cold wire parameter and bevel specification parameter are cold wire feed speed (CWFS) and bevel design (BD), respectively. CWFS and BD were selected to study the effect of the cold wire addition and varied bevel types on weld characteristics and hardness. Only CWFS is a four-level welding parameter and the others are two-level.

Table 3.4 CWTSAW tests parameters and input levels

Symbol	Process parameter	Notation	Unit	Level 1	Level 2	Level 3	Level 4
A	Cold wire feed speed	CWFS	mm/s	16.9	25.4	33.9	42.3
B	Heat input of lead electrode	HIL	kJ/mm	1.6	1.8	-	-
C	Heat input of trail electrode	HIT	kJ/mm	1.3	1.5	-	-
D	Voltage of lead electrode	VL	V	33	36	-	-
E	Voltage of trail electrode	VT	V	34	37	-	-
F	Travel speed	TS	mm/s	21.2	23.3	-	-
G	Bevel design	BD	mm^2	12	25	-	-

3.2.5 Experimental Table

In Chapter 4, Taguchi analysis is employed for the parametric study of CWTSAW. The main advantage of Taguchi analysis is the use of small number of welding tests, which is more economical and effective than using a factorial design [42]. Based on six parameters with two levels and one parameter with four levels, an L16 orthogonal array (OA) was designed using Taguchi analysis and is shown in Table 3.5. The L16 array comprised 16 weld tests and each level of the parameters appeared the same number of times in each column. The weld geometrical values were measured for all 16 weld tests and analyzed using statistical methods. Additionally, a welding table of three confirmatory tests is shown in Table 3.6. These confirmatory tests were used to validate the linear trend between the measured and predicted results in multiple linear regression (MLR) analysis. The results and discussion will be presented in Chapter 4.

Table 3.5 L16 orthogonal array based on Taguchi analysis

Test no.	A(CWFS)	B(HIL)	C(HIT)	D(VL)	E(VT)	F(TS)	G(BD)
	(mm/s)	(kJ/mm)	(kJ/mm)	(V)	(V)	(mm/s)	(mm^2)
1	16.9	1.6	1.3	33	34	21.2	12
2	16.9	1.6	1.3	33	34	23.3	25
3	16.9	1.8	1.5	36	37	21.2	12
4	16.9	1.8	1.5	36	37	23.3	25
5	25.4	1.6	1.3	36	37	21.2	12
6	25.4	1.6	1.3	36	37	23.3	25
7	25.4	1.8	1.5	33	34	21.2	12
8	25.4	1.8	1.5	33	34	23.3	25
9	33.9	1.6	1.5	33	37	21.2	25
10	33.9	1.6	1.5	33	37	23.3	12
11	33.9	1.8	1.3	36	34	21.2	25
12	33.9	1.8	1.3	36	34	23.3	12
13	42.3	1.6	1.5	36	34	21.2	25
14	42.3	1.6	1.5	36	34	23.3	12
15	42.3	1.8	1.3	33	37	21.2	25
16	42.3	1.8	1.3	33	37	23.3	12

Table 3.6 Welding table for confirmatory tests

Test no.	A(CWFS)	B(HIL)	C(HIT)	D(VL)	E(VT)	F(TS)	G(BD)
	(mm/s)	(kJ/mm)	(kJ/mm)	(V)	(V)	(mm/s)	(mm^2)
C1	25.4	2.0	1.4	36	34	21.2	25
C2	33.9	1.6	1.8	33	37	21.2	25
C3	29.6	1.8	1.4	33	38	21.2	25

The optimized level of parameters was determined based on the statistical analysis in Chapter 4. In Chapter 5, a series of welding tests were conducted using the optimized parameter levels, which are shown in Table 3.7. CWFS of zero (CW0-Ref.), 16.9 mm/s (CW40) and 33.9 mm/s (CW80) were used to fabricate the weldments while the other weld parameters remained identical. For the evaluation of productivity, an additional weldment with 16.9 mm/s CWFS and 25.4 mm/s travel speed (CW40-TS60) was fabricated. The reasons for not selecting a travel speed faster than 25.4 mm/s was the presence of weld defects on the weldment surface such as entrapped flux and undercuts.

Table 3.7 Weld tests using optimized levels

Weld parameters	Welding tests					Optimized levels
	Unit	CW0-Ref.	CW40	CW80	CW40-TS60	
Heat input of Lead	(kJ/mm)	1.6	1.6	1.6	1.6	1.6
Heat input of Trail	(kJ/mm)	1.3	1.3	1.3	1.3	1.3
Voltage of Lead	(V)	31	31	31	33	-
Voltage of Trail	(V)	33.5	33.5	33.5	35	-
Current of Lead	(A)	1100	1100	1100	1240	-
Current of Trail	(A)	825	825	825	950	-
Travel speed	mm/s	21.2	21.2	21.2	25.4	21.2
Cold wire feed	mm/s	0	16.9	33.9	16.9	-

3.3 Sample Preparation

The specific procedures for preparation of weldment samples and metallographic samples are presented in this section. A description of etchants used on metallographic samples for weld characterization analysis is also provided.

3.3.1 Weldment Samples

Weldment samples preparation followed a series of steps to achieve the requirements of metallurgical samples. Before sectioning, all welded plates were inspected visually to check for weld defects, such as undercuts, surface porosity and burn through. Table 3.8 summarizes the purposes and requirements of cutting and sectioning weldments; a schematic illustration is provided in Figure 3.3. The steps are as follows:

- Step a: Rough sectioning of the run-on tabs and residual base metal was conducted using a vertical saw to achieve the requirements of 20-30 mm from each weld bead toe side.
- Step b: Three weld specimens (15 mm width and 19 mm thick) were extracted from each welded plate based on visual inspection and numbered according to the welding direction.
- Step c: Extra base metal was precisely removed to match the size of the mounting holder.

Especially in step c, consideration of the mounting size holder and cutting distance from the bead toe is necessary because the weld bead length is varied in each welded plate. Accordingly, 48 specimens (16 welded plates x 3 specimens) were sectioned at the transverse direction relative to the welding direction. Good sectioning improved the efficiency of metallographic sample preparation.

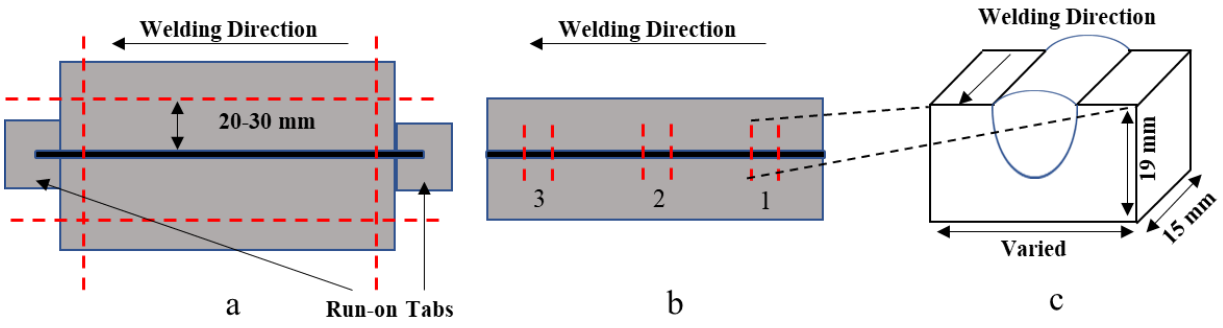

Figure 3.3 Schematic of process for sectioning a welded plate.

Table 3.8 Steps used in sectioning weldments

Steps	Equipment	Purpose	Requirements	Schematic
a	Vertical saw	Roughly remove run-on tabs and residual base metal (see Figure 3-3)	Section weldments to remain 20-30 mm from each weld bead toe side	Figure 3.3a
b	Vertical saw	Extract the selected sample area	Align cutting direction at the transverse direction to produce 15 mm width samples	Figure 3.3b
c	Precision saw	Remove extra base metal (small amount)	Precisely cut weldments to match size of mounting holder	Figure 3.3c

3.3.2 Metallographic Samples

After sectioning, metallographic specimens were mounted and polished according to ASTM E3-11 standard [79]. The equipment for polishing was a Buehler EcoMet 250 grinder-polisher which provided the required polishing on the specimens depending on the observation techniques being used. Weld specimens were ground using silicon carbide grinding paper and then polished with a series of diamond suspensions to a 3 μm finish. This was followed by 1 μm alumina and lastly 0.05 μm alumina where necessary. Required polishing finishes and etching details with matching application are shown in Table 3.9.

Metallographic samples mechanically polished to a 3 μm finish were subsequently etched with 4% Nital to reveal HAZ and WM boundaries. Two main etchants, LePera and Picral, were modified to reveal specific phases in the CGHAZ and the detailed compositions of the etchants are shown in Table 3.9. In addition, some samples needed a finer finish (0.05 μm) prior to etching. All etching processes were conducted at room temperature with varied etching times as shown in Table 3.9. A summary of the characterization techniques employed after each etching process is presented next.

Table 3.9 Etching techniques and metallographic specimen requirements

No.	Etchant	Polish finish	Concentration	Time	Application
1	Nital	3 µm diamond suspension	4 ml nitric acid in 100 ml ethanol	30-40s	Etching of HAZ and WM boundaries
2	Modified LePera	0.05 µm diamond suspension	a) 4 g picric acid and 1 ml HCl acid in 96 ml ethanol; b) 1 g $Na_2S_2O_5$ in 100 ml distilled water -Mixture of a) and b) in equal volume ratio (1:1)	45-55s	Etching of polygonal ferrite, granular bainite, bainitic ferrite and MA constituents [80]
3	Modified Picral Etchant	0.05 µm diamond suspension	4 g picric acid in 96 ml distilled water + few drops of HCl	45-60s	Etching of PAG boundaries [31]

3.4 Weld Characterization Techniques

This section presents four metallographic techniques, including stereomicroscopy, optical microscopy (OM), scanning electron microscopy (SEM) and electron backscatter diffraction (EBSD) used for weld characterization. A summary of the characterization techniques and type of etchant are shown in Table 3.10.

Table 3.10 Summary of weld characterization techniques

Characterization technique	**Objective**	**Results**	**Etchant**
Stereomicroscopy	Measure geometrical values	Geometry measurements including length, area and bead angle of weld specimen in WM and HAZ	4% Nital
OM	Identify phases and measure grain size and phases fraction	Identification of microstructural constituents; Volume and size measurement of MA constituents in HAZ;	Modified LePera [80]
		Grain size measurement of PAG in HAZ	Modified Picral [31]
SEM	Identify and characterize phases	Volume and size measurement of MA constituents in HAZ	Modified LePera [80]
EBSD	Measure grain size and misorientation angle	Size of ferrite/bainite grains and distribution of boundary misorientation angles	Not etched

3.4.1 Stereomicroscopy

Three weld samples extracted from one weldment, as shown in Figure 3.4a, were used to measure geometry characteristics. A total of 48 specimens were obtained. Each sample was mounted and polished following the ASTM E3-11 standard [79] and then were macro-etched using 4% Nital to reveal the HAZ and WM boundaries (Figure 3.4b). A stereomicroscope image was obtained from each section and analyzed using Image J to obtain the weld geometry values including bead width (BW), penetration depth (PD), penetration area (PA), bead width at half penetration depth ($BW_{1/2}$), height of reinforcement area (HRA), reinforcement area (RA), bead toe angle (BTA) and CGHAZ area as per Figure 3.4b.

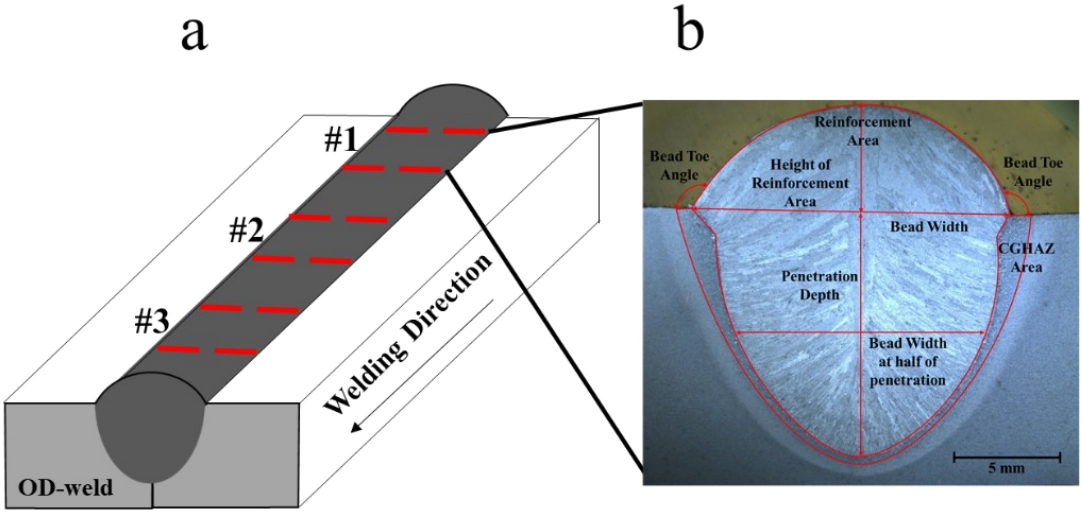

Figure 3.4 a) Schematic showing sectioning position of welds. b) Macrograph of Sample Test 1-1.

The weld geometry values obtained from the stereomicroscope images were utilized to calculate aspect ratio (AR), semi-penetration ratio (SPR) and the amount of dilution of the weld, as shown in Equations 3.3 to 3.5, respectively.

$$AR = \frac{\text{PD}}{\text{BW}} \tag{3.3}$$

$$SPR = \frac{BW_{1/2}}{\text{BW}} \tag{3.4}$$

$$Dilution = \frac{\text{PA}-\text{bevel area}}{\text{PA}+\text{RA}} \tag{3.5}$$

The bevel areas in the two bevel specifications were 12 mm^2 and 25 mm^2 (Figure 3.1).

3.4.2 Optical Microscopy (OM)

Optical microscopy (OM) was conducted using an Olympus BX61 microscope and Olympus StreamMotion software. The objective of using OM was to identify microstructures such as martensite-austenite (MA) constituent and prior-austenite grains (PAG) in the HAZ. The weld specimens were micro-etched with modified LePera's and modified picral solutions to reveal MA and PAG, respectively, in the HAZ.

3.4.3 Scanning Electron Microscopy (SEM)

Scanning electron microscopy (SEM) was done using a Zeiss EVO M10 SEM operating at 20 kV accelerating voltage. The feature of high magnification in the SEM was suitable to characterize MA constituents after a proper modified LePera's etching process.

Quantitative analysis of MA constituents and PAG size for both optical and SEM micrographs was done using ImageJ commercial image analysis software. The mean liner intercept method according to ASTM E112 was carried out to analyze the PAG size [81]. The microstructural analysis results were correlated with mechanical properties for a better understanding of the effect of cold wire addition to the HAZ.

3.4.4 Electron Backscattered Diffraction (EBSD)

Electron backscattered diffraction (EBSD) analysis was completed employing the Zeiss Sigma FESEM for data acquisition. Before EBSD analysis, the sample surfaces were polished to a final step using 0.02 diamond suspension to avoid any micro-scratches. EBSD was mainly employed to obtain the misorientation associated with grain boundaries. The accuracy of the collected data from grain average misorientation was quite sensitive to the grain size of the sample and the scanning step size [82]. The detailed illustration of scanning step size and results analysis related to EBSD are presented in Chapter 5.

3.5 Mechanical Properties

Two mechanical property testing methods, micro-hardness testing and Charpy V-notch impact testing (CVN), were utilized.

3.5.1 Micro-hardness

Vickers micro-hardness measurements were obtained from the BM, HAZ and WM, as illustrated in Figure 3.5 [83]. Two indentation lines (5 mm below the surface) contained a total of 50 indents from each weld sample to guarantee 10 to 12 indents in the WM and CGHAZ. A 500 g load and a dwell time of 14 s were used. The distance between two indents was three times the size of an indent, as indicated in images in Figure 3.5.

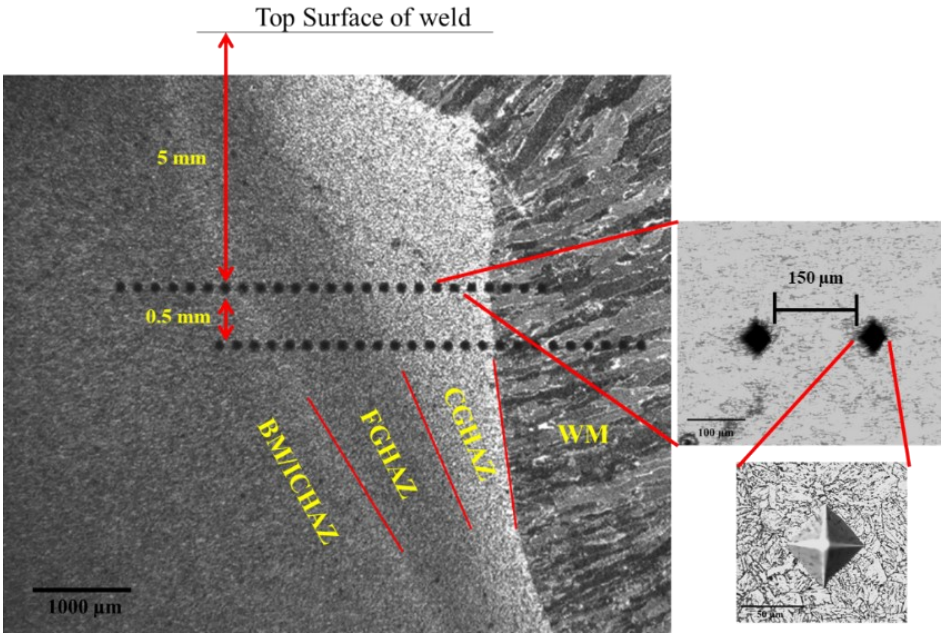

Figure 3.5 Example of micro-hardness mapping along the HAZ and WM of a CWTSAW sample.

3.5.2 Impact Toughness

Sub-size Charpy V notch specimens (5 mm * 10mm * 55mm) were machined along the transverse direction at the quarter thickness of the weld according to ASTM E23-12C [84]. Then, the machined specimens were macro-etched with 5% Nital to reveal the HAZ and WM boundaries. The notch position of Charpy specimens was entirely located in the CGHAZ. The Charpy tests were performed on the specimens at 301 K (28 °C), 263 K (-10 °C), 243 K (-30 °C), 228 K (-45 °C)

and 213 K (-60 °C). Three specimens from each welding condition were tested at each temperature. Figure 3.6 illustrates the location of the extracted specimen and notch position.

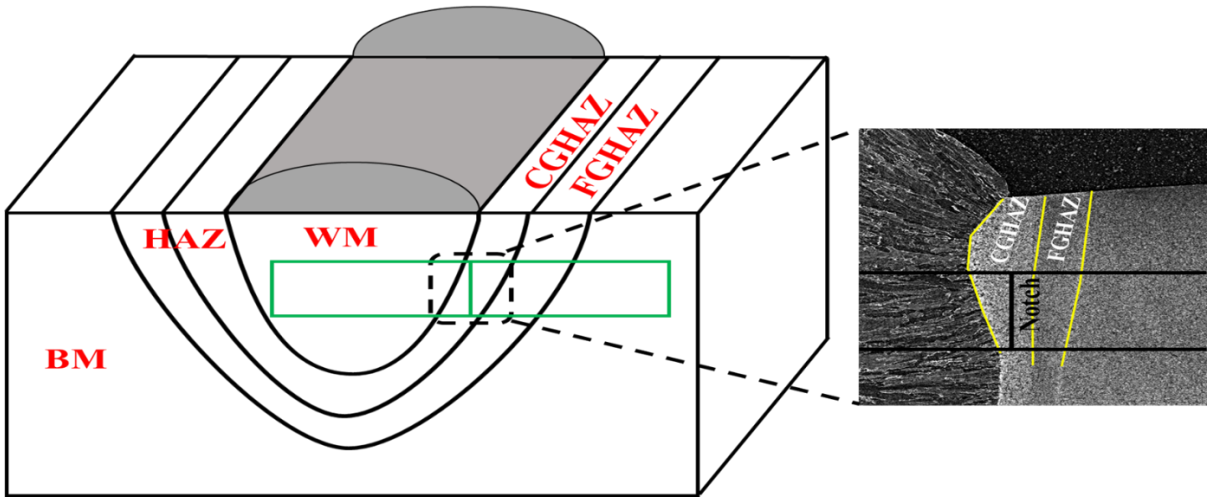

Figure 3.6 Schematic and image of sub-size CVN specimen.

Chapter 4: Parametric Study of CWTSAW

In this Chapter, the effects of the heat input of the lead (HIL) and trail (HIT) electrodes, the voltage of the lead (VL) and trail (VT) electrodes, travel speed (TS), bevel design (BD) and cold wire feed speed (CWFS) on the weld geometry, micro-hardness of the HAZ and microstructure of the CGHAZ were studied. In total, 16 test welds were conducted. The specific test welds were designed using the Taguchi method. Following welding, the weld geometrical characteristics were measured, including bead width (BW), penetration depth (PD), penetration area (PA), bead width at half of penetration depth ($BW_{1/2}$), reinforcement area (RA), the height of reinforcement area (HRA), bead toe angle (BTA), aspect ratio (AR), semi-penetration ratio (SPR) and CGHAZ area.

The measurements were analyzed using three statistical methods; i.e., analysis of variance (ANOVA), multiple linear regression (MLR) analysis, and signal-to-noise (S/N) ratio. ANOVA was used to determine the significant weld parameters by analyzing the variability of the data using the variance ratio (F value), sum of squares (SS) and level of significance (P value) [43]. MLR is a linear model used to develop empirical equations for response characteristics and mechanical properties, such as SPR, RA, HRA, CGHAZ area and micro-hardness of the CGHAZ and WM [50]. S/N ratio is the method for optimizing the levels of weld parameters to improve weld geometry [53].

4.1 Measured Weld Characteristics

The welding parameters selected for the parametric study of CWTSAW are listed in Table 3.4 (Chapter 3). The weld characteristics measured for each of the 16 tests are presented in this section. The results of bead width (BW), height of reinforcement area (HRA), bead toe angle (BTA), reinforcement area (RA) and CGHAZ area are shown in Table 4.1. The values shown in brackets are one standard deviation. In Table 4.1, the maximum value and minimum value for each weld characteristic are in bold and underlined, respectively.

Minimum and maximum measured BW values of 12.4 mm and 15.6 mm were obtained for Test 8 and Test 13 samples, respectively. The maximum measured HRA (5.7 mm) and RA (57.1 mm^2) and the minimum measured BTA (111.8°) were obtained for the Test 7 sample. This combination is the largest reinforcement shape for all welds. Conversely, Test 11 sample have the lowest HRA (3.2 mm) and highest BTA (136.6°), which represents the smallest reinforcement

shape in all welds. Moreover, the largest (30.2 mm^2) and smallest CGHAZ area (20.8 mm^2) occur for observed in Test 8 and Test 5 samples, respectively. The CGHAZ area is one of the significant weld characteristics due to its inferior mechanical properties, particularly toughness [5], [74], [85]. Additional measured weld characteristics will be presented later.

Table 4.1 Results for BW, HRA, BTA, RA and CGHAZ area

Trail No.	BW (mm)	HRA (mm)	BTA (º)	RA (mm^2)	CGHAZ Area (mm^2)
1	14.0 (0.6)	5.0 (0.1)	123.5 (2.6)	51.3 (3.1)	22.1 (1.7)
2	13.4 (0.5)	4.2 (0.1)	127.8 (2.6)	39.5 (1.3)	27.5 (0.5)
3	15.3 (0.2)	4.4 (0.1)	125.2 (2.9)	47.5 (0.8)	24.2 (0.1)
4	14.1 (0.1)	3.6 (0.1)	130.7 (4.8)	35.0 (3.3)	26.0 (1.1)
5	15.1 (0.3)	4.0 (0.3)	127.0 (0.6)	45.4 (5.8)	20.8 (0.7)
6	14.7 (0.1)	3.9 (0.1)	135.7 (3.3)	36.8 (1.8)	24.4 (0.6)
7	13.2 (0.1)	**5.7 (0.1)**	111.8 (3.9)	**57.1 (3.2)**	26.1 (0.9)
8	12.4 (0.1)	5.2 (0.1)	113.5 (3.7)	47.9 (1.9)	**30.2 (1.5)**
9	14.7 (0.4)	3.5 (0.1)	124.0 (2.4)	37.4 (1.2)	27.4 (0.6)
10	13.3 (0.2)	4.9 (0.1)	121.7 (1.6)	49.2 (1.6)	23.8 (0.1)
11	14.7 (0.4)	3.2 (0.1)	**136.6 (2.9)**	31.9 (1.1)	27.8 (1.4)
12	14.4 (0.1)	4.9 (0.2)	119.8 (1.7)	52.9 (4.4)	23.0 (1.1)
13	**15.6 (0.1)**	4.0 (0.3)	133.2 (1.4)	43.1 (2.9)	25.7 (1.1)
14	12.8 (0.3)	5.5 (0.2)	112.1 (2.7)	52.3 (2.8)	23.1 (1.2)
15	13.5 (0.3)	3.5 (0.1)	136.0 (2.5)	31.2 (0.7)	27.8 (1.1)
16	13.3 (0.4)	4.9 (0.2)	119.6 (1.4)	47.1 (2.8)	22.2 (0.3)

*****Maximum values are indicated in bold and minimum values are underlined in each column.

Penetration area (PA), penetration depth (PD), bead width at half of penetration ($BW_{1/2}$), aspect ratio (AR), semi-penetration ratio (SPR) and dilution are presented in Table 4.2. AR, SPR and dilution were calculated as per Equations 3.3 to 3.5 presented in Chapter 3. The maximum PA (171.4 mm^2) and PD (15.2 mm) were measured for Test 8 sample. Test 8 sample had the highest AR (1.22) and SPR (1.08). The amount of dilution is the amount of parent metal melted relative

to the total amount of fused metal. This value will influence the composition of the molten pool and properties of the weld [86], [87]. Therefore, the low amount of dilution in Test 13 samples (0.621) is more suitable than the high amount of dilution in Test 4 samples (0.694).

Table 4.2 Results for PA, PD, $BW_{1/2}$, AR, SPR and dilution

Trail No.	PA (mm^2)	PD (mm)	$BW_{1/2}$ (mm)	AR	SPR	Dilution
1	123.2 (1.8)	11.6 (0.1)	12.0 (0.1)	0.83 (0.03)	0.86 (0.04)	0.639 (0.009)
2	139.7 (3.3)	13.0 (0.2)	12.1 (0.3)	0.98 (0.03)	0.90 (0.04)	0.640 (0.005)
3	139.1 (0.6)	12.3 (0.1)	12.7 (0.1)	0.80 (0.02)	0.83 (0.01)	0.683 (0.003)
4	161.0 (2.0)	13.7 (0.1)	**13.5 (0.2)**	0.97 (0.02)	0.96 (0.01)	**0.694 (0.008)**
5	119.4 (2.3)	10.9 (0.3)	12.1 (0.01)	0.72 (0.06)	0.80 (0.04)	0.655 (0.025)
6	142.6 (2.0)	12.2 (0.1)	13.1 (0.1)	0.83 (0.03)	0.89 (0.04)	0.655 (0.009)
7	139.2 (0.4)	13.3 (0.1)	12.0 (0.1)	1.01 (0.06)	0.91 (0.05)	0.650 (0.009)
8	**171.4 (4.1)**	**15.2 (0.1)**	13.4 (0.4)	**1.22 (0.02)**	**1.08 (0.01)**	0.667 (0.001)
9	142.9 (2.1)	13.2 (0.1)	12.2 (0.1)	0.90 (0.03)	0.83 (0.02)	0.654 (0.007)
10	135.4 (2.5)	12.8 (0.2)	12.3 (0.1)	0.97 (0.02)	0.93 (0.03)	0.670 (0.004)
11	143.4 (3.1)	13.1 (0.4)	12.5 (0.1)	0.89 (0.01)	0.85 (0.01)	0.675 (0.006)
12	132.8 (0.4)	12.1 (0.1)	12.2 (0.3)	0.84 (0.05)	0.85 (0.05)	0.653 (0.016)
13	136.6 (2.5)	12.4 (0.1)	11.7 (0.1)	0.80 (0.02)	0.75 (0.02)	0.621 (0.013)
14	134.4 (1.5)	12.8 (0.1)	11.9 (0.2)	1.00 (0.03)	0.93 (0.02)	0.658 (0.009)
15	142.3 (1.2)	13.1 (0.3)	11.8 (0.2)	0.97 (0.01)	0.88 (0.02)	0.676 (0.004)
16	134.7 (2.3)	12.5 (0.1)	12.4 (0.2)	0.94 (0.02)	0.94 (0.03)	0.677 (0.007)

*****Maximum values are indicated in bold and minimum values are underlined in each column

Table 4.3 shows the CGHAZ hardness and the WM hardness, including the average value and one standard deviation for each of the 16 tests. Both lowest hardness values for the CGHAZ and WM are observed in Test 11. The highest hardness values for the CGHAZ and WM were measured from Test 2 and Test 4, respectively.

Table 4.3 Hardness Values

Trail No.	CGHAZ Hardness	WM Hardness
1	215.9 (1.9)	230.0 (0.9)
2	**223.8 (1.5)**	233.2 (3.9)
3	220.6 (1.8)	234.7 (4.6)
4	220.1 (1.9)	**237.1 (1.9)**
5	216.2 (1.0)	233.7 (2.4)
6	222.3 (2.9)	232.0 (0.2)
7	216.6 (1.8)	232.9 (2.7)
8	215.1 (1.3)	234.4 (1.3)
9	212.9 (1.3)	229.7 (1.3)
10	215.0 (1.7)	235.4 (0.8)
11	<u>208.9 (1.4)</u>	<u>225.8 (0.9)</u>
12	215.4 (1.3)	228.8 (4.8)
13	213.8 (1.4)	232.7 (3.1)
14	219.9 (1.8)	236.1 (2.1)
15	215.6 (1.6)	234.3 (3.8)
16	209.7 (1.5)	230.5 (4.7)

*****Maximum values are indicated in bold and minimum values are underlined in each column

Figure 4.1 is a plot of CGHAZ micro-hardness vs. WM micro-hardness. The general trend is that WM hardness increases with increasing CGHAZ hardness. This correlation suggests that factors influencing the CGHAZ hardness affect the WM hardness in a similar manner.

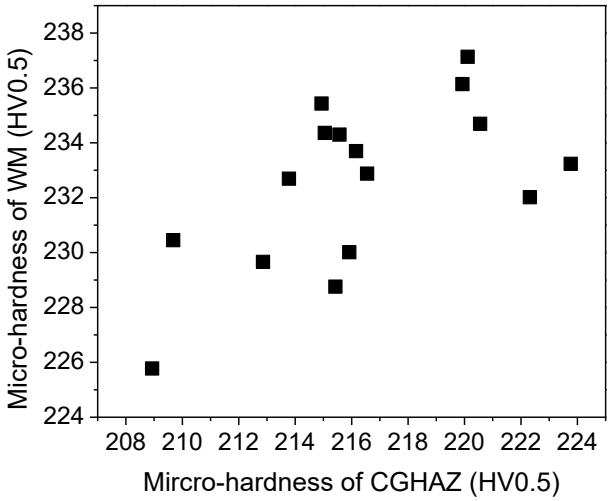

Figure 4.1 Plot of CGHAZ micro-hardness vs. WM micro-hardness.

Figure 4.2 shows a plot of penetration area (PA) vs. CGHAZ area. CGHAZ area appears to expand as PA expands. This correlation appears to be reasonable since the CGHAZ is adjacent to the WM. The increased PA produces a larger amount of WM (consists of both PA and RA), which increases the CGHAZ area. Test 4 and Test 8 appear to be outliers. The observed correlation is based on the relationship between PA and WM without considering the effect of welding parameters, such as heat input and voltage.

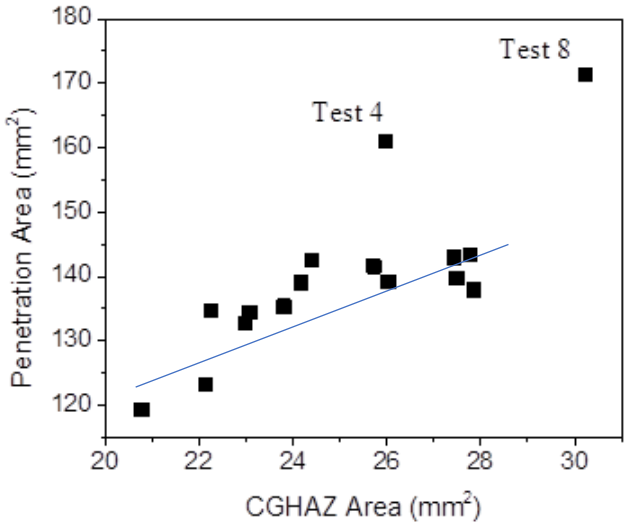

Figure 4.2 Plot of CGHAZ area vs. penetration area (The line passing through to data points represents a guide to illustrate the overall data trend).

The trend between CGHAZ area and RA is shown in Figure 4.3. RA decreases as CGHAZ area is increased. The decreased RA may facilitate full penetration in the weld which may increase the size of CGHAZ area. The bevel design (BD) influences the observed correlation between the RA and CGHAZ area, which is analyzed in Section 4.4. Although Test 7 and Test 8 do not follow the observed trend, the data are necessary for statistical analysis. The fitted equation of the line passing through to data points in Figure 4.2 and 4.3 is not the focus of this study. However, due to the outliers in the Figures more information on the correlation between welding parameters and measured weld geometry is presented in Section 4.3.

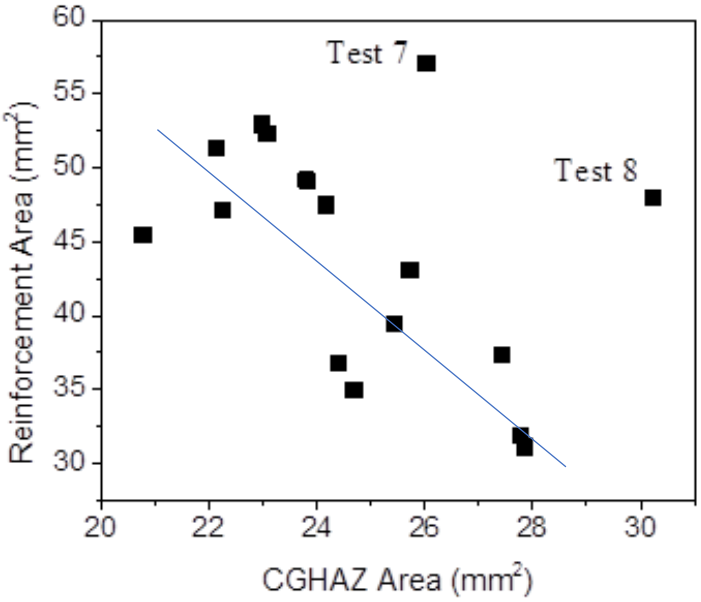

Figure 4.3 Correlation of CGHAZ area and reinforcement area (The line passing through to data points represents a guide to illustrate the overall data trend).

4.2 Analysis of Variance (ANOVA)

The ANOVA table for each weld characteristic is presented in this section. Based on the value of P, significant parameters for each of measured weld characteristics are determined.

4.2.1 Quantities of ANOVA

Table 4.4 shows the ANOVA table for reinforcement area (RA). All the remaining ANOVA tables are presented in Appendix A. Included in the Table 4.4 are probabilities of significance (P), degrees of freedom (DOF), sum of squares (SS), variance ratios (F) and R^2 values for each welding parameter.

P values are used to determine the statistical significance of each of the welding parameters [6], [42], [45]. A P value equal to or less than 0.05 indicates the parameter is statistically significant with a 95% confidence. A P value of 0.25 corresponds to a 75% confidence level that the parameter is statistically significant for the weld characteristic. The significant welding parameters affecting reinforcement area (RA) are heat input of the trail electrode (HIT), voltage of the trail electode (VT) and bevel design (BD), all with a confidence level of 95%.

The SS value in Table 4.4 is used to evaluate the percentage contribution of each weld parameter to the weld characteristic. The SS values for the remaining weld characteristics are provided in Appendix A. The R^2 value is a statistical measure of the validity of the statistical model and it represents the proportion of explained variation in total variation. Therefore, a high R^2 value; e.g., 90%, means that approximatly 90% of the observed variation can be explained by the statistical model.

Table 4.4 ANOVA table for RA

Characteristic		CWFS	HIL	HIT	VL	VT	TS	BD	R^2
RA	DF	3	1	1	1	1	1	1	95.2%
	SS	40.06	1.23	69.53	15.26	134.62	16.04	626.04	
	F	1.76	0.16	9.19	2.02	17.79	2.12	82.72	
	P	0.25	0.70	0.02	0.21	0.01	0.20	0.00	

4.2.2 P Values for All the Welding Parameters.

The P values for individual weld geometry results and micro-hardness values for the CGHAZ and WM are listed in Table 4.5, along with confidence levels. For 95% and 75% confidence levels, the significant welding parameters are highlighed in bold. The effect of each welding parameter on the weld characteristic is presented in the next section in the form of a multiple linear regression (MLR) analysis.

Table 4.5 P values for weld geometry results and CGHAZ and WM micro-hardness values

Characteristic	CWFS	HIL	HIT	VL	VT	TS	BD	Confidence level
BW	0.65	0.32	0.49	**0.012**	0.20	**0.023**	0.63	95%
HRA	**0.027**	0.70	**0.005**	**0.003**	**0.001**	**0.002**	**0.00**	
BTA	0.50	0.52	**0.021**	**0.05**	**0.05**	0.081	**0.004**	
RA	0.25	0.70	**0.023**	0.21	**0.006**	0.20	**0.00**	
CGHAZ area	0.31	**0.02**	**0.033**	**0.032**	0.10	0.28	**0.001**	
AR	0.59	**0.043**	**0.033**	**0.008**	0.10	0.015	0.11	
SPR	0.37	0.074	0.21	0.053	0.56	**0.008**	0.54	
Dilution	0.76	**0.011**	0.37	0.44	**0.021**	0.23	1.00	
CGHAZ Hardness	**0.13**	0.28	0.70	0.42	0.86	**0.21**	0.83	75%
WM Hardness	**0.17**	0.65	**0.04**	0.95	**0.20**	**0.19**	0.77	

*Significant parameters are indicated in bold.

4.3 Multiple Linear Regression (MLR) Analysis

The objective of MLR is to model a linear relationship between the independent variables (weld parameters) and the response factors (geometric characteristics and micro-hardness profiles). Only linear response modelling was conducted in this chapter due to the large number of test variables that were examined, and the low number of tests conducted. A third order multiple regression analysis (TOMRA) is provided in Appendix A.

The MLR equation is of the following form:

$$y_i = C_0 + C_1 \cdot x_{i1} + C_2 \cdot x_{i2} + C_3 \cdot x_{i3} + \cdots + C_p \cdot x_{ip} \quad (4.1)$$

where y_i is the response variable (e.g., geometric characteristics and micro-hardness), x_{ip} is the statistically significant welding parameter and C_0 is the intercept. MLR was developed for HRA, BTA, RA, CGHAZ area, BW and micro-hardness of the CGHAZ and WM, as shown in Equations 4.2 to 4.8.

To validate each equation, three (3) complementary tests were conducted and are included in Figures 4.4 to 4.10. The weld table for these complementary tests is shown in Table 3.6 from Chapter 3. The rest of the MLR results for AR, SPR and dilution are presented in Appendix A.

4.3.1 Height of Reinforcement Area (HRA)

The MLR equation for HRA is given in Equation 4.2. Six significant parameters, i.e., CWFS, HIT, VL, VT, TS and BD, are predictors in Equation 4.2. The coefficient for each of the significant parameters was received using regression command in Excel. The predicted values, calculated according to Equation 4.2, are correlated with the measured HRA values in Figure 4.4. Included in the figure are the values from the complementary tests (triangles). The predicted and measured HRA values fit reasonably well as indicated by the relatively high R^2 value. Also, the complementary results are fairly close to the trend line (the straight line) in Figure 4.4.

$$HRA = 10.2 - 0.0002 \cdot CWFS + 1.99 \cdot HIT - 0.14 \cdot VL - 0.21 \cdot VT + 0.096 \cdot TS - 0.078 \cdot BD \quad (4.2)$$

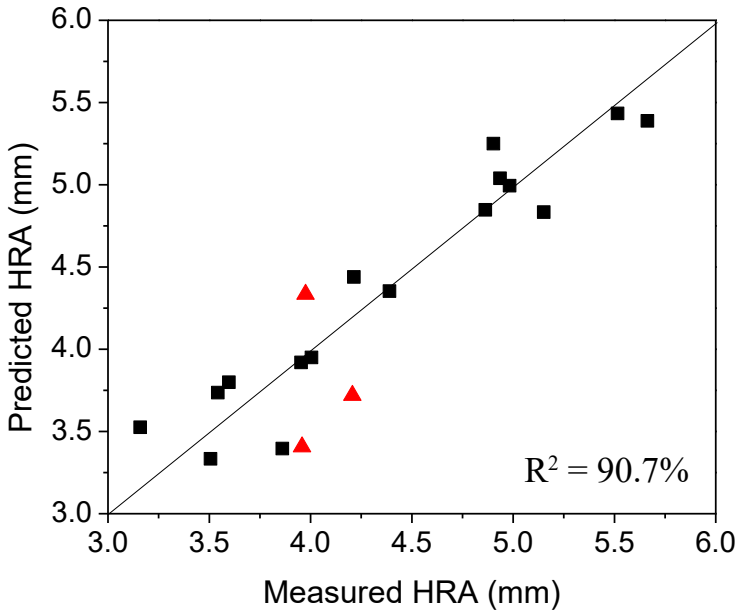

Figure 4.4 Measured and predicted values for HRA.

4.3.2 Bead Toe Angle (BTA)

The empirical equation for BTA is shown in Equation 4.3. The predicted BTA values are plotted vs. the measured values in Figure 4.5. The fit for BTA is not as good as that for HRA, but the BTA model is still valid for prediction with an R^2 value of 83.3%. The three complementary tests fit well with the BTA model.

$$BTA = 83.6 - 33.61 \cdot HIT + 1.77 \cdot VL + 1.74 \cdot VT - 0.91 \cdot TS + 0.72 \cdot BD \quad (4.3)$$

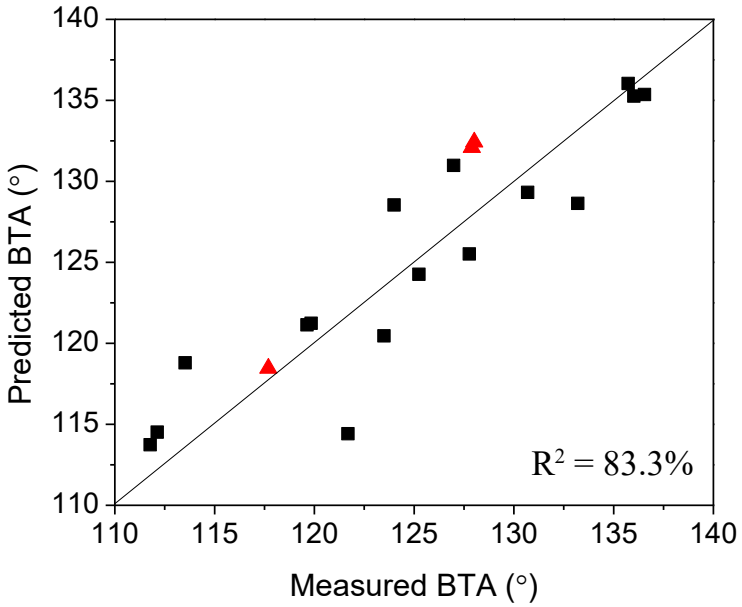

Figure 4.5 Measured and predicted values for BTA.

4.3.3 Reinforcement Area (RA)

The empirical equation for RA is shown in Equation 4.4 and the predicted RA values are plotted vs. the measured values in Figure 4.6. The R^2 value of 87.6%, which indicates a reasonable fit. One of the complementary test results varies somewhat from the ideal line. To summarize the overall reinforcement shape results, the trend lines for HRA, BTA and RA have fairly high R^2 values (83-91%) which indicates a good predictive behavior for reinforcement shape in the MLR model.

$$RA = 100.8 + 20.85 \cdot HIT - 1.93 \cdot VT - 0.94 \cdot BD \quad (4.4)$$

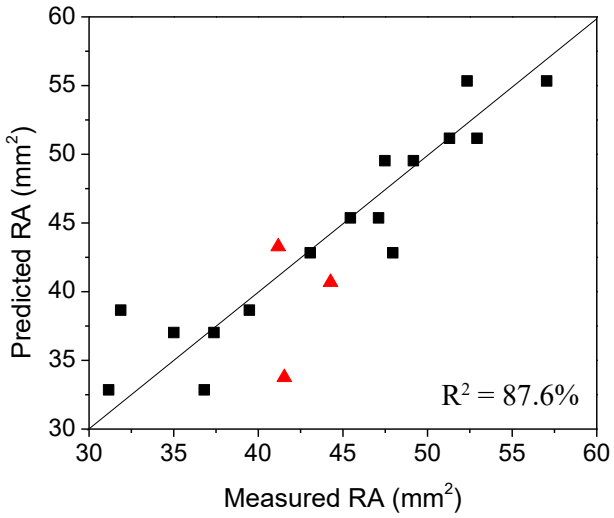

Figure 4.6 Measured and predicted values for RA.

4.3.4 CGHAZ Area

The empirical equation for CGHAZ area is shown in Equation 4.5. The predicted CGHAZ area values are plotted against the measured values in Figure 4.7. The R^2 value is 82.0% which is closed to the R^2 value for reinforcement shape indicating a reasonable fit. Most results are located near the ideal straight line indicating an accurate prediction using Equation 4.5. The complementary results lie reasonably close to the predicted values.

$$\text{CGHAZ Area} = 12.6 + 8.20 \cdot \text{HIL} + 7.22 \cdot \text{HIT} - 0.48 \cdot \text{VL} + 0.27 \cdot \text{BD} \qquad (4.5)$$

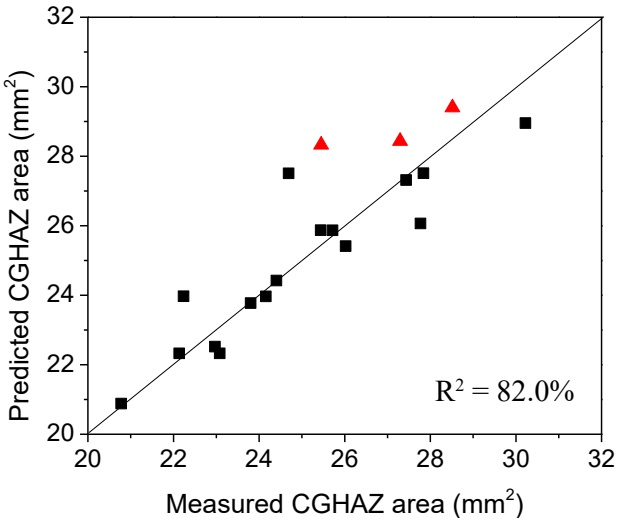

Figure 4.7 Measured and predicted values for CGHAZ area.

4.3.5 Bead Width (BW)

The empirical equation for BW is shown in Equation 4.6 and the predicted BW values are plotted against the measured values in Figure 4.8. The points are somewhat dispersed about the trend line and the R^2 value is only 71%. This lower R^2 value for the BW model corresponds to more error indicating the predictions are less precise. Three predictors in Equation 4.6 are selected based on the statistically significant parameters for BW. The remaining parameters and interactions are not included, but may also influence the BW. The complementary tests fit well with the BW model.

$$BW = 5.56 + 0.38 \cdot VL + 0.16 \cdot VT - 0.20 \cdot TS \quad (4.6)$$

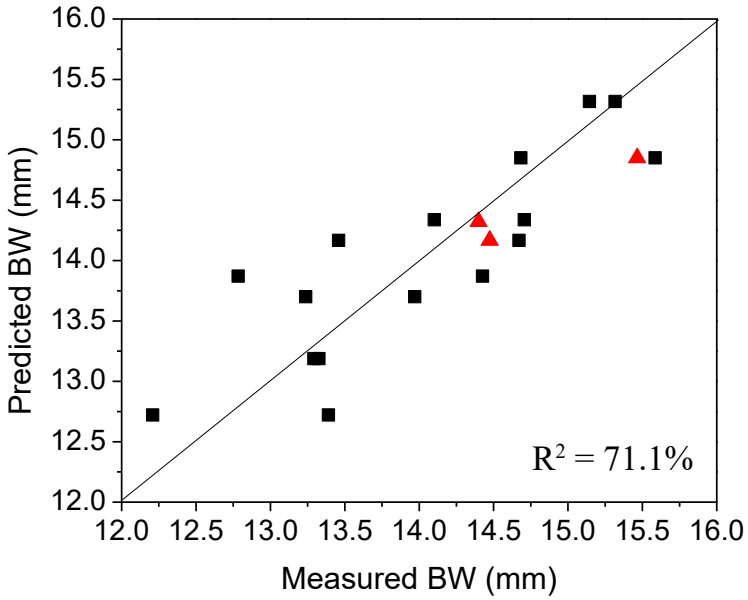

Figure 4.8 Measured and predicted values for BW.

4.3.6 CGHAZ Micro-hardness

The empirical equation for micro-hardness of CGHAZ is shown in Equation 4.7. This equation is used to predict the hardness of CGHAZ without including a cold wire feed speed (CWFS) of 42.3 mm/s. Including the CWFS of 42.3 mm/s within the model resulted in a low R^2 value of 50.7% (Figure 4.9-a). The fitting is improved (R^2 = 74.4%) if the 42.3 mm/s CWFS data is excluded (Figure 4.9-b). The CWFS, especially 42.3 mm/s, may have a dominant effect on the

CGHAZ micro-hardness. Moreover, the CWFS is the statistically significant parameter in Equation 4.7. The fundamental relationship between CWFS and CGHAZ hardness is presented in Section 4.4.

$$\text{Micro-hardness of CGHAZ} = 204.6 - 0.18 \cdot \text{CWFS} + 0.69 \cdot \text{TS} - 7.78 \cdot \text{HIL} \quad (4.7)$$

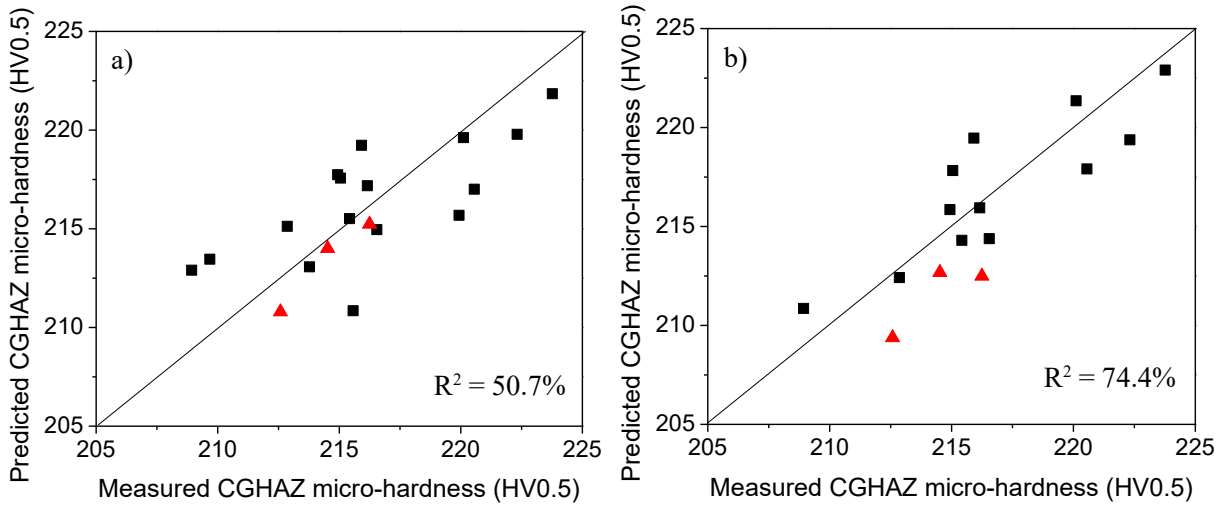

Figure 4.9 Predicted and measured micro-hardness for the CGHAZ: a) Includes data for CWFS of 42.3 mm/s and b) excludes data for CWFS of 42.3 mm/s.

4.3.7 WM Micro-hardness

The CWFS of 42.3 mm/s has a similar effect on the prediction of WM hardness as for CGHAZ hardness. A poor fit (R^2 = 48.7%) is obtained if the 42.3 mm/s data is included (Figure 4.10-a). A much better fit (R^2 = 81.8%) is achieved if the 42.3 mm/s CWFS data is excluded from Equation 4.8. Based on CWFS contribution to both empirical equations for CGHAZ and WM hardness, CWFS has a greater effect on the hardness profile than on the weld geometric profile in the MLR analysis.

$$\text{Micro-hardness of WM} = 170.0 - 0.097 \cdot \text{CWFS} + 0.47 \cdot \text{TS} - 13.9 \cdot \text{HIT} + 0.67 \cdot \text{VT} \quad (4.8)$$

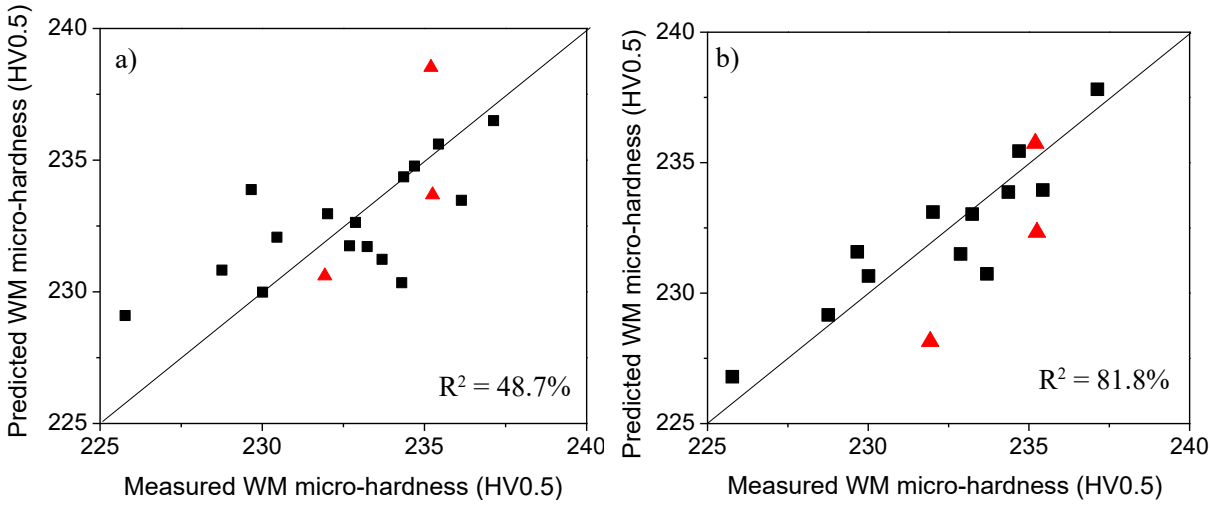

Figure 4.10 Predicted and measured micro-hardness for the WM: a) Includes data for CWFS of 42.3 mm/s and b) excludes data for CWFS of 42.3 mm/s.

4.4 Relationship Between Weld Characteristics and Welding Parameters

The quantitative effect of each significant weld variable on the weld characteristics is shown in Table 4.6 and was calculated using Equation 4.9.

$$Quantitative\ Effect = Level\ Range * Coefficient \tag{4.9}$$

The coefficient is associated with each predictor in MLR empirical equations. The level range is defined in Table 4.6. The level range for CWFS is from 16.9 mm/s to 33.9 mm/s and the 42.3 mm/s CWFS is excluded for the reasons given in the previous section (Section 4.3). In this section, the affected weld characteristics are discussed and correlated with the significant variables independently. The discussion on the quantitative effect of BD is presented in the next section. For the purpose of this section, the 42.3 mm/s CWFS data is not discussed.

Table 4.6 Quantitative effect of each significant weld variable on the weld characteristics

Characteristic	CWFS (mm/s)	HIL (kJ/mm)	HIT (kJ/mm)	VL (V)	VT (V)	TS (mm/s)	BD (mm^2)
Level range	16.9→33.9	1.6→1.8	1.3→1.5	33→36	34→37	21.2→23.3	12→25
BW (mm)	-	-	-	1.15	0.47	-0.98	-
HRA (mm)	-0.009	-	0.399	-0.426	-0.614	0.480	-1.034
BTA (°)	-	-	-6.72	5.31	5.21	-4.53	9.59
RA (mm^2)	-	-	4.17	-	-5.80	-	-12.51
CGHAZ area	-	1.64	1.44	-1.45	-	-	3.54
AR	-	0.081	0.087	-0.12	-	0.11	-
SPR	-	0.055	-	-0.061	-	0.10	-
Dilution	-	0.021	-	-	0.018	-	-
CGHAZ Hardness	-7.05	-1.56	-	-	-	3.44	-
WM Hardness	-3.86	-	2.77	-	2.01	2.37	-

4.4.1 Bead Width (BW)

Increasing overall voltage (lead + trail electrode) and decreasing travel speed (TS) results in a wider BW, as exhibited in Table 4.6. It is generally accepted that a higher arc voltage leads to a wider arc length (Figure 4.11) promoting the formation of a wide BW [34], [37], [88]. Thomas et al [89] correlated travel speed (TS) with BW of heavy gauge strip and reported that a high TS reduces the filler metal per unit length of weld leading to a narrow weld. This agrees with the V and TS results shown in Table 4.6. Specifically, a faster TS and lower V results in a shorter arc length and, as such, a smaller BW.

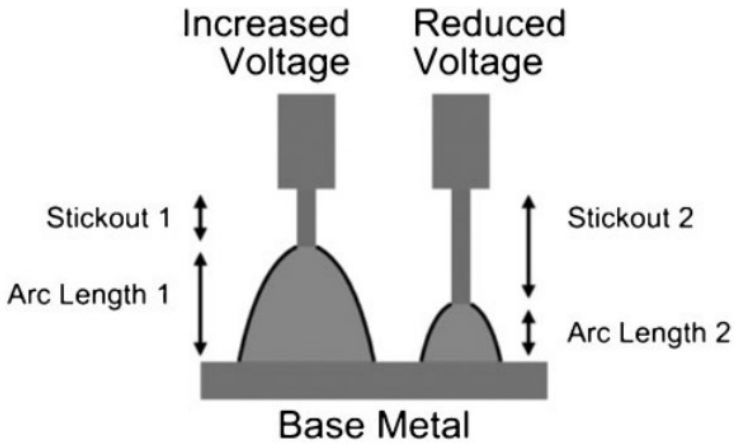

Figure 4.11 Effect of voltage on arc length [88].

4.4.2 Reinforcement Size (HRA, RA and BTA)

From Table 4.6 it is apparent that VL and VT negatively affect the height of reinforcement area (HRA) and postively affect bead toe angle (BTA). Specifically, increasing the voltage results in a lower HRA, larger BTA and smaller reinforcement area (RA). This observation is confirmed by the images in Figure 4.12. Reisgen et al [86] also reported that RA was reduced with increasing welding voltage in a SAW cold wire process. The effect of the HIT on the reinforcement size is also apparent in Table 4.6. Increasing the heat input of the trail electrode (HIT) results in a larger RA, higher HRA, and smaller BTA. This observation corresponds to the effect of heat input on the deposition rate, since deposition rate is defined as the amount of wire that is converted into weld metal (penetration area + reinforcement area). In the CWTSAW process, the polarity for heat input of the trail electrode (HIT) was selected as a square wave alternating current (ACSQ) due to its increased deposition rate, as reported by Pepin et al [38]. The improved deposition rate increased the amount of filler metal in the weld joint.

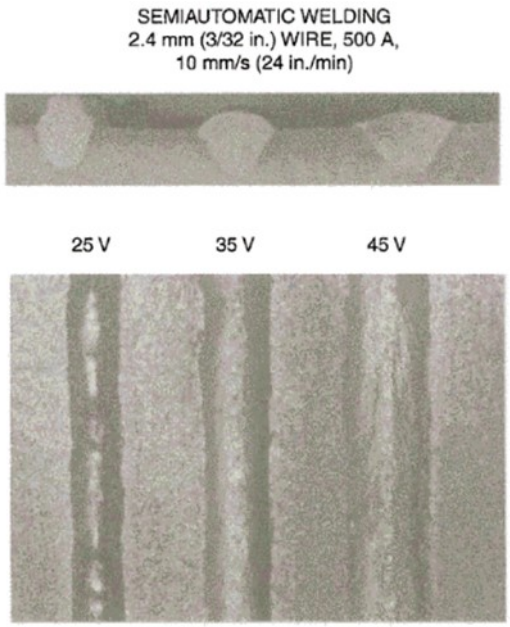

Figure 4.12 Effect of arc voltage variation on reinforcement [34].

4.4.3 CGHAZ Area

Table 4.6 shows that the heat input of lead and trail electrode (HIL and HIT) positively influence the CGHAZ area. Specifically, increasing HIL and HIT promotes growth in the size of the CGHAZ area. The growth of the CGHAZ area is related to the grain coarsening temperature and the grain size increased sharply above this temperature [33], [90]. The grain-coarsening temperature is generally related to the level of the weld thermal cycle which is governed by the amount of heat input of the electrode [91]. As such, increasing heat input means that a longer time is spent above the grain coarsening temperature which promotes grain coarsening [8], [92], [93]. Therefore, heat input is a dominant parameter affecting the growth of CGHAZ area.

4.4.4 Ratio of Weld Shape (SPR and AR)

The aspect ratio (AR) and semi-penetration ratio (SPR) are calculated using Equations 3.3 and 3.4 in Chapter 3, respectively, and were used to describe the weld shape. Both geometric ratio results are negatively affected by VL. As discussed previously, a wider BW is produced by a higher V due to the wider arc length. As VL is increased, AR and SPR are decreased due to the wider BW. Moreover, the TS has a positive influence on AR and SPR. The effect of TS variation on weld bead shape is exhibited in Figure 4.13. An increasing TS results in a smaller BW due to the

reduced heat input and reduced melted metal per unit length [88], [94]. Therefore, both AR and SPR are increased as TS increases, due to the smaller BW.

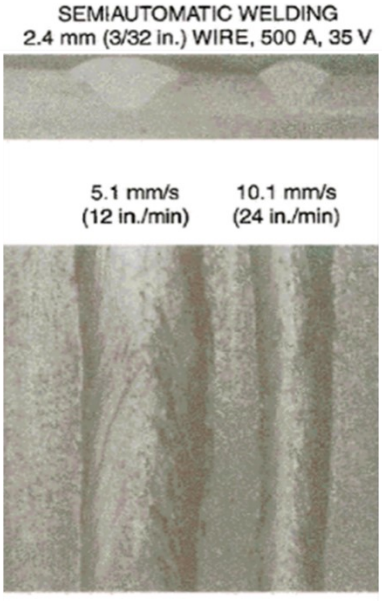

Figure 4.13 Effect travel speed variation on bead shape [34].

4.4.5 Dilution

Dilution is defined as the ratio of the amount of adjacent metal melted to the total amount of fused metal. The amount of dilution is affected by two geometric results: penetration area (PA) and reinforcement area (RA), as expressed in Equation 3.5, in Chapter 3 [95]. There are two significant parameters, heat input of the lead electrode (HIL) and voltage of the trail electrode (VT), that affect PA and RA. Specifically, the polarity of the HIL is direct current electrode positive (DCEP) in the welding process producing a weld with good penetration [41], [88]. Therefore, a higher HIL increases the penetration depth leading to more dilution. In addition, the effect of voltage on reinforcement was discussed in Subsection 4.3.2. More dilution was confirmed when there was a smaller RA in the weld. Finally, it is common to minimize the amount of dilution since the amount of dilution affects the composition of the molten pool and the resultant mechanical properties in the welds [8], [96].

4.4.6 Micro-hardness

The cold wire feed speed (CWFS) has the most dominant effect on the CGHAZ and WM micro-hardness profiles (Table 4.6), since cold wire addition alters the local thermal cycle by

absorbing the heat from the molten pool. Increasing the CWFS leads to a lower hardness because of the faster cooling rate [7], [31]. As discussed in previous sub-sections, the heat input and voltage may also contribute to the CGHAZ hardness profile since they can change the local thermal cycle and the size of the CGHAZ area. It is difficult to compare the effects of CWFS on hardness when other parameters are varied as well. The discussion on the effect of cooling rate on microstructure and related weld properties in the CGHAZ is presented in Chapter 5.

4.5 Importance of Bevel Design (BD)

In Table 4.6, BD exhibited the greatest effect on HRA, BTA, CGHAZ area and RA. In order to understand the effect of BD, the 16 measurements of RA, HRA, BTA, and CGHAZ area were plotted against two bevel specifications separately, as shown in Figure 4.14. The BD with a wider bevel area had lower RA and HRA, and increased BTA and CGHAZ area. This means that smaller and shallower reinforcement regions were produced for the larger bevel angle.

According to the study of the influence of bevel angle on heat transfer and fluid flow in the welding pool, published by Chen et al., increasing the bevel angle from 60° to 90° resulted in more liquid metal flowing downward. This means that increased bevel angle promotes heat transfer from the top to the bottom of the weld leading to full penetration [97]. Huang et al. also studied the effect of groove angle on weld depth in tungsten inert gas (TIG) welding by analyzing the current density and arc pressure. When the groove angle was increased, the current density and arc pressure were elevated at the groove bottom position, because of the concentrated arc heat input and stronger electromagnetic force at the bottom region of the high groove angle in comparison to the low groove angle [98]. This phenomenon indicates that there is a smaller RA in the wider BD than the shallower BD due to the achievement of full penetration.

The formation of a larger CGHAZ area in the deep BD than in the shallow BD is supported by Chen's simulation study of thermal cycles in the molten pool. The finding showed that the width of the overheated zone (1100°C - 1500°C) increased when the bevel angle changed from 60° to 90°, which promotes the formation of a coarse grain structure. The reason for this phenomenon is that the arc and molten metal contacted a larger area when the bevel angle was larger, so that the solid metal phase easily conducted more heat to expand the overheated zone [97].

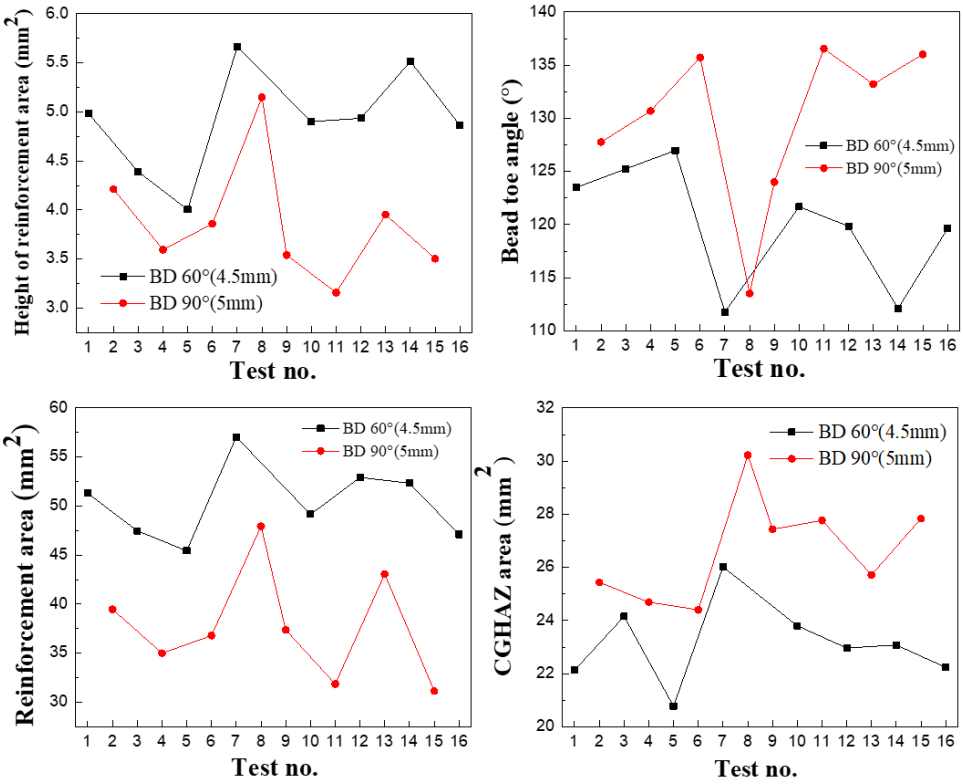

Figure 4.14 Measurements of reinforcement area, bead toe angle, height of reinforcement area and CGHAZ area for the two bevel specifications.

The BD had a smaller effect on the weld geometry (SPR and AR) and dilution than HI, V, and TS, as shown in Table 4.6. The dominant effect of heat input, rather BD, on dilution was discussed in Subsection 4.3.5. The values of SPR and AR are calculated from the bead width (BW). The smaller effect of BD on the BW can be explained in terms of the main liquid metal flow pattern and surface tension in the molten pool. The main flow pattern of liquid metal in the molten pool, as defined by Chen et al., is liquid metal flowing upward along the boundary of the molten pool and colliding at the top of the weld, whereupon the liquid metal changes direction and descends into the pool [97].

The main flow pattern of liquid metal and surface tension are governed the BW and they are affected by active elements, such as O, S, Si, and Ni, dissolved in the liquid mixture metal. This has been studied by Chen et al. [97] and Ribic et al. [99]. The BW is controlled by the surface tension force since it pulls liquid metal towards the center of the weld pool, which is varied by the concentration of the active elements. Kannan et al. [100] also confirmed that bead width depends

on the concentration of surface active elements and the local temperature profile. In this study, the composition of the base metal X70 steel, the electrodes and the granular flux were uniform and identical for all 16 fabricated weldments. This means that the main flow pattern, surface tension and BW were not altered even for different bevel angles and bevel depths. Therefore, the BD had little influence on the weld geometry ratio.

4.6 Signal-to-Noise (S/N) Ratio Analysis

The S/N ratio was utilized to determine the optimized levels for each welding parameter. The welding parameters were categorized by two quality requirements, which are "lower-the-better" and "higher-the-better", respectively. AR, BTA, APR, and BW are included in "higher-the-better" quality requirements. Dilution, CGHAZ area, HRA, and RA are included in "lower-the-better" quality requirements. The S/N ratio analysis was not conducted on the micro-hardness profiles since there was not agreement on which approach was better. The S/N ratio was calculated using Equations 2.3 and 2.4 in Chapter 2.

A higher average S/N ratio value representing a given level of the weld parameter resulted in an optimal effect on the geometric characteristics, since higher S/N values mean lower noise effects [6], [8], [50], [51]. A weld parameter level with a higher S/N value is considered as the optimized parameter level, which results in an optimal effect on the geometric characteristics. The calculated S/N ratio values for the weld characteristics are shown in Appendix A (Table A2). Based on the calculated S/N ratio values, the optimized levels for the CWTSAW parameters are summarized (Table 4.7). Overall, the optimal geometric characteristics are achieved using optimized levels of CWTSAW parameters; i.e., 1.6 kJ/mm for HIL (level 1), 1.3 kJ/mm for HIT (level 1), 21.2 mm/s for TS (level 1), and 25mm^2 for BD (level 2).

Table 4.7 Optimized levels of cold-wire TSAW parameters

Criteria	Characteristics	CWFS (mm/s)	HIL (kJ/mm)	HIT (kJ/mm)	VL (V)	VT (V)	TS (mm/s)	BD (mm^2)
Higher-the-better	BW	33.9	1.6	1.3	36	37	21.2	25
	AR	25.4	1.8	1.5	33	34	23.3	25
	BTA	16.9	1.6	1.3	36	37	21.2	25
	SPR	25.4	1.8	1.5	33	34	23.3	25
Lower-the-better	RA	33.9	1.8	1.3	36	37	21.2	25
	CGHAZ Area	16.9	1.6	1.3	36	37	23.3	12
	Dilution	25.4	1.6	1.3	33	34	21.2	25
	HRA	33.9	1.6	1.3	36	37	21.2	25

4.7 Conclusions

The influence of cold wire addition in CWTSAW on geometrical measurements and micro-hardness profiles of the HAZ in heavy gauge X70 line pipe steels has been studied and optimized parametrically. The following general conclusions can be made:

1. TS, VL and VT were significant parameters that influenced the bead shape and penetration profile.
2. BD significantly influenced the geometrical results, such as HRA, BTA, RA and CGHAZ area; however, BD had less influence on the micro-hardness profile.
3. The CWFS was the significant parameter for CGHAZ and WM hardness, since the cold wire affected the local thermal profile by absorbing heat from the molten pool.
4. A CWTSAW process with an HIL of 1.3 kJ/mm and HIT of 1.6 kJ/mm, a travel speed of 21.2 mm/s, a 90° bevel angle and a bevel depth of 5 mm improved the overall geometrical characteristics.

Chapter 5: A study of CWTSAW Influence in Microstructure and Properties of CGHAZ

In this chapter, the effect of CWTSAW on microstructure and mechanical properties in the CGHAZ of heavy gauge X70 steel is studied. In the previous chapter, parametric optimization was conducted on the CWTSAW process parameters that were correlated with weld geometry characteristics, the amount of dilution and micro-hardness of the WM and CGHAZ. The optimized set of welding parameters determined in Chapter 4 (Table 3.6) are utilized in this chapter. A description of the visual inspection of weld appearance before and after optimization of parametric study is presented. Next, the trends for impact absorbed energy and the variation in micro-hardness are expressed and correlated with the morphology and distribution of MA constituents and the PAG size in the CGHAZ. The ferrite/bainite (α/B) grain misorientation within the CGHAZ obtained from EBSD is also presented. Then, analysis of fracture morphology is conducted on Charpy V-notch (CVN) samples and the appropriate fracture mechanisms are defined. Finally, analysis of the actual heat input in the HAZ and welding productivity of CWTSAW are discussed.

5.1 Weld Visual Appearance

A comparison of weld appearance was done on the welds using the original parameter levels and optimized levels and is shown in Figure 5.1. The actual view of the weld (left image) and the projection view of the weld (right image) are shown in Figure 5.1. Nonuniform bead shapes are observed in Figure 5.1-a and c (see arrows) for weld test numbers, T1 and T10. An improved weld appearance (Figure 5.1-b and d) was observed for welds (CW40 and CW80) using optimized parameter levels. This improvement in the weld appearance supports the validity and feasibility of the parametric study on weld geometry.

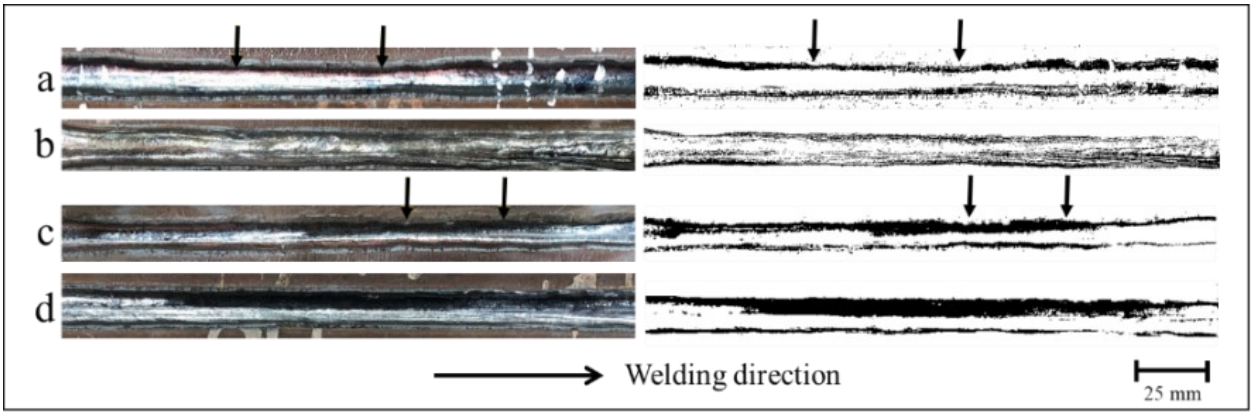

Figure 5.1 Appearance of weldments fabricated by CWTSAW at CWFS of 16.9 mm/s (a, b) and 33.9 mm/s (c, d) before optimization (a, c) and after optimization (b, d). Arrows indicate regions with defects.

5.2 Charpy Impact Toughness

The average absorbed energy for the CVN samples as a function of test temperature is shown in Figure 5.2. A detailed description of CVN testing, testing temperature and welding parameter inputs for tests was presented in Chapter 3. All tests were conducted using the same heat input, voltage and bevel specification, except for cold wire feed speed (CWFS) and travel speed (TS). The CW0-Ref. samples were fabricated without cold wire addition and TS is at 21.2 mm/s. The CW40 and CW80 samples were produced for CWFS of 16.9 mm/s (40 in/min) and 33.9 mm/s (80 in/min), respectively, with TS at 21.2 mm/s (50 in/min) for both welds. The CW40-TS60 sample was fabricated using CWFS of 16.9 mm/s (40 in/min) and TS of 25.4 mm/s (60 in/min). The samples welded using the optimized parameters and a CWFS of either 16.9 or 33.9 mm/s exhibit high absorbed energy for test temperatures >40 °C. The lowest energy absorbed was observed for the weld without cold wire addition. A “bump” in the absorbed energy is observed in the CW40 and CW40-TS60 samples at -30 °C. The mechanism that would account for this “bump” is not known but it appears to be related to the large scatter of absorbed energy at DBTT [31].

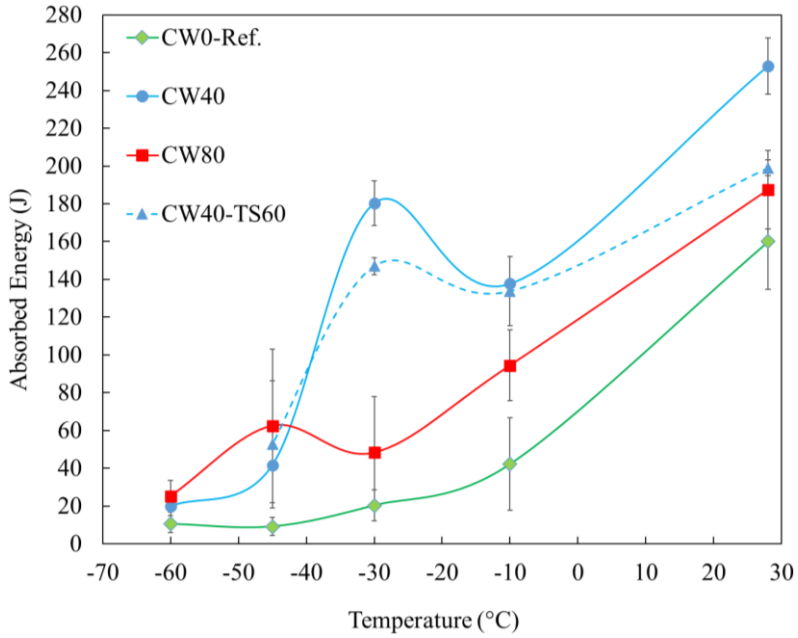

Figure 5.2 Average absorbed energy for CWTSAW welds at various cold wire feed rates and travel speeds as a function of testing temperature.

The fracture energy for each weld was calculated by averaging the absorbed energy results between the room temperature and -60°C, as shown in Table 5.1. The averaged absorbed energy quantitatively described the overall performance of each sample in Charpy tests. The highest absorbed energy is 136.5 J for the CW40 samples. The lowest absorbed energy is 85.3 J for the CW0-Ref. samples. The samples fabricated with a CWFS of 16.9 mm/s (CW40 and CW40-TS60) absorbed more energy than the other samples.

The variation in fracture toughness depends significantly on microstructure. Specifically, the fraction, size and distribution of MA constituents and the PAG size are significantly influenced by the local thermal cycles and cooling rate [62], [76], [77]. The correlation between the fracture toughness and microstructure is discussed in Section 5.9.

Table 5.1 Calculated average fracture energy of CWTSAW welds

Weld ID	Calculated fracture energy (J)
CW0-Ref.	85.3
CW-40	136.5
CW-80	106.4
CW40-TS60	125.8

5.3 Micro-hardness

The average micro-hardness values measured for the WM, CGHAZ, FGHAZ, ICHAZ and BM as a function of normalized distance to the fusion line are shown in Figure 5.3. The hardness is highest in the WM with the lowest values at the FGHAZ/ICHAZ interface. The CW40 and CW40-TS60 samples have lower hardness values in both the CGHAZ and GHAZ compared with the CW0-Ref. and CW80 samples. This difference will be discussed when the microstructures of CW0-Ref., CW40 and CW80 samples are considered. Detailed analysis of the MA constituents and grain size in the CGHAZ for each of weld tests and their effects on hardness will be discussed in Sections 5.4, 5.5 and 5.9.

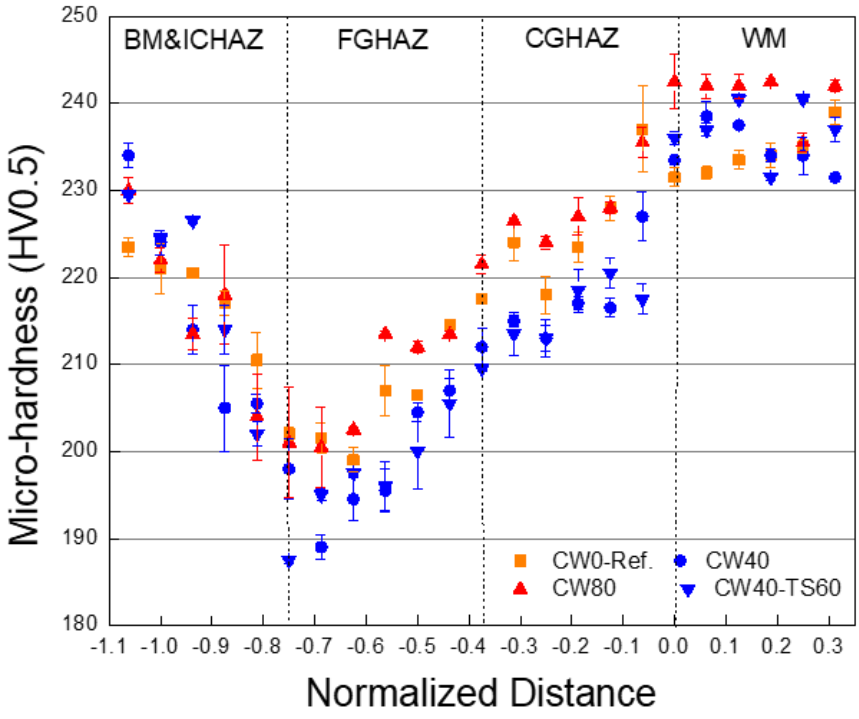

Figure 5.3 Average micro-hardness values within the WM, CGHAZ, FGHAZ, ICHAZ and the BM for various weld conditions.

5.4 PAG and Grain Misorientation Analysis

This section includes measurement of PAG size for the CW0-Ref., CW40 and CW80 samples in the CGHAZ. In addition, the size and misorientation angle of ferrite and banite grains are presented.

5.4.1 Prior Austenite Grains (PAG) - Optical Imaging

Optical micrographs of the PAG boundaries in the CGHAZ of CW0-Ref., CW40 and CW80 samples are shown in Figure 5.4. The detailed etching and measurement methods for PAG boundaries and size were presented in Chapter 3. Each OM micrograph was taken from a location 3 mm below the weld surface and 50-200 µm from the fusion line. After etching, the PAG boundaries were revealed and are marked with dashed lines in Figure 5.4. The weld is located on the left side of each figure. The average PAG size is 72.5 (2.8), 52.3 (2.7) and 39.9 (2.0) µm for CW0-Ref., CW40 and CW80 samples, respectively. The values in the brackets are one standard deviation. Refinement of the PAG size occurs as the cold wire travel speed is increased. SEM results for each of the samples are presented in Subsection 5.4.2.

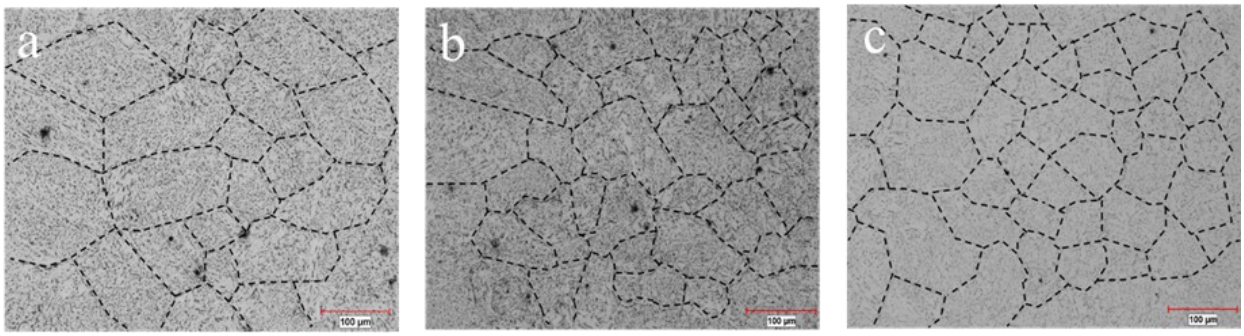

Figure 5.4 OM micrographs of PAG boundaries in the CGHAZ of a) CW0-Ref., b) CW40 and c) CW80.

5.4.2 Prior Austenite Grains (PAG) - SEM Imaging

SEM micrographs of the PAG boundaries in the CGHAZ of the CW0-Ref., CW40 and CW80 samples are shown in Figure 5.5. The PAG boundaries are revealed as white lines and are indicated with arrows. Three SEM micrographs were taken from a location 3 mm below the weld surface and 50-200 µm from the fusion line for the PAG size measurement. The PAG size is 71.1 (3.5), 48.2 (2.2) and 34.0 (2.0) µm for the CW0-Ref., CW40 and CW80 samples, respectively. The

values in the brackets are one standard deviation. Qualitatively, the PAG size tendency shown in the OM results is supported by the SEM images.

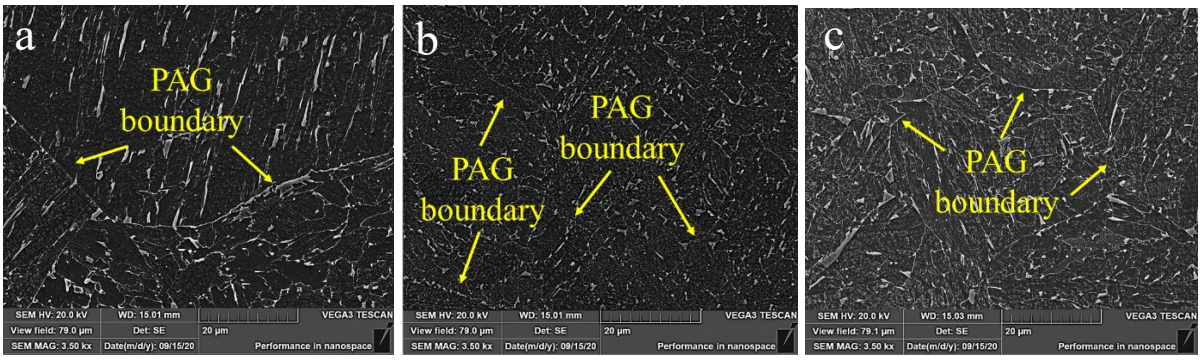

Figure 5.5 SEM SE micrographs of the CGHAZ in a) CW0-Ref., b) CW40 and c) CW80 showing PAG boundaries.

The samples shown in Figure 5.5 were all welded with identical heat inputs (2.9 kJ/mm for the lead and trail electrodes - Table 3.7). Li et al [62], [101] reported that increasing welding heat input promoted the growth of PAG. In this study, the cold wire addition absorbed heat from the molten pool resulting in a variation of the local thermal cycle. As the cold wire feed speed (CWFS) was increased from zero (0) to 33.9 mm/s, the actual heat input and peak temperature in the CGHAZ decreased. Therefore, the smallest PAG size (39.9 µm) occurred in the CGHAZ of the CW80 sample due to the relative fast cooling rate and low peak temperature in the CGHAZ. Detailed actual heat input analysis is presented in Subsection 5.8.

5.4.3 Misorientation between Ferrite/Bainite (α/B) Grains

The α/B grains in the CGHAZ of the CW0-Ref. and CW40 samples were analyzed using EBSD mapping, as shown in Figure 5.6. The ferrite/bainite grain boundaries exhibited similar features via EBSD mapping which made them difficult to separate. A 250 by 200 µm map with a 1 µm step size was selected for the EBSD mapping process. A 15° misorientation of two adjacent grains was considered as the transition from low angle to high angle grain boundaries and the high angle grain boundaries (>15°) treated as obstacles during fractrure propagation have a dominant effect on the properties of the weld [30][82]. As such, a 15° misorientation angle was selected to identify α/B grain boundaries. At least four regions were analyzed and around 100 grains were measured for the EBSD micrographs. The measured gain sizes for CW0-Ref. and CW40 samples

were 20.0 µm (1.6) and 16.1 µm (1.3), respectively. The cold wire addition at a 16.9 mm/s feeding rate resulted in refinement of the α/B grain size.

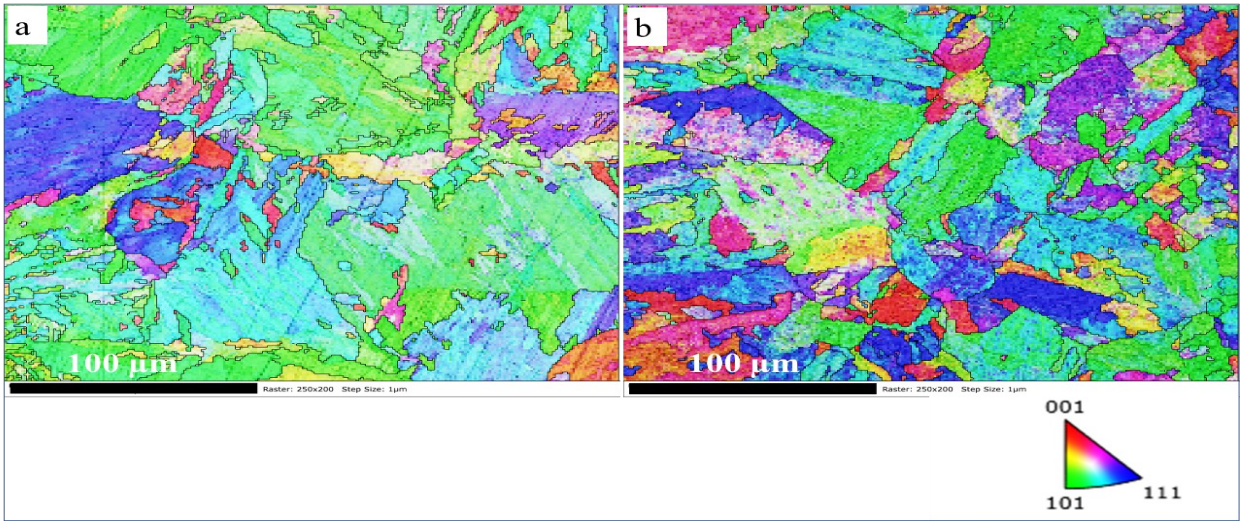

Figure 5.6 Examples of EBSD maps showing ferrite and bainite grain boundaries, defined as misorientations greater than 15º, in the CGHAZ of (a) CW0-Ref. and (b) CW40 samples.

Figure 5.7 shows the fraction of grains with a specific misorientaion for both CW0-Ref. and CW40 samples. The CW0-Ref. sample has a larger fraction of grain boundaries with a misorientation angle from 35° to 41° than the CW40 sample. For misorientation angles greater than 43°; however, the fractions are similar for the two samples. Except for the difference in the grain size, the variation in fracture toughness may rely more on the MA constituents than on the ferrite/bainite microstructure. This is discussed in Section 5.9.

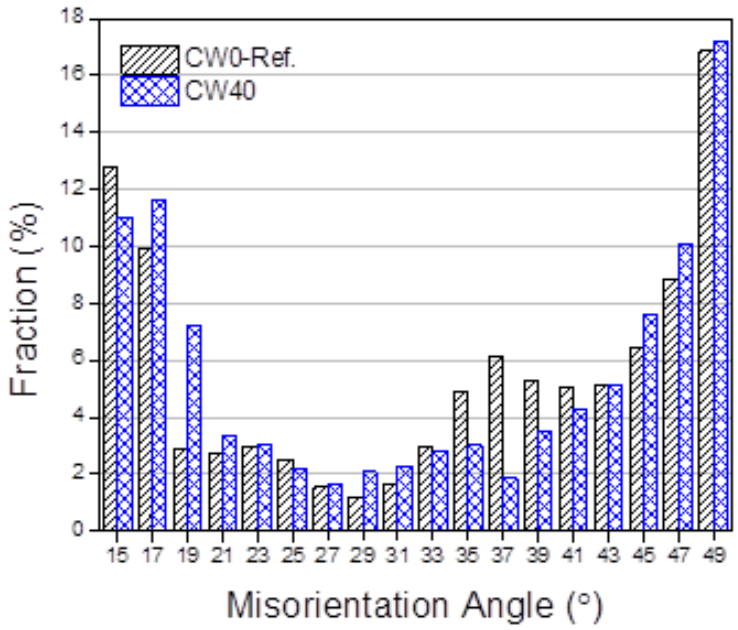

Figure 5.7 Ferrite and bainite grain boundary misorientation angle distribution in the CGHAZ for the CW0-Ref. and CW40 samples.

5.5 Martensite-austenite (MA) Constituents Analysis

This section includes the measured size and fraction of MA constituents in the CGHAZ for the CW0-Ref., CW40 and CW80 samples. In addition, the size distribution and inter-particle spacing of MA constituents for each weld are presented.

5.5.1 MA Analysis with OM

OM micrographs of the MA constituents in the CGHAZ of the CW0-Ref., CW40 and CW80 samples are shown in Figure 5.8. Three micrographs for each sample were taken from a location 3 mm below the weld surface and 50-200 μm from the fusion line. The size and fraction of MA for each sample were measured using the size measurement and color threshold command of Image J software. The major axis (longest length) of MA constituents were measured. Figure 5.8-a to 5.8-c show MA regions in the CW0-Ref., CW40 and CW80 samples, respectively, which are highlighted in blue by Image J for MA measurements (Figure 5.8-d to 5.8-f).

The MA regions in the CW0-Ref. sample were mainly massive (blocky and concentrated) and elongated. The MA features in the CW40 sample were finer and more dispersed than those in the CW0-Ref. sample. The MA features in the CW80 sample are more elongated than those in the CW0-Ref. sample, and more concentrated than those in the CW40 sample. The MA fraction and size by OM are summarized in Table 5.2. The values in brackets are one standard deviation.

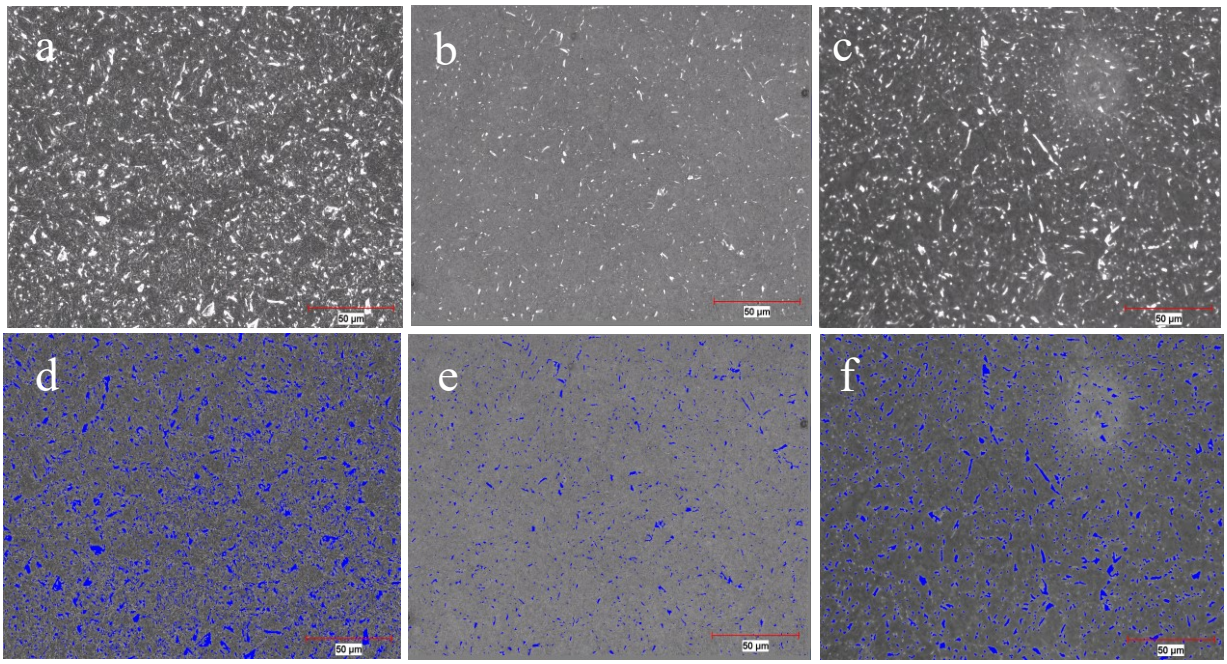

Figure 5.8 OM micrographs of MA constituents in the CGHAZ of CW0-Ref. (a, b), CW40 (b, c) and CW80 (c, f).

5.5.2 MA analysis with SEM

SEM micrographs of MA constituents in the CGHAZ of the CW0-Ref., CW40 and CW80 samples are shown in Figure 5.9. The MA fractions for each weld were also obtained using SEM and measured using Image J. Figure 5.9-a and 5.9-b show blocky and elongated MA regions in the CW0-Ref. sample. Figure 5.9-c and 5.9-d show the fine distribution of MA in the CW40 sample. Figure 5.9-e and 5.9-f show the elongated and blocky MA regions in the CW80 sample. The MA constituents of the CW80 sample are more elongated with a larger size than those in the CW0-Ref. and CW40 samples. The features of MA constituents on SEM micrographs agree with the features from OM micrographs.

The measured MA fractions using Image J for SEM micrographs for each sample are shown in Table 5.2. The values in the brackets are one standard deviation. The MA fractions by SEM for all samples are consistently larger than the measured fraction by OM, since PAG boundaries also exhibit the same white color as the MA constituents in SEM micrographs. The color threshold command of Image J captured both MA constituents and PAG boundaries to process the measurement of MA constituents. Therefore, the MA fraction by SEM is greater than the results by OM and the MA size by SEM is not provided. The trend for MA fraction for OM

and SEM is consistent. The distribution of different MA sizes for each of the welds is presented in the next subsection.

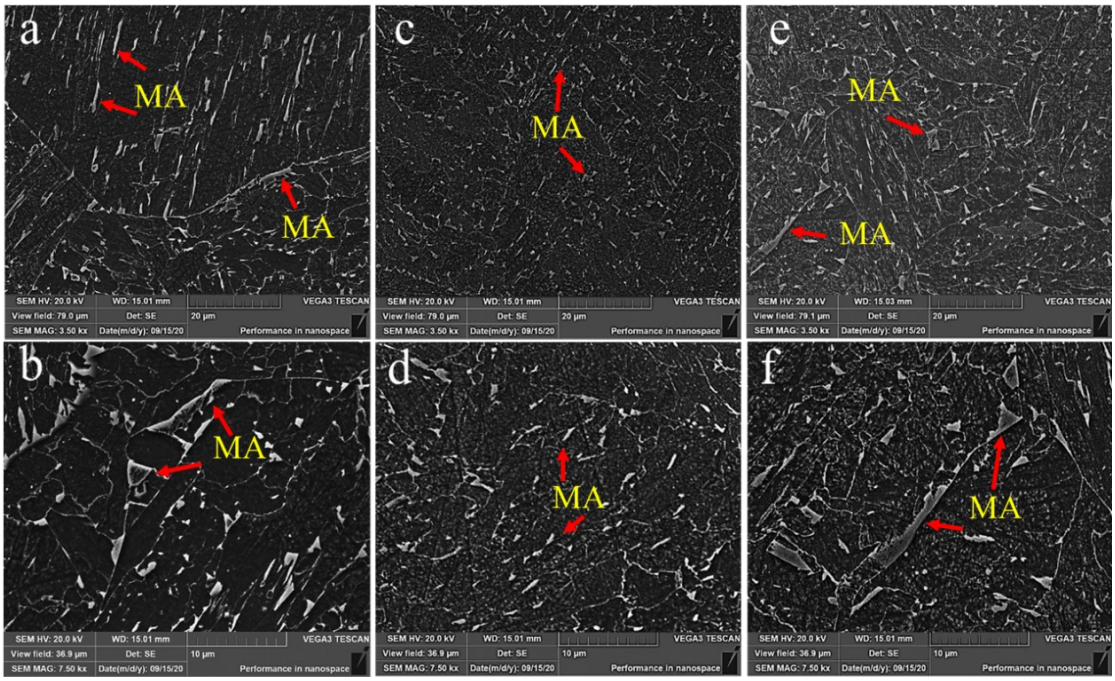

Figure 5.9 SEM SE micrographs of MA in the CGHAZ of CW0-Ref. (a, b), CW40 (c, d) and CW80 (e, f) at low (a-e) and high (b-f) magnification.

Table 5.2 Summary of the MA measurements for each of the welds

MA measurements		CW0-Ref.	CW40	CW80
Size (μm)		0.82 (0.01)	0.75 (0.04)	**1.16 (0.04)**
Fraction (%)	OM	5.2(0.2)	2.8 (0.2)	**5.9 (0.2)**
	SEM	6.3 (0.3)	3.5 (0.2)	**6.5 (0.2)**

* Maximum values are indicated in bold font and minimum values are underlined for each row.

5.5.3 Distribution and Spacing of MA

The size distribution of MA constituents for each of the welds is provided in Figure 5.10. The feature sizes were determined by measuring the major axis (longest length) of MA constituents using Image J for optical micrographs. The feature sizes of MA constituents were not measured using SEM micrographs since the PAG boundaries also exhibit the same white color as the MA constituents in SEM micrographs. Approximately one thousand MA constituents were captured for each OM micrograph using Image J. All particles measured as 0.2 μm in length (1 pixel in the OM micrographs) were treated as noise/outliers and removed by Image J.

Figure 5.10 shows that 45% of the MA constituents for the CW0-Ref. sample are 1 μm or smaller, while 55% of the MA constituents for the CW40 sample and 33% of the MA constituents for the CW80 sample are 1 μm or smaller. The major axis of some MA constituents in CW0-Ref. and CW80 samples (Figure 5.9-b and f) reflects in the large size distribution of MA constituents (>6 μm) in Figure 5.10-a and c.

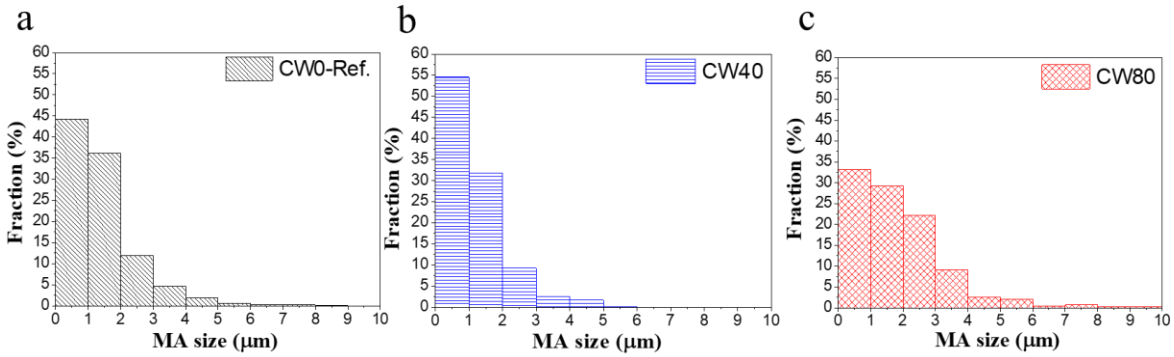

Figure 5.10 MA size distribution in the CGHAZ for CWTSAW welds of a) CW0-Ref., b) CW40 and c) CW80.

Equation 5.1 [102] was utilized to determine the mean inter-particle spacing for the MA constituents in the CGHAZ of the samples.

$$\lambda_p = \frac{\pi d_p^2}{2\sqrt{3}\,V_p} - \frac{\sqrt{2}d_p}{\sqrt{3}} \tag{5.1}$$

where λ_p, d_p and V_p are the mean inter-particle spacing, the mean MA size (Table 5.2) and the volume fraction of MA constituents, respectively. The mean MA size is the mean major axis length of MA constituetns. The mean inter-particle spacing, along with the measured mean sizes and fractions in Table 5.3 are discussed in Section 5.6.

5.6 Summary of Microstructural Results

The measured and calculated microstructural results for each of the welds are summarized in Table 5.3. Included in the table are the PAG size, size, fraction and inter-particle spacing of MA constituents and the ferrite/bainite (α/B) grain size for each of the welds. The CW0-Ref. sample has the largest PAG and α/B grain sizes at 72.5 and 20.0 μm, respectively. The maximum size, fraction and inter-particle spacing for the MA constituetns occur for the CW80 sample. Conversely, the minimum size and fraction of MA occur for the CW40 sample. Overall, there is a denser

distribution of MA for the CW0-Ref. sample and a larger size distribution of MA for CW80 sample compared with the finer distribution of MA for the CW40 sample.

Table 5.3 Summary of microstructural results for each of the welds

Microstructural Results			CW0-Ref.	CW40	CW80
Size of PAG (μm)		OM	**72.5 (2.8)**	52.3 (2.7)	39.9 (2.0)
		SEM	**67.2 (3.5)**	48.2 (2.2)	34.0 (2.0)
MA constituents	Size (μm)		0.82 (0.01)	0.75 (0.04)	**1.16 (0.04)**
	Fraction (%)	OM	5.2 (0.2)	2.8 (0.2)	**5.9 (0.2)**
		SEM	6.3 (0.3)	3.5 (0.2)	**6.5 (0.2)**
	Spacing (μm)		10.9 (1.5)	17.7 (1.1)	**19.5 (1.9)**
Size of α/B Grain (μm)			**20.0 (1.6)**	16.1 (1.3)	-

* Maximum values are indicated in bold font and minimum values are underlined for each row.

5.7 Fracture Morphology Analysis

This section includes optical macrographs and SEM micrographs of the fracture surfaces for each of the samples tested at -30 and -45°C. The fracture surfaces are characterized to determine the relative amount of brittle and ductile fracture.

5.7.1 Optical Macrographs of the Fracture Surface

Optical macrographs of the fracture surface for the CW0-Ref., CW40 and CW80 CVN samples tested at -30°C are shown in Figure 5.11. The fracture surface of the CW0-Ref. sample is shiny and flat indicating brittle failure. The fracture surface of the CW40 sample shows shear lips and a dull fibrous surface indicative of ductile fracture. The fracture surface of the CW80 sample contains both a flat and shiny region and a fibrous region. Qualitatively, the facture surface of the CW40 sample exhibits more ductile behavior than the CW80 sample.

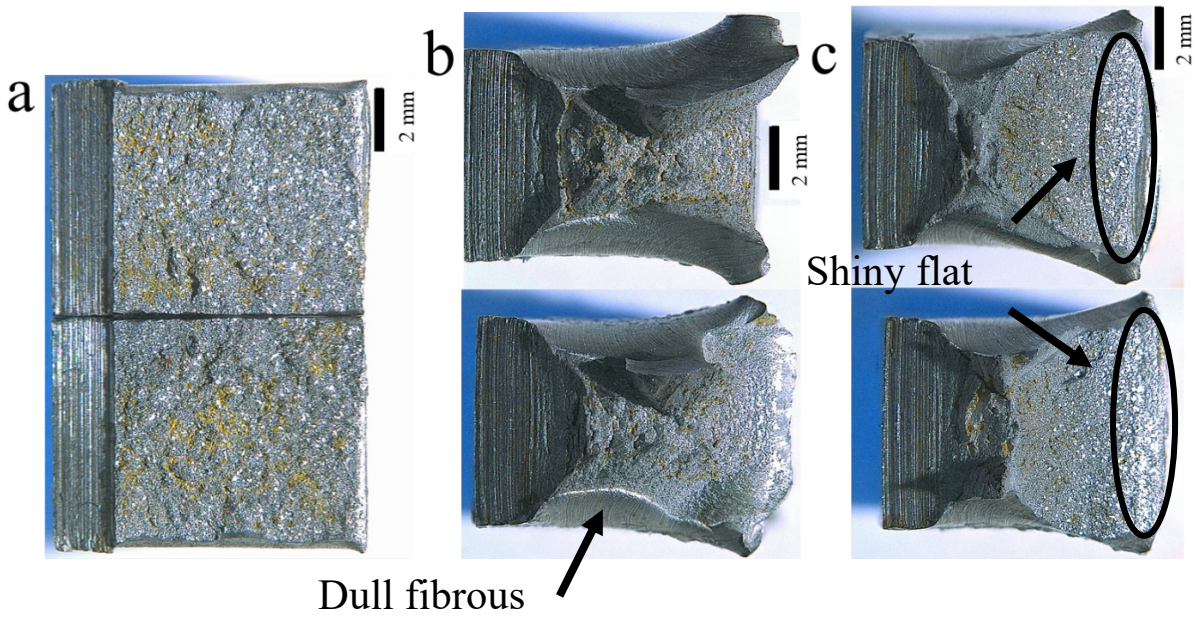

Figure 5.11 Optical macrographs of fracture surfaces after testing at -30°C for the a) CW0-Ref., b) CW40 and c) CW80 samples.

5.7.2 SEM Micrographs of the Fracture Surface

SEM micrographs of the fracture morphology for the CW0-Ref., CW40 and CW80 CVN samples tested at -30°C are shown in Figure 5.12. The presence of river patterns on the fracture surface of the CW0-Ref. sample indicate cleavage fracture (brittle fracture). The extensive brittle fracture surface corresponds to the low absorbed energy (20 J). Ductile dimples are the main feature of the CW40 sample fracture surface, indicating a microvoid coalescence (MVC) mechanism. This behavior correlates with the high absorbed fracture energy (180 J). Both ductile and brittle features, i.e., dimples and a river pattern, appear on the CW80 sample fracture surface indicating quasi-cleavage fracture. Quasi-cleavage fracture is defined as the fracture model consisting of the characteristics of dimples rupture fracture and cleavage fracture; examples are indicated with arrows in Figure 5.12. The low relatively absorbed energy value (48 J) is indicative of the fracture mechanism.

The presence of quasi-cleavage facets is related to the initiation and propagation of cracks through the MA constituents [63], [77], [93], [103]. The inferior fracture toughness of the CW80 sample relative to the CW40 sample correlates with the elongated MA constituents and their high volume fraction, both of which promote cleavage crack initiation and propagation.

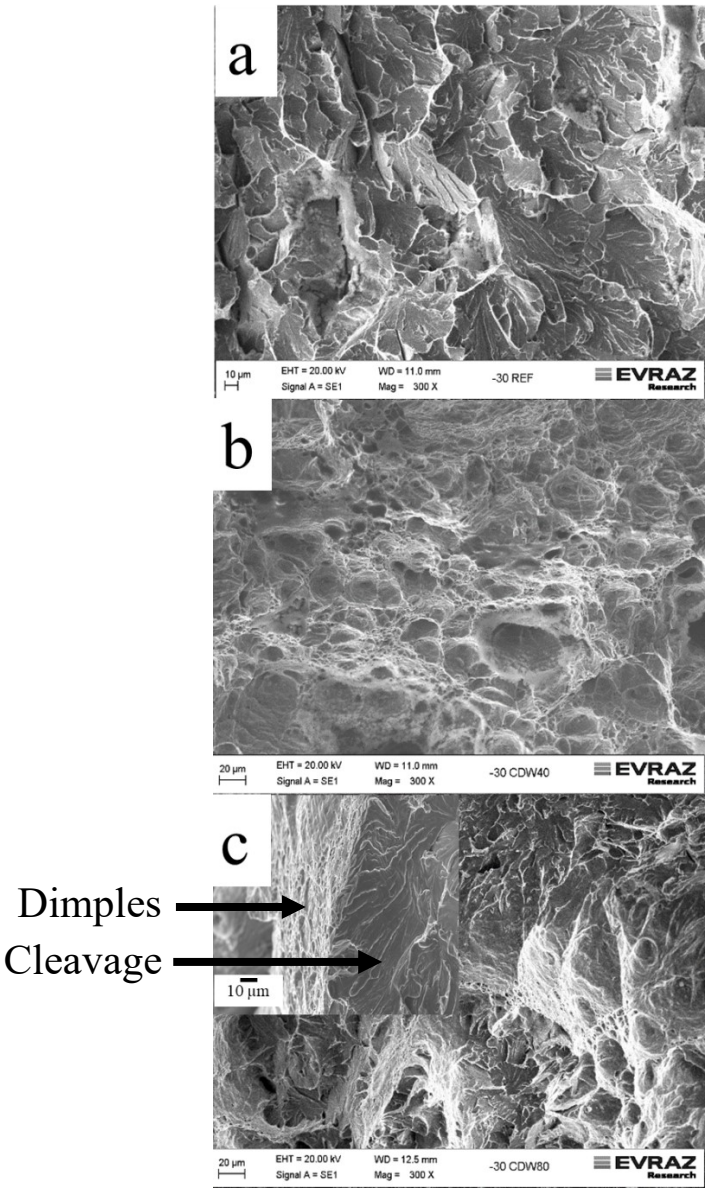

Figure 5.12 SEM micrographs of the fracture morphology after testing at -30°C for a) CW0-Ref., b) CW40 and c) CW80 samples.

SEM micrographs of the fracture morphology for the CW0-Ref., CW40 and CW80 CVN samples tested at -45 °C are shown in Figure 5.13. All samples exhibited cleavage failure, which correlates with the lower absorbed energy values. The absorbed energy for CW0-Ref, CW40 and CW80 are 9.2, 41.8 and 62.5 J, respectively. The finer cleavage facets (indicated with arrows in Figure 5.13) for the CW80 sample are due to the finer PAG size in the CGHAZ. This phenomenon was observed Lan et al. [60] for weld samples with relatively low heat input. The heat input analysis for each of the welds is presented in Section 5.8.

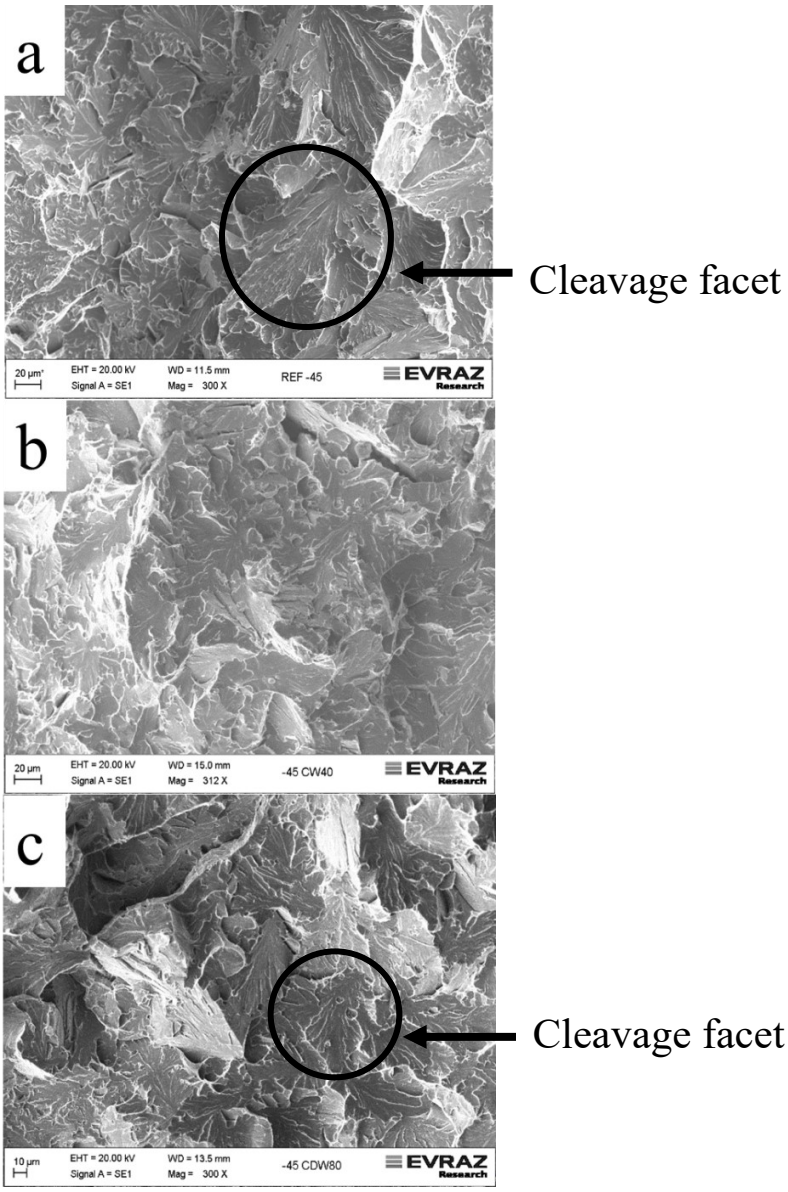

Figure 5.13 SEM micrographs of the fracture morphology after testing at -45°C for the a) CW0-Ref., b) CW40 and c) CW80 samples.

5.8 Heat Input Analysis

This section includes different methods for determining the heat balance and ultimately the heat input during welding. The calculations include the enthalpy change for cold wire fusion, the arc instability method and the actual heat input method. The cooling rate from 800°C to 500°C is calculated based on the actual heat input.

5.8.1 Enthalpy Change for Cold Wire Fusion ($\Delta H_{Fusion-CW}$)

The nominal heat input is a combination of the heat input for the lead and trail electrodes. The cold wire consumes some of the heat from the weld pool which influences the amount of actual heat input. The actual heat input (HI_{Act}) and cooling rate (CR) are closely related to the enthalpy change associated with the cold wire addition.

Mohammadijoo et al. [7] applied a heat balance approach to welded 13.4 mm thick X70 line pipe steels. Four equations were used to analyze the actual heat input in the CWTSAW process; i.e., Equations 5.2 to 5.5. The enthalpy change during cold wire fusion is given by:

$$\mathbf{\Delta H_{Fusion-CW}}\left(\frac{\text{kJ}}{\text{mm}}\right) = \frac{\text{FS.A.}\rho}{1000.\text{TS}}.\left\{\Delta H^{\circ}_{298} + \int_{25+273}^{1510+273} C_p^s\,.\,dT + \Delta H_{\alpha\rightarrow\gamma} + \Delta H_{\gamma\rightarrow\delta} + \Delta H_l + \int_{1510+273}^{2000+273} C_p^l.\,dT\right\} \quad (5.2)$$

where FS, A, ρ and TS (mm/s) are the feed speed, cross-sectional area of the electrodes, density of the cold wire, travel speed, respectively; C_p^s and C_p^l are the specific heat capacities of the solid and molten electrode. ΔH°_{298} and ΔH_l are the standard enthalpy change at 25 °C (298 K) and the latent heat of fusion for the cold electrode, respectively. The physical properties of the cold wire utilized in Equation 5.2 are assumed to be similar to those of a structural steel from a European standard [104], which were also used in the heat transfer analysis in steel structures published by Narang et al. [105]. The initial temperature (25 °C), melting point of the solid electrode (1510 °C) and the temperature of the molten electrode (2000 °C) used for the enthalpy change in Equation 5.2 are taken from the standard for the structural steel [104]. The feed speed and travel speed are shown in Table 3.7 and the values of characteristics and thermodynamic properties for the cold wire utilized for the heat balance approach are shown in Table 5.4. The latent heats of phase transformation, alpha ferrite to austenite ($\Delta H_{\alpha\rightarrow\gamma}$) and austenite to delta ferrite ($\Delta H_{\gamma\rightarrow\delta}$), for pure iron are also

included in Equation 5.2, since these phase transformations occur in the temperature range from 25 to 2000 °C.

Table 5.4 Characteristics and thermodynamic properties utilized for the heat balanced approach [104], [105]

Characteristics of cold wire and standard enthalpy change	
Density (ρ)	$7.87 \cdot 10^{-3}$ (kg/cm^3)
Latent heat of fusion (ΔH_l)	270 (kJ/kg)
Cross-section area (A)	0.13 (cm^2)
Standard enthalpy change (ΔH°_{298})	0 (kJ/kg)
Latent heats of phase transformation for pure iron	
Alpha ferrite to austenite ($\Delta H_{\alpha \rightarrow \gamma}$)	16 (kJ/kg)
Austenite to delta ferrite ($\Delta H_{\gamma \rightarrow \delta}$)	15 (kJ/kg)
Specific heat capacity of electrodes and cold wire	
Temperature (**°C**)	Specific heat capacities [J/(kg·K)]
25-600	$425 + 0.773T - 1.69 \cdot 10^{-3}T^2 + 2.22 \cdot 10^{-6}T^3$
600-735	666 + [13002 / (738- T)]
735-900	545 + [17820 / (T-731)]
900-1510	650
1510-2000 (liquid)	820

The enthalpy changes for cold wire fusion of the weld samples were calculated and are shown in Table 5.5. The enthalpy change increases as the cold wire feed speed increases. In addition, the value of this change is important for heat reduction on the nominal heat input ($HI_{Nominal}$), since the cold wire consumes some amount of the heat input for fusion.

Table 5.5 Enthalpy changes for cold wire fusion of the weld samples

	CW0-Ref.	CW40	CW80
$\Delta H_{Fusion-CW}$ (kJ/mm)	0	0.16	0.32
$HI_{Nominal}$ (kJ/mm)	2.9	2.9	2.9

5.8.2 Enthalpy Change Associated with Arc Instability ($\Delta H_{Arc-instability}$)

The enthalpy change associated with arc instability in CWTSAW process is related to the current and voltage recorded for the lead and trail electrodes. The current and voltage were recorded at 0.5 s intervals during the process, but did not remain at the nominal values since the cold wire addition into the welding pool caused fluctuations in the voltage and current settings. Three sets of recorded voltage and current values for the lead and trail electrode were averaged and the variation in voltage and current, expressed as one standard deviation in brackets, is indicated in Table 5.6. The enthalpy change due to arc instability is given by Equation 5.3 [7]:

$$\boldsymbol{\Delta H_{Arc-instability}}\left(\frac{kJ}{mm}\right) = \frac{60}{1000 \cdot TS} \cdot \{[(V \cdot I)_L + (V \cdot I)_T]_{Nominal} - [(V \cdot I)_L + (V \cdot I)_T]_{Recorded}\} \quad (5.3)$$

where $\Delta H_{Arc-instability}$ is defined as the energy difference between the nominal input and recorded values of voltage (V) and current (I). The variation in current and voltage and the enthalpy changes associated with arc instability are shown in Table 5.6. The enthalpy change due to arc instability increased as the cold wire feed speed increased.

Table 5.6 Variation in welding parameters and enthalpy changes due to arc instability for the weld samples

Welding parameters		CW0-Ref.	CW40	CW80
I-Lead (A)	Nominal	1100	1100	1100
	Recorded	1100	1095.9 (0.2)	1099.2 (0.1)
I-Trail (A)	Nominal	825	825	825
	Recorded	825	823.5 (0.1)	823.9 (0.1)
V-Lead (V)	Nominal	31	31	31
	Recorded	31	30.2 (0.2)	30.0 (0.1)
V-trail (V)	Nominal	33.5	33.5	33.5
	Recorded	33.5	33.3 (0.2)	30.8 (0.2)
$\Delta H_{Arc-instability}$ (kJ/mm)		0	0.06	0.16

5.8.3 Actual Heat Input (HI_{Act})

The actual heat input was determined by incorporating a correction factor (η) to account for the loss in heat due to cold wire fusion and arc instability. The correction factor is given in Equation 5.4.

$$\boldsymbol{Correction\ factor}: \eta = 1 - \frac{\Delta H_{Fusion-CW} + \Delta H_{Arc-instability}}{HI_{Nominal}} \tag{5.4}$$

where $HI_{Nominal}$is the nominal heat input corresponding to the sum of the lead and trail electrode nominal heat inputs (HI-Lead and HI-Trail - Table 3.7). Then the actual heat input (HI_{Act}) is determined as follows:

$$\boldsymbol{HI_{Act}}(\frac{kJ}{mm}) = \eta \cdot HI_{Nominal} \tag{5.5}$$

The calculated correction factors and actual heat inputs are shown in Table 5.7. The CW0-Ref. sample has the same HI_{Act} as $HI_{Nominal}$, since there is no cold wire, while HI_{Act} decreases as the cold wire feed speed increases.

5.8.4 Cooling Rate (CR)

Poorhaydari et al. [106] estimated the cooling rate (CR) for thick welding plates according to the Rosenthal equations.

$$\boldsymbol{\Delta t_{8-5}(s)} = \frac{HI_{Act}}{2\pi\lambda} \cdot (\frac{1}{500-T_0} - \frac{1}{800-T_0}) \tag{5.6}$$

$$\boldsymbol{CR}\ \left(\frac{^\circ C}{s}\right) = \frac{300}{\Delta t_{8-5}} = \frac{2\pi\lambda \cdot (800-T_0) \cdot (500-T_0)}{HI_{Act}} \tag{5.7}$$

where Δt_{8-5} is the weld time constant, which is the cooling time from 800 °C to 500 °C, T_0 is the initial temperature (25 °C) and λ is the thermal conductivity (41 [J/ (s·m·°C)]). Calculated CR and Δt_{8-5} values are given in Table 5.7. There is an increase in cooling rate and a decrease in Δt_{8-5} as the cold wire feed speed increases.

Table 5.7 Calculated actual heat input, CR, and Δt_{8-5} for the weld samples

	CW0-Ref.	CW40	CW80
$HI_{Nominal}$ (kJ/mm)	2.9	2.9	2.9
Correction factor (η)	1	0.9	0.8
HI_{Act} (kJ/mm)	2.9	2.61	2.32
Δt_{8-5} (s)	9.17	8.26	7.34
Cooling rate (CR) (°C/s)	32.7	36.3	40.9

The actual heat input (HI_{Act}) is correlated with the microstructrual results in Figure 5.14. The MA spacing increased as the HI_{Act} decreased. The MA size is reduced from 0.82 to 0.75 µm with the intermediate value of HI_{Act} (2.6 kJ/mm); however, MA size increases significantly to 1.16 µm with the lowest value of HI_{Act} (2.3 kJ/mm) which corresponds to the fastest CR (40.9 °C/s). The PAG size decreased as the actual heat input decreased. The decrease in MA fraction from 5.21 to 2.79% with HI_{Act} equal to 2.6 kJ/mm and the increase to 5.93% with the lowest value of HI_{Act} (2.3 kJ/mm) are similar to the trend in MA size.

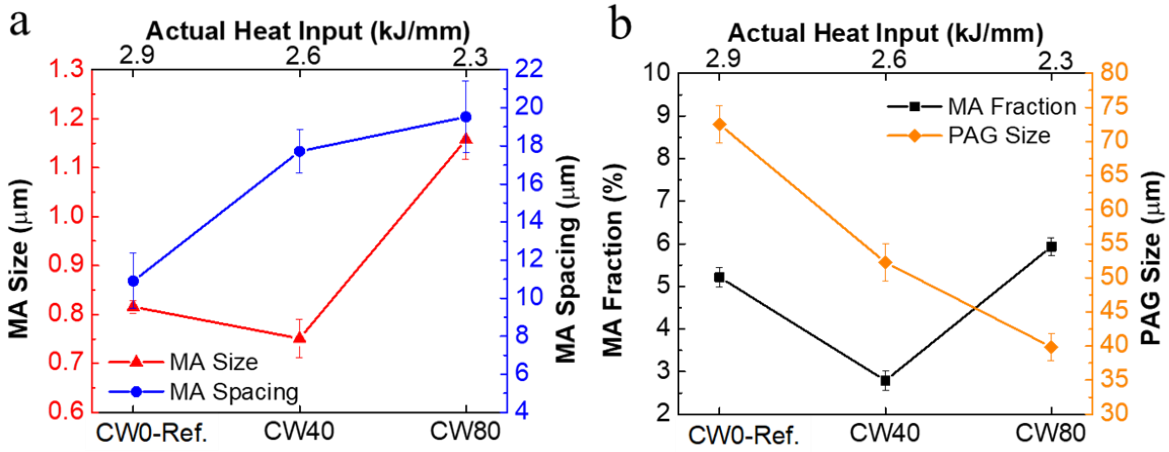

Figure 5.14 a) MA size and spacing and b) MA fraction and PAG size in the CGHAZ vs. cold wire feed speed and actual heat input for the three welded samples.

5.9 Correlation between Microstructure and Properties in the CGHAZ

Poorer fracture toughness and a variation in hardness values were observed for the CW0-Ref. and CW80 samples. The CW40 samples had better fracture toughness. These results can be

correlated with the size, fraction and distribution of the MA constituents [62], [101] and MA morphology is influenced by PAG size [107]–[109].

Li et al. [76], [77] reported elongated and massive MA constituents were formed during relatively fast cooling rates and this morphology is detrimental to fracture toughness. From a fracture mechanism perspective, cleavage fracture is initiated at elongated MA constituents and the cleavage facet size is correlated to the PAG size [66], [67]. Li et al. [62], [101] also discovered that increasing the welding heat input promoted the growth of PAG and that the morphology of the MA constituents was affected by PAG size. In addition, refinement of MA constituents, combined with a reduction in volume fraction and increased inter-particle spacing in the HAZ, are generally accepted as improving toughness in the HAZ [61], [93], [110]–[112].

Overall, the PAG size and MA morphology in the CGHAZ are significantly influenced by welding peak temperature and cooling time [71], [77], [93], [106], [113], [114]. These effects are summarized in Figure 5.15 and discussed in subsequent subsections.

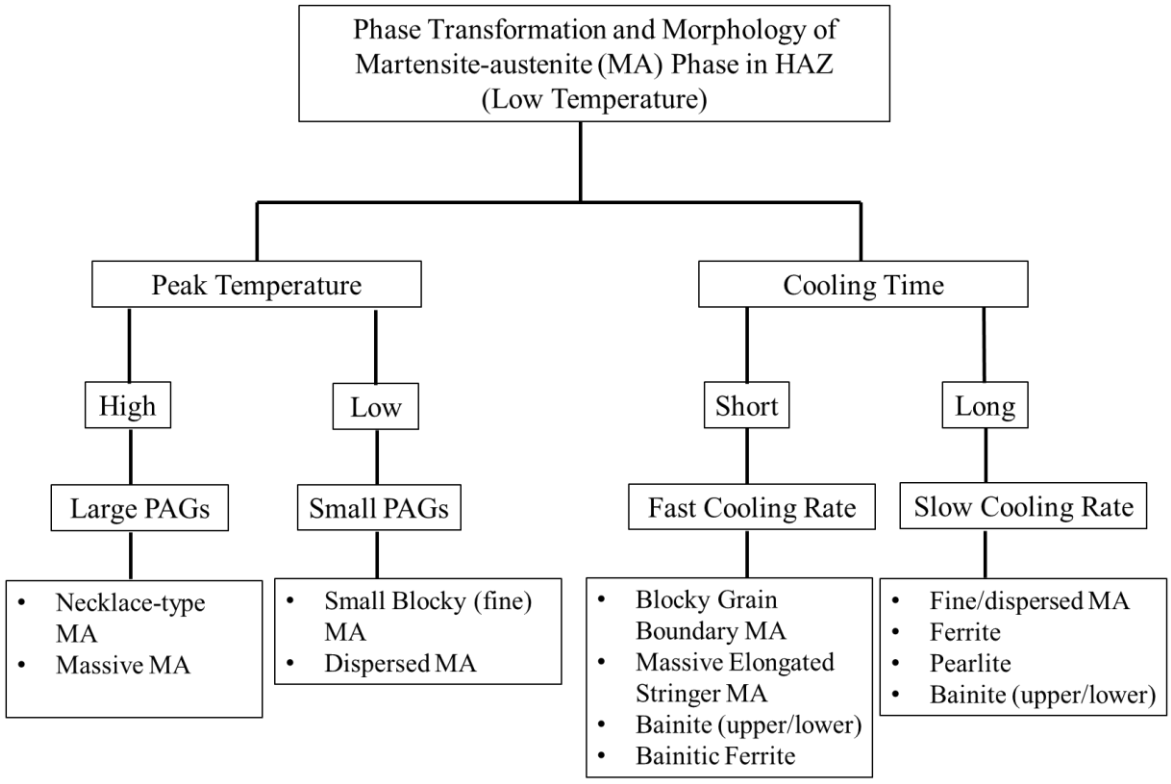

Figure 5.15 Effects of peak temperature and cooling time on phase transformation and morphology of MA in the CGHAZ.

5.9.1 Peak Temperature Effect

Figure 5.15 shows the effect of peak temperature on PAG size and MA morphlogy. Koistinen et al [115] reported that the fraction of MA constituents is proportional to the difference between the martensite start temperature (Ms) and the lowest temperature reached. Specifically, the fraction of MA is increased as the amount of undercooling is increased. Fisher et al. [70] developed a model that correlated the martensite fraction with PAG size and reported that the martensite fraction was positively proportional to the PAG size cubed in the early transformation stages. Li et al. [76] reported that the PAG size was relatively coarse in the CGHAZ for a high heat input (high peak temperature) weld. This means that a higher peak temperature is associated with a higher Ms and larger PAG size, which results in a higher volume fraction of massive MA constituents.

The above discussion supports the results obtained for the CW0-Ref. and CW40 samples, where the CW40 samples had smaller PAG sizes and lower MA fractions. The better MA morphology for the CW40 samples led to improved fracture toughness properties.

Yang et al. [71], Kim et al. [55], Li et al. [116] and Lambert et al. [66] have reported that coarse PAG with elongated MA particles promote cleavage fracture in the CGHAZ; specifically, elongated MA particles are due to the higher Ms and the coarse PAG is due to the high peak temperature. Finely dispersed MA is beneficial for toughness improvement. Davis et al. [114] and Lee et al. [110] reported that most of the elongated MA constituents formed at the coarse PAG boundaries and necklace-type MA islands formed a wide local brittle zone (LBZ). Both of these promote cleavage fracture and reduce the toughness of the CGHAZ. A detailed discussion of LBZ on toughness deterioration was presented in Section 2.4.

5.9.2 Cooling Rate Effect

Figure 5.15 summarizes the effect of cooling rate on phase transformation and MA morphology. The weld using the 33.9 mm/s cold wire feed rate has inferior toughness relative to the CW40 sample, but the CW80 sample has better toughness than the CW0-Ref. sample. This is atttributed to a wider LBZ in the CGHAZ of CW0-Ref. sample, due to more necklace-type MA islands at the coarse PAG boundaries than in the CGHAZ of CW80 sample (Figure 5.9). The poorer toughness for the CW80 samples is related to the unfavourable MA morphology. Blocky MA formed at the PAG boundaries and massive elongated stringer MA formed within the PAG (Figure 5.9-e). In addition, the largest size and the highest fraction of MA constituents were obtained for

the CW80 samples (Figure 5.14). The CW80 sample had the smallest PAG size, which is not in agreement with the hypothesis that coarser PAG promotes MA formation. The disagreement may be related to the high cooling rate in the CGHAZ of the CW80 sample. Huda et al. [108] reported that fast cooling rates (water cooled sample) resulted in a high MA fraction and blocky shape and confirmed that the carbon content was higher in the MA than in the adjacent ferrite matrix. Khan et al. [63] showed that the steel microstructure, at relatively fast cooling rates (6 ºC/s), was composed of martensite and bainite with little pearlite. Samples with slower cooling rates (4 to 1 ºC/s) contained extensive amounts of pearlite. Eroglu et al. [57] confirmed that slow cooling rate led to carbon-rich austenite transforming to polygonal ferrite and fine-grain pearlite. The various phases and morphology of MA are summaried in Figure 5.15.

The combined effects of peak temperature and cooling rate on the PAG size and MA morphology have been discussed. The formation of blocky and massive, elongated stringer MA consituents in the CGHAZ of the CW80 sample occur at the highest cooling rate. A CWFS of 16.9 mm/s resulted in a favorable cooling rate which promoted both refinement of the grain size and the formation of a favourable MA morphology in terms of fracture toughness behavior. The highest peak temperature occurred for the CGHAZ of the CW0-Ref. sample and was responsible for the inferior fracture toughness.

5.10 Welding Productivity

The aim of the CWTSAW process is to increase welding productivity of heavy gauge line pipe steels, while maintaining mechanical properties and without increasing heat input. It is generally accepted that increasing the heat input during welding will result in the deterioration of mechanical properties. Feeding a cold wire into the weld pool reduces the heat generated in the weldment while increasing welding productivity. Figure 5.16 shows the absorbed energy (-30 °C) and travel speed for the various welded steels. The CW0-Ref. sample was welded without any cold wire addition and had a low absorbed energy. When a cold wire feed speed of 16.9 mm/s and a travel speed of 21.2 mm/s are used, the absorbed energy of CW40 is increased which is indicative of fracture toughness improvement. However, inferior fracture toughness is obtained if the CWFS is increased to 33.9 mm/s (CW80), due to the relatively fast cooling rate. Qualitatively, the CWFS of 16.9 mm/s is suitable for the process. The possibility of increasing travel speed can improve productivity by reducing welding time. If the travel speed for the CW40 sample is increased 20%

(from 21.2 to 25.4 mm/s - CW40-TS60 sample) to improve productivity, the fracture toughness does not change markedly (Figure 5.16). However, if the travel speed is increased above 25.4 mm/s for the CW40 sample, a jamming phenomenon associated with the cold wire was generated at the weld since the arc of the trail electrode did not provide sufficient heat for cold wire fusion.

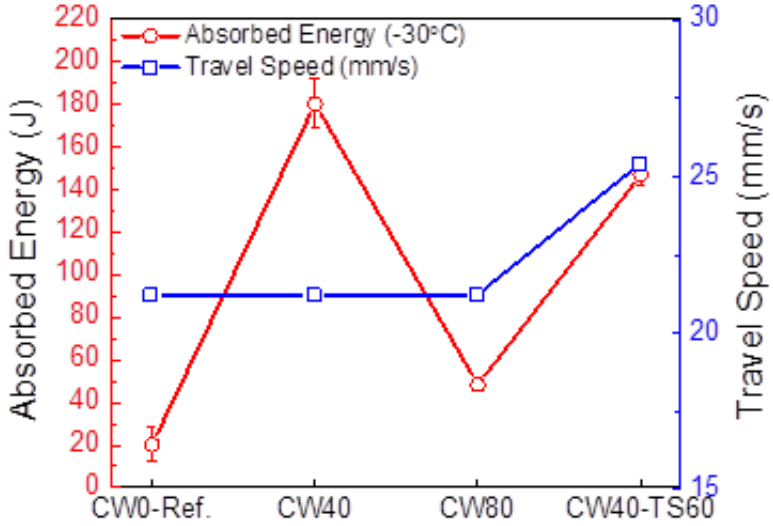

Figure 5.16 Absorbed energy during fracture testing at -30°C and travel speed for various CWTSAW samples.

5.11 Conclusions

The influence of CWTSAW on heavy gauge X70 line pipe steel (19.1 mm) in terms of microstructure characteristics and mechanical properties of the CGHAZ has been studied. The following conclusions can be made:

- The absorbed energy of the CGHAZ was improved up to 60% (from 85J to 137J) with CW40 sample.
- Grain refinement of PAG and α/B grains was achieved by cold wire addition.
- The CW40 samples had reduced MA fraction and finely dispersed MA, which provided a favorable morphology in terms of fracture toughness.
- Elongated and massive block MA constituents formed in the CW80 samples as a result of faster cooling rates and these were detrimental to the fracture toughness of the welded steel.
- The PAG size and MA morphology were significantly influenced by the peak temperature and cooling rate in the CGHAZ during welding.

- Welding productivity, while maintaining good fracture toughness, of 19.1 mm thick X70 line pipe steel was improved by 20% using a cold wire feed rate of 16.9 mm/s (40 in/min).

Chapter 6: Conclusions and Future Work

This Chapter contains conclusions drawn from Chapter 4 and 5. The following subsections list the main findings regarding the influence of cold wire addition on the weld geometry, microstructure and mechanical properties of the coarse grain heat-affected zone (CGHAZ) of welded heavy gauge X70 steel. Proposed future work is also presented.

6.1 Effect of CWTSAW parameters on weld geometry for heavy gauge X70 Steels

- The voltage of the lead and trail electrodes had a significant effect on the bead width, penetration profile and reinforcement shape. Higher voltage resulted in increased bead width and bead toe angle. Higher lead electrode voltage resulted in decreased CGHAZ area, aspect ratio and semi-penetration ratio.
- Cold wire feed speed had a secondary effect on the height of reinforcement area. An increase in cold wire feed speed resulted in a lower height of reinforcement area.
- Bevel design had a significant effect on the height of reinforcement area, reinforcement area, bead toe angle and CGHAZ area, but only a minor effect on the weld metal and CGHAZ micro-hardness.
- Cold wire feed speed had the most dominant effect on the weld metal and CGHAZ micro-hardness profiles, since the cold wire addition altered the local thermal cycle by absorbing heat from the molten pool.
- Increasing cold wire feed speed led to a lower hardness because of the faster cooling rate.
- A cold wire tandem submerged arc welding process, with a heat input for the lead electrode of 1.3 kJ/mm, a heat input for the trail electrode of 1.6 kJ/mm, a travel speed of 21.2 mm/s, a bevel angle of 90° and a bevel depth of 5 mm reduced the CGHAZ area, dilution, height of reinforcement area, and reinforcement area and increased bead width, penetration depth and bead toe angle.

6.2 Influence of CWTSAW on CGHAZ microstructure and properties

- The welds were fabricated using the optimized set of weld parameters showing uniform bead shape. The validity and feasibility of the parametric study was confirmed.

- The averaged absorbed energy of the CGHAZ was improved by 60% (from 85 J to 137 J) with a cold wire feed speed of 16.9 mm/s, a travel speed of 21.2 mm/s and a total heat input of 2.9 kJ/mm.
- The heat input was reduced by 10.3% (from 2.9 kJ/mm to 2.6 kJ/mm) when the cold wire was fed at 16.9 mm/s (40 in/min); this was accompanied by an improvement in the fracture toughness.
- A cold wire addition at 16.9 mm/s decreased the size of prior austenite grains (PAG) and ferrite/bainite grains, due to the decreased peak temperature and increased cooling rate in the HAZ.
- A cold wire feed speed of 16.9 mm/s minimized the size and fraction of martensite-austenite (MA) constituents and resulted in a dispersed distribution of MA constituents in the CGHAZ.
- The finer and lower fraction of MA constituents, due to the reduced heat input in the HAZ, contributed to fracture toughness improvement.
- A cold wire feed speed of 33.9 mm/s (80 in/min) promoted the presence of elongated and massive block MA constituents and resulted a concentrated distribution of MA constituents in the CGHAZ.
- The cooling rate in the HAZ from 800 °C to 500 °C was calculated based on the heat input analysis. The cooling rate increased as the cold wire feed speed increased in the HAZ.
- Elongated and massive block MA constituents in the HAZ, which formed because of the relatively fast cooling rate for welds with a cold wire feed speed of 33.9 mm/s, were detrimental to the fracture toughness.
- A lower actual heat input and faster cooling rate reduced the PAG size from 72.5 to 52.3 μm, for welds with a cold wire feed speed of 16.9 mm/s and a travel speed of 21.2 mm/s (50 in/min).
- A cold wire feed speed of 16.9 mm/s and a travel speed of 21.2 mm/s resulted in an intermediate cooling rate of 36.3 °C/s which promoted both a reduction of grain size and formation of finer MA and a small fraction of MA. Fracture toughness was improved.
- The PAG size and MA morphology were significantly influenced by the cooling rate and peak temperature in the CGHAZ during welding.

- Welding productivity, while maintaining good fracture toughness, of 19.1 mm thick X70 line-pipe steel was improved by 20% (from 21.2 mm/s to 25.4 mm/s) through feeding of a cold wire at 16.9 mm/s.

6.3 Future Work

- Full characterization of the CGHAZ microstructure for welds fabricated using a cold wire feed speed of 25.4 mm/s is necessary to develop a full understanding of the effect of cold wire feed speed (16.9 to 33.9 mm/s) on PAG size and MA morphology.
- Carbon density and the amount of segregated alloying elements in the MA constituents are needed to understand the MA constituent transformation under different cooling rates.
- A thermal simulation study of the HAZ is necessary quantitatively understand the local thermal cycle.
- Machine learning, using the geometrical and microstructural results obtained from heavy (19.1 mm) and intermediate gauge (13.4 mm) X70 line pipe steels for accurate prediction of the welding behavior of different gauge X70 line pipe steels, is worth pursuing.

References

[1] K. Weman, *Welding Processes Handbook (2nd Edition) - Knovel*. Woodhead Publishing, 2012.

[2] L. E. Collins, K. Dunnett, T. Hylton, and A. Ray, "Development of heavy gauge X70 helical line pipe," *Proc. Bienn. Int. Pipeline Conf. IPC*, vol. 3, pp. 1–9, 2018.

[3] A. O'Brien, "Triple-Arc Submerged Arc Welding," in *Welding Handbook, Volume 2 - Welding Processes, Part 1*, 9th Editio., A. O'Brien, Ed. American Welding Society (AWS), 2004, pp. 290–292.

[4] S. Moeinifar, A. H. Kokabi, H. R. Madaah Hosseini, C. J. Shang, G. Hui, and L. Z. Wei, "Influence of four wires tandem submerged arc welding process on heat affected zone properties in high strength pipeline steel," *Proc. 2010 Int. Conf. Mech. Ind. Manuf. Technol. MIMT 2010*, no. April 2015, pp. 85–89, 2010.

[5] S. M. Far, "Influence of thermal simulated and real tandem submerged arc welding process on the microstructure and mechanical properties of the coarse grained heat affected zone," *Appl. Mech. Mater.*, vol. 110–116, pp. 3191–3198, 2012.

[6] M. F. Mruczek and D. Parker, "Cold Wire Feed Submerged Arc Welding," Johnstown, PA, 2006.

[7] M. Mohammadijoo, L. Collins, H. Henein, and D. G. Ivey, "Evaluation of cold wire addition effect on heat input and productivity of tandem submerged arc welding for low-carbon microalloyed steels," *Int. J. Adv. Manuf. Technol.*, vol. 92, no. 1–4, pp. 817–829, 2017.

[8] M. Mohammadijoo, S. Kenny, L. Collins, H. Henein, and D. G. Ivey, "Influence of cold-wire tandem submerged arc welding parameters on weld geometry and micro-hardness of microalloyed pipeline steels," *Int. J. Adv. Manuf. Technol.*, pp. 2249–2263, 2017.

[9] M. Ramakrishnan and V. Muthupandi, "Application of submerged arc welding technology with cold wire addition for drum shell long seam butt welds of pressure vessel components," *Int. J. Adv. Manuf. Technol.*, vol. 65, no. 5–8, pp. 945–956, 2013.

[10] S. K. J. Ramakrishnan Mannarsamy*, S.K.Shrivastava*, PiyushThakor*, Gautam Chauhan* and and R. korada Korada*, "Establishment of cold wire addition technology in multiwire submerged arc welding for line pipe manufacturing to improve the weldment quality," *ASME 2015 India Oil Gas Pipeline Conf.*, pp. 1–11, 2015.

[11] M. Ramakrishnan, K. Padmanaban, and V. Muthupandi, "Studies on fracture toughness of cold wire addition in narrow groove submerged arc welding process," *Int. J. Adv. Manuf. Technol.*, vol. 68, no. 1–4, pp. 293–316, 2013.

[12] C. Yang, "R&D and applications of V-N microallloyed steels in China," in *7th International Conference on High Strength Low Alloy Steels, HSLA Steels*, 2015, vol. 2, p. p 917-930.

[13] X. Huo, J. Xia, L. Li, Z. Peng, S. Chen, and C. T. Peng, “A review of research and development on titanium microalloyed high strength steels,” *Mater. Res. Express*, vol. 5, no. 6, 2018.

[14] J. C. Villalobos, A. Del-Pozo, B. Campillo, J. Mayen, and S. Serna, “Microalloyed steels through history until 2018: Review of chemical composition, processing and hydrogen service,” *Metals (Basel).*, vol. 8, no. 5, 2018.

[15] T. N. Baker, “Microalloyed steels,” *Ironmak. Steelmak.*, vol. 43, no. 4, pp. 264–307, 2016.

[16] M. Mohammadijoo, L. Collins, H. Henein, and D. G. Ivey, “CANADIAN HSLA STEEL PIPELINES : HISTORY AND TECHNOLOGY,” *Res. Artic. Mater.*, no. University of Alberta, p. 8, 2018.

[17] T. Ogawa, K. Sato, H. Dannoshita, K. Maruoka, and K. Ushioda, “Role of Nb on microstructural evolution during intercritical annealing in low-carbon steels,” *ISIJ Int.*, vol. 56, no. 12, pp. 2290–2297, 2016.

[18] A. Jenney, Cynthia L.; O’Brien, “Weldability of Commercial Alloys,” in *Welding Handbook, Volume1 - Welding Science and Technology*, American Welding Society (AWS), 2001, pp. 140–142.

[19] C. L. Davis and J. E. King, “Cleavage initiation in the intercritically reheated coarse-grained heat-affected zone: Part I. Fractographic evidence,” *Metall. Mater. Trans. A*, vol. 25, no. 3, pp. 563–573, 1994.

[20] B. De Meester, “The weldability of modern structural TMCP steels,” *ISIJ Int.*, vol. 37, no. 6, pp. 537–551, 1997.

[21] S. Endo and N. Nakata, “Development of Thermo-Mechanical Control Process (TMCP) and high performance steel in JFE Steel,” *JFE Tech. Rep.*, vol. 20, no. 20, pp. 1–7, 2015.

[22] S. Vervynckt, K. Verbeken, B. Lopez, and J. J. Jonas, “Modern HSLA steels and role of non-recrystallisation temperature,” *Int. Mater. Rev.*, vol. 57, no. 4, pp. 187–207, 2012.

[23] S. Kyriakides and E. Corona, “Pipe and Tube Manufracturing Processes,” in *Mechanics of Offshore Pipelines*, 2007, pp. 59–88.

[24] A. O’Brien, “6.2.1 Advantages and Limitations,” in *Welding Handbook, Volume 2- Welding Processes, Part 1*, 9th Editio., American Welding Society (AWS), 2004, pp. 257–258.

[25] A. Jenney, Cynthia L. O’Brien, “1.2.1.2 Submerged Arc Welding,” in *Welding Handbook, Volume 1*, 9th Editio., American Welding Society (AWS), 2001, pp. 7–8.

[26] A. O’Brien, “6.7.2.5 Tandem Arc Submerged Arc Welding,” in *Welding Handbook, Volume 2 - Welding Processes, Part 1*, 9th Editio., American Welding Society (AWS), 2004, p. 290.

[27] Suryana, A. Pramono, I. Muda, and A. Setiawan, “The Influence of Heat Input to Mechanical Properties and Microstructures of API 5L-X65 Steel Using Submerged Arc Welding Process,” *MATEC Web Conf.*, vol. 269, p. 01009, 2019.

[28] C. Yan, L. Wu, W. Wu, Y. Yuan, and X. Yang, “Prediction of HAZ width in submerged arc welding of mild steel,” *IOP Conf. Ser. Earth Environ. Sci.*, vol. 252, no. 2, 2019.

[29] R. C. Júnior *et al.*, “Influence of Heat Input and Cold Wire Feeding Rate on Pitting Corrosion Resistance of Submerged Arc Welding Duplex Stainless Steel Welds,” *J. Mater. Eng. Perform.*, vol. 28, no. 4, pp. 1969–1976, 2019.

[30] M. Mohammadijoo, L. Collins, R. Lazor, H. Henein, and D. G. Ivey, “Influence of Cold-Wire Submerged Arc Welding on the Toughness of Microalloyed Steel,” *Weld. J.*, vol. 97, no. December, pp. 338s-352s, 2018.

[31] M. Mohammadijoo, S. Kenny, L. Collins, H. Henein, and D. G. Ivey, “Characterization of HAZ of API X70 Microalloyed Steel Welded by Cold-Wire Tandem Submerged Arc Welding,” *Metall. Mater. Trans. A Phys. Metall. Mater. Sci.*, vol. 48, no. 5, pp. 2247–2259, 2017.

[32] M. Mohammadijoo, J. Valloton, L. Collins, H. Henein, and D. G. Ivey, “Characterization of martensite-austenite constituents and micro-hardness in intercritical reheated and coarse-grained heat affected zones of API X70 HSLA steel,” *Mater. Charact.*, vol. 142, no. May, pp. 321–331, 2018.

[33] K. Easterling, “The heat-affected zone,” in *Introduction to the Physical Metallurgy of Welding*, 2nd ed., Butterworth-Heinemann, 1992, pp. 126–190.

[34] A. O’Brien, “Welding Handbook, Volume 2 - Welding Processes, Part 1 - 6.5 Process variables,” 9th Editio., American Welding Society (AWS), 2004, pp. 278–282.

[35] K. Weman, “4.3.1 Electromagnetic Forces and the Plasma Jet,” in *Welding processes Handbook*, Woodhead Publishing, 2012, p. 37.

[36] S. E. Hughes, “Chapter 7 Fracture Modes and Welding Defects,” in *Quick Guide to Welding and Weld Inspection*, Woodhead Publishing, 2009, p. 101.

[37] K. Weman, “10.4.2 Welding Parameters and Weld Quality,” in *Welding Processes Handbook (2nd Edition)*, 2nd ed., Woodhead Publishing, 2012, pp. 113–114.

[38] J. T. Pepin, “Effects of Submerged Arc Weld (SAW) Parameters on Bead Geometry and Notch-Toughness for X70 and X80 Linepipe Steels,” University of Alberta, 2009.

[39] K. Fisher, “Technology Increases SAW Deposition Rates,” *Weld. Des. Fabr.*, vol. 75, no. 3, pp. 28–32, 2002.

[40] D. V. Kiran, D. W. Cho, W. H. Song, and S. J. Na, “Arc interaction and molten pool behavior in the three wire submerged arc welding process,” *Int. J. Heat Mass Transf.*, vol. 87, pp. 327–340, 2015.

[41] R. P. Singh, R. K. Garg, and D. K. Shukla, “Mathematical modeling of effect of polarity on weld bead geometry in submerged arc welding,” *J. Manuf. Process.*, vol. 21, pp. 14–22, 2016.

[42] G. Taguchi, *Taguchi on Robust Technology Development: Bringing Quality Engineering Upstream*. ASME Press, 1993.

[43] R. K. Roy, “Primer on the Taguchi Method (2nd Edition) - 6. Analysis of Variance (ANOVA),” in *Primer on the Taguchi Method*, 2nd ed., R. K. Roy, Ed. Society of Manufacturing Engineers (SME), 2010.

[44] Y. S. Tarng and W. H. Yang, “Application of the Taguchi method to the optimization of the submerged arc welding process,” *Mater. Manuf. Process.*, vol. 13, no. 3, pp. 455–467, 1998.

[45] H. Shahverdi Shahraki and H. Mozafari, “Modeling and Optimizing of Submerged Arc Welding Process by Taguchi Design of Experiments in Presence of Magnesium Oxide Nano-Particles,” *Appl. Mech. Mater.*, vol. 763, pp. 52–57, 2015.

[46] A. Sarkar, J. Roy, A. Majumder, and S. C. Saha, “Optimization of Welding Parameters of Submerged Arc Welding Using Analytic Hierarchy Process (AHP) Based on Taguchi Technique,” *J. Inst. Eng. Ser. C*, vol. 95, no. 2, pp. 159–168, 2014.

[47] P. Besharati Givi, Mohammad Kazem; Asadi, “13.3.1 Taguchi Method,” in *Advances in Friction-Stir Welding and Processing*, Elsevier, 2014, p. 564.

[48] Q. Xin, “3.1.5 The Taguchi Method,” in *Diesel Engine system Design*, Woodhead Publishing, 2011, pp. 215–216.

[49] M. H. Kakaei Lafdani, E. Ghadiri Zahrani, and A. M. Galloway, “Optimization study of weld geometry in the tandem submerged arc welding process,” *Proc. Inst. Mech. Eng. Part B J. Eng. Manuf.*, vol. 229, no. 6, pp. 1068–1077, 2015.

[50] P. G. Mathews, “Design of Experiments with MINITAB,” in *Linear Regression*, P. G. Mathews, Ed. American Society for Quality (ASQ), 2005, pp. 273–346.

[51] K. Gowthaman, J. Saiganesh, and C. S. Rajamanikam, “Determination of submerged arc welding process parameters using Taguchi method and regression analysis,” *2013 Int. Conf. Energy Effic. Technol. Sustain. ICEETS 2013*, pp. 842–847, 2013.

[52] M. Sailender, R. Suresh, G. Chandramohan Reddy, and S. Venkatesh, “Prediction and comparison of the dilution and heat affected zone in submerged arc welding (SAW) of low carbon alloy steel joints,” *Meas. J. Int. Meas. Confed.*, vol. 150, p. 107084, 2020.

[53] R. L. Mason, R. F. Gunst, and J. L. Hess, “13 Analysis of Nested Designs and Designs for Process Improvement,” in *Statistical Design and Analysis of Experiments - With Applications to Engineering and Science*, 2nd Editio., vol. 1, 2003, pp. 423–458.

[54] J. D. Verhoeven, “5.3 The Notched Impact Test,” in *Steel Metallurgy for the Non-Metallurgist*, ASM International, 2007, pp. 47–48.

[55] B. C. Kim, S. Lee, N. J. Kim, and D. Y. Lee, “Microstructure and local brittle zone phenomena in high-strength low-alloy steel welds,” *Metall. Trans. A*, vol. 22, no. 1, pp. 139–149, 1991.

[56] S. Grellmann, Wolfgang Seidler, “4.4.2 Charpy Impact Test and Charpy Notched Impact Test,” in *Polymer Testing*, 2nd ed., Hanser Publishers, 2013, p. 150.

[57] M. Eroglu and M. Aksoy, “Effect of initial grain size on microstructure and toughness of intercritical heat-affected zone of a low carbon steel,” *Mater. Sci. Eng. A*, vol. 286, no. 2, pp. 289–297, 2000.

[58] G. Roberts, G. Krauss, and R. Kennedy, “Principles of Tool Steel Heat Treatment,” in *Tool Steels*, R. Roberts, George; Krauss, George; Kennedy, Ed. ASM Internationa, 1998, pp. 68–103.

[59] V. Javaheri, N. Khodaie, T. T. Nyo, and D. Porter, “Induction hardening of a 0.40% c novel microalloyed steel: Effects of heating rate on the prior austenite grain size,” *Mater. Sci. Forum*, vol. 941 MSF, pp. 64–70, 2018.

[60] H. F. Lan, L. X. Du, Q. Li, C. L. Qiu, J. P. Li, and R. D. K. Misra, “Improvement of strength-toughness combination in austempered low carbon bainitic steel: The key role of refining prior austenite grain size,” *J. Alloys Compd.*, vol. 710, pp. 702–710, 2017.

[61] X. Li, C. Shang, X. Ma, and S. V. Subramanian, “Study on the toughness of X100 pipeline steel heat affected zone,” *Energy Mater. 2014, Conf. Proc.*, pp. 597–604, 2014.

[62] X. Li, X. Ma, S. V. Subramanian, C. Shang, and R. D. K. Misra, “Influence of prior austenite grain size on martensite-austenite constituent and toughness in the heat affected zone of 700MPa high strength linepipe steel,” *Mater. Sci. Eng. A*, vol. 616, pp. 141–147, 2014.

[63] A. R. Khan, S. Yu, H. Wang, and Y. Jiang, “Effect of cooling rate on microstructure and mechanical properties in the CGHAZ of electroslag welded pearlitic rail steel,” *Metals (Basel).*, vol. 9, no. 7, 2019.

[64] S. Moeinifar, A. H. Kokabi, and H. R. M. Hosseini, “Effect of tandem submerged arc welding process and parameters of Gleeble simulator thermal cycles on properties of the intercritically reheated heat affected zone,” *Mater. Des.*, vol. 32, no. 2, pp. 869–876, 2011.

[65] S. Moeinifar, A. H. Kokabi, and H. R. M. Hosseini, “Role of tandem submerged arc welding thermal cycles on properties of the heat affected zone in X80 microalloyed pipe line steel,” *J. Mater. Process. Technol.*, vol. 211, no. 3, pp. 368–375, 2011.

[66] A. Lambert-Perlade, A. F. Gourgues, J. Besson, T. Sturel, and A. Pineau, “Mechanisms and modeling of cleavage fracture in simulated heat-affected zone microstructures of a high-strength low alloy steel,” *Metall. Mater. Trans. A Phys. Metall. Mater. Sci.*, vol. 35, no. 13, pp. 1039–1053, 2004.

[67] A. Lambert, J. Drillet, A. F. Gourgues, T. Sturel, and A. Pineau, “Microstructure of martensite-austenite constituents in heat affected zones of high strength low alloy steel welds in relation to toughness properties,” *Sci. Technol. Weld. Join.*, vol. 5, no. 3, pp. 168–173, 2000.

[68] X. Li, X. Ma, S. V. Subramanian, and C. Shang, “EBSD characterization of secondary microcracks in the heat affected zone of a X100 pipeline steel weld joint,” *Int. J. Fract.*, vol. 193, no. 2, pp. 131–139, 2015.

[69] A. I. Handbook, *26.2 Martensite and Austenite*. ASM Handbook, 1991.

[70] J. C. Fisher, J. H. Hollomon, and D. Turnbull, “Kinetics of the Aostenite-t Martensite TransforlDation,” *Met. Trans.*, vol. 185, pp. 691–700.

[71] H. S. Yang and H. K. D. H. Bhadeshia, “Austenite grain size and the martensite-start temperature,” *Scr. Mater.*, vol. 60, no. 7, pp. 493–495, 2009.

[72] J. Zhang, C. S. Li, B. Z. Li, Z. X. Li, and Q. W. Wang, “Effect of Final Cooling Temperature on Microstructure and Mechanical Properties of a Cr-Ni-Mo-V Bainite Steel,” *J. Mater. Eng. Perform.*, vol. 27, no. 9, pp. 4749–4759, 2018.

[73] M. Shome, O. P. Gupta, and O. N. Mohanty, “Effect of simulated thermal cycles on the microstructure of the heat-affected zone in HSLA-80 and HSLA-100 steel plates,” *Metall. Mater. Trans. A Phys. Metall. Mater. Sci.*, vol. 35, no. 13, pp. 985–996, 2004.

[74] X. Li *et al.*, “Elemental distribution in the martensite–austenite constituent in intercritically reheated coarse-grained heat-affected zone of a high-strength pipeline steel,” *Scr. Mater.*, vol. 139, pp. 67–70, 2017.

[75] Z. Zhu, L. Kuzmikova, H. Li, and F. Barbaro, “Effect of inter-critically reheating temperature on microstructure and properties of simulated inter-critically reheated coarse grained heat affected zone in X70 steel,” *Mater. Sci. Eng. A*, vol. 605, pp. 8–13, 2014.

[76] C. Li, Y. Wang, and Y. Chen, “Influence of peak temperature during in-service welding of API X70 pipeline steels on microstructure and fracture energy of the reheated coarse grain heat-affected zones,” *J. Mater. Sci.*, vol. 46, no. 19, pp. 6424–6431, 2011.

[77] C. Li, Y. Wang, T. Han, B. Han, and L. Li, “Microstructure and toughness of coarse grain heat-affected zone of domestic X70 pipeline steel during in-service welding,” *J. Mater. Sci.*, vol. 46, no. 3, pp. 727–733, 2011.

[78] American Welding Society (AWS) D1 Structural Welding Committee, *Guide for Strengthening and Repairing Existing Structures (1st Edition): (AWS D1.7/D1.7M:2010) - 4.4.2.2 Manganese*, 1st ed. AWS, 2009.

[79] ASTM International, “ASTM E3-11 Stardard Guide for Preparation of metallographic specimens,” *ASTM Stand.*, vol. 11, no. Reapproved 2017, pp. 1–17, 2017.

[80] F. S. Lepera, “Improved Etching Technique for the Determination of Percent Mar- tensite in High-Strength Dual-Phase Steels,” *Metallography*, no. Elsevier North Holland, Inc., 1979, pp. 263–268, 1979.

[81] ASTM, “ASTM E112-13: Standard test methods for determining average grain size,” *ASTM Int.*, pp. 1–28, 2013.

[82] J. M. Reichert, W. J. Poole, M. Militzer, and L. Collins, “A NEW APPROACH USING EBSD TO QUANTITATIVELY DISTINGUISH COMPLEX TRANSFORMATION PRODUCTS ALONG THE HAZ IN X80 LINEPIPE STEEL,” *Ipc 2014*, pp. 1–7, 2014.

[83] ASTM E384 - 17, “Standard Test Method for Microindentation Hardness of Materials,” *ASTM Int.*, pp. 1–40, 2017.

[84] ASTM E 23-12c, “Standard Test Methods for Notched Bar Impact Testing of Metallic Materials,” *Standards*, vol. i, pp. 1–25, 2013.

[85] S. K. Sharma and S. Maheshwari, “A review on welding of high strength oil and gas pipeline steels,” *J. Nat. Gas Sci. Eng.*, vol. 38, pp. 203–217, 2017.

[86] U. Reisgen, U. Dilthey, and I. Aretov, “SAW cold wire technology - Economic alternative for joining hot crack sensitive nickel-base alloys,” *Hot Crack. Phenom. Welds II*, pp. 215–237, 2008.

[87] N. Murugan, R. S. Parmar, and S. K. Sud, “Effect of submerged arc process variables on dilution and bead geometry in single wire surfacing,” *J. Mater. Process. Tech.*, vol. 37, no. 1–4, pp. 767–780, 1993.

[88] J. Pepin, C. Penniston, H. Henein, D. G. Ivey, L. Collins, and D. Boyd, “Using semipenetration ratio to characterize effects of waveform variables on bead profile and heat affected zone with single electrode submerged arc welding,” *Can. Metall. Q.*, vol. 51, no. 3, pp. 284–293, 2012.

[89] R. D. Thomas, “Weld Overlays, Welding, Brazing, and Soldering,” *Met. Handbook, Am. Soc. Met.*, vol. 6, pp. 804–819, 1983.

[90] M. Mohammadijoo, “Development of a Welding Process to Improve Welded Microalloyed Steel Characteristics,” p. 33, 2017.

[91] J. . Lancaster, “8.3 Transformation and Microstructure of Steel,” in *Metallurgy of Welding (6th Edition)*, 6th ed., Woodhead Publishing, 1999, pp. 234–238.

[92] P. Yan and H. K. D. H. Bhadeshia, “Mechanism and kinetics of solid-state transformation in high-temperature processed linepipe steel,” *Metall. Mater. Trans. A Phys. Metall. Mater. Sci.*, vol. 44, no. 12, pp. 5468–5477, 2013.

[93] X. Li, Y. Fan, X. Ma, S. V. Subramanian, and C. Shang, “Influence of Martensite-Austenite constituents formed at different intercritical temperatures on toughness,” *Mater. Des.*, vol. 67, pp. 457–463, 2015.

[94] A. O’Brien, “6.5 Process Variables,” in *Welding Handbook, Volume 2 - Welding Processes, Part 1*, 9th Editio., American Welding Society (AWS), 2004, pp. 278–282.

[95] J. F. Lancaster, “Metallurgical Effects of the Weld Thermal Cycle,” in *Metallurgy of Welding*, Woodhead Publishing, 1999, pp. 169–208.

[96] D. P. & M. K. z. Sun, “High Productivity Cladding with Non-Consumable Electrode Arc Processes,” in *6’th International Trendsin Welding Research Conference Proceedings*, 2020, no. April 2002, pp. 15–19.

[97] J. Chen, C. Schwenk, C. S. Wu, and M. Rethmeier, “Predicting the influence of groove angle on heat transfer and fluid flow for new gas metal arc welding processes,” *Int. J. Heat Mass Transf.*, vol. 55, no. 1–3, pp. 102–111, 2012.

[98] Y. Huang, H. Yu, J. Zhang, and C. Ren, “Study on arc physical characteristics of GPCA-TIG welding under different angles of V groove,” *Eng. Res. Express*, vol. 1, no. 1, p. 015032, 2019.

[99] B. Ribic, S. Tsukamoto, R. Rai, and T. DebRoy, “Role of surface-active elements during keyhole-mode laser welding,” *J. Phys. D. Appl. Phys.*, vol. 44, no. 48, 2011.

[100] P. Rajesh Kannan, V. Muthupandi, and K. Devakumaran, “On the effect of temperature coefficient of surface tension on shape and geometry of weld beads in hot wire gas tungsten arc welding process,” *Mater. Today Proc.*, vol. 5, no. 2, pp. 7845–7852, 2018.

[101] X. Li, Y. Fan, X. Ma, S. V. Subramanian, and C. Shang, “Influence of Martensite-Austenite constituents formed at different intercritical temperatures on toughness,” *Mater. Des.*, vol. 67, pp. 457–463, 2015.

[102] H. Somekawa and T. Mukai, “Fracture toughness in an extruded ZK60 magnesium alloy,” *Mater. Trans.*, vol. 47, no. 4, pp. 995–998, 2006.

[103] B. zhou Li, C. sheng Li, X. Jin, and J. Zhang, “Effect of M–A constituents formed in thermo-mechanical controlled process on toughness of 20CrNi2MoV steel,” *J. Iron Steel Res. Int.*, vol. 26, no. 12, pp. 1340–1349, 2019.

[104] “Eurocode 3: Design of steel structures - Part 1-2: General Rules - Structral fire design,” 2011.

[105] V. Narang, “Heat transfer analysis in steel structures,” WORCESTER POLYTECHNIC INSTITUTE, 2005.

[106] K. Poorhaydari, B. M. Patchett, and D. G. Ivey, “Estimation of Cooling Rate in the Welding of Plates with Intermediate Thcikness,” *Weld. J.*, no. October, pp. 149–155, 2005.

[107] Z. Zhu, L. Kuzmikova, H. Li, and F. Barbaro, “The effect of chemical composition on microstructure and properties of intercritically reheated coarse-grained heat-affected zone in X70 steels,” *Metall. Mater. Trans. B Process Metall. Mater. Process. Sci.*, vol. 45, no. 1, pp. 229–235, 2014.

[108] N. Huda, A. R. H. Midawi, J. Gianetto, R. Lazor, and A. P. Gerlich, “Influence of martensite-austenite (MA) on impact toughness of X80 line pipe steels,” *Mater. Sci. Eng. A*, vol. 662, pp. 481–491, 2016.

[109] X. Li, C. Shang, C. Han, Y. Fan, and J. Sun, “Influence of necklace-type M-A constituent on impact toughness and fracture mechanism in the heat affected zone of x100 pipeline steel,” *Jinshu Xuebao/Acta Metall. Sin.*, vol. 52, no. 9, pp. 1025–1035, 2016.

[110] S. Lee, B. C. Kim, and D. Kwon, “Fracture toughness analysis of heat-affected zones in high-strength low-alloy steel welds,” *Metall. Trans. A*, vol. 24, no. 5, pp. 1133–1141, 1993.

[111] L. Yu, H. H. Wang, T. P. Hou, X. L. Wang, X. L. Wan, and K. M. Wu, “Characteristic of martensite–austenite constituents in coarse grained heat affected zone of hsla steel with varying al contents,” *Sci. Technol. Weld. Join.*, vol. 19, no. 8, pp. 708–714, 2014.

[112] L. Yu, H. H. Wang, X. L. Wang, G. Huang, T. P. Hou, and K. M. Wu, “Improvement of impact toughness of simulated heat affected zone by addition of aluminium,” *Mater. Sci. Technol. (United Kingdom)*, vol. 30, no. 15, pp. 1951–1958, 2014.

[113] J.L. Dossett and H. E. Boyer, “Practical Heat Treating,” in *Practical heat treating*, 2nd Editio., ASM International, 2006, p. 296.

[114] C. L. Davis and J. E. King, “Effect of cooling rate on intercritically reheated microstructure and toughness in high strength low alloy steel,” *Mater. Sci. Technol.*, vol. 9, no. 1, pp. 8–15, 1993.

[115] D. P. Koistinen and R. E. Marburger, “A general equation prescribing the extent of the austenite-martensite transformation in pure iron-carbon alloys and plain carbon steels,” *Acta Metall.*, vol. 7, no. 1, pp. 59–60, 1959.

[116] Y. Li and T. N. Baker, “Effect of morphology of martensite-austenite phase on fracture of weld heat affected zone in vanadium and niobium microalloyed steels,” *Mater. Sci. Technol.*, vol. 26, no. 9, pp. 1029–1040, 2010.

{Bibliography

Appendix

This Appendix includes the quantities of ANOVA for weld geometric measurements and micro-hardness of the CGHAZ and WM. The average of signal-to-noise (S/N) ratio values for each weld geometric results and weld parameters are presented. Multiple linear regression (MLR) results for SPR, AR and dilution and three order multiple regression analysis (TOMRA) for HRA, RA, CGHAZ area, SPR, and CGHAZ and WM micro-hardness are presented. Additionally, the calculated effective contribution using sum of squares (SS) for weld geometric values are presented.

A.1 Analysis of Variance (ANOVA)

Table A.1 ANOVA table for weld geometric values, dilution, the WM and CGHAZ micro-hardness.

Characteristic		CWFS	HIL	HIT	VL	VT	TS	BD	R^2
BW	DF	3	1	1	1	1	1	1	82.2%
	SS	0.74	0.48	0.23	5.28	0.87	3.84	0.11	
	F	0.59	1.16	0.54	12.64	2.08	9.17	0.26	
	P	0.65	0.32	0.49	0.012	0.20	0.02	0.63	
HRA	DF	3	1	1	1	1	1	1	97.8%
	SS	0.63	0.01	0.64	0.73	1.51	0.92	4.28	
	F	6.40	0.16	19.43	22.19	46.02	28.14	130.72	
	P	0.03	0.70	0.01	0.00	0.00	0.00	0.00	
BTA	DF	3	1	1	1	1	1	1	89.0%
	SS	50.03	8.56	180.71	112.79	108.68	82.23	367.83	
	F	0.89	0.46	9.64	6.01	5.79	4.38	19.61	
	P	0.50	0.52	0.02	0.05	0.05	0.08	0.00	
CGHAZA	DF	3	1	1	1	1	1	1	93.1%
	SS	4.90	10.76	8.34	8.37	4.01	1.57	50.19	
	F	1.50	9.87	7.65	7.68	3.68	1.44	46.04	
	P	0.31	0.02	0.03	0.03	0.10	0.28	0.001	

Table A.1 (continued)

Characteristic		CWFS	HIL	HIT	VL	VT	TS	BD	R^2
AR	DF	3	1	1	1	1	1	1	89.2%
	SS	0.01	0.03	0.03	0.06	0.01	0.05	0.01	
	F	0.68	6.54	7.58	14.86	3.71	11.32	3.46	
	P	0.59	0.04	0.03	0.01	0.10	0.02	0.11	
SPR	DF	3	1	1	1	1	1	1	84.4%
	SS	0.01	0.012	0.005	0.015	0.001	0.04	0.001	
	F	1.27	4.68	1.93	5.76	0.38	15.54	0.42	
	P	0.37	0.07	0.21	0.05	0.56	0.01	0.54	
Dilution	DF	3	1	1	1	1	1	1	81.9%
	SS	0.0002	0.002	0.0001	0.0001	0.0013	0.0002	0	
	F	0.4	12.94	0.95	0.69	9.64	1.76	0	
	P	0.76	0.01	0.37	0.44	0.02	0.23	1.00	
CGHAZ Hardness	DF	3	1	1	1	1	1	1	68.1%
	SS	115.57	19.78	2.25	10.35	0.50	27.28	0.66	
	F	2.80	1.44	0.16	0.75	0.04	1.98	0.05	
	P	0.13	0.28	0.70	0.42	0.86	0.21	0.83	
WM Hardness	DF	3	1	1	1	1	1	1	75.6%
	SS	38.64	1.28	38.28	0.02	11.46	11.94	0.52	
	F	2.37	0.24	7.03	0.00	2.10	2.19	0.10	
	P	0.17	0.65	0.04	0.95	0.20	0.19	0.77	

A.2 Signal to Noise (S/N) Ratio

Table A.2 Average signal-to-noise (S/N) ratio values for seven welding parameters of CWTSAW

Symbol	Parameters	Level	BW	HRA	BTA	RA
A	CWFS	1	23.0 (0.3)	-12.6 (0.6)	**42.1 (0.1)**	-32.6 (0.8)
		2	22.8 (0.4)	-13.3 (0.8)	41.7 (0.4)	-33.3 (0.8)
		3	**23.1 (0.2)**	**-12.2 (0.9)**	41.9 (0.3)	**-32.5 (0.9)**
		4	22.8 (0.4)	-12.9 (0.9)	41.9 (0.40)	-32.6 (0.9)
B	HIL	1	**23.0 (0.2)**	**-12.5 (0.5)**	**42.0 (0.2)**	-32.9 (0.4)
		2	22.8 (0.2)	-12.7 (0.7)	41.9 (0.2)	**-32.6 (0.7)**
C	HIT	1	**23.0 (0.2)**	**-12.3 (0.5)**	**42.2 (0.2)**	**-32.3 (0.6)**
		2	22.8 (0.3)	-13.1 (0.6)	41.7 (0.2)	-33.2 (0.5)
D	VL	1	22.6 (0.2)	-12.3 (0.5)	41.7 (0.2)	-32.9 (0.6)
		2	**23.3 (0.2)**	**-12.2 (0.5)**	**42.1 (0.2)**	**-32.6 (0.6)**
E	VT	1	22.8 (0.2)	-13.3 (0.6)	41.7 (0.2)	-33.3 (0.6)
		2	**23.1 (0.2)**	**-12.2 (0.4)**	**42.1 (0.2)**	**-32.2 (0.5)**
F	TS	1	**23.2 (0.2)**	**-12.2 (0.6)**	**42.1 (0.2)**	**-32.5 (0.7)**
		2	22.6 (0.2)	-13.2 (0.5)	41.8 (0.2)	-33.0 (0.5)
G	BD	1	22.9 (0.2)	-13.8 (0.3)	41.6 (0.2)	-34.0 (0.2)
		2	**23.0 (0.2)**	**-11.7 (0.5)**	**42.2 (0.2)**	**-31.5 (0.5)**

*Higher S/N ratio values are indicated in bold and values in bracket are indicated as one standard deviation.

Table A.2 (Continued)

Symbol	Parameters	Level	SPR	CGHAZA	Dilution	AR
A	CWFS	1	-1.0 (0.3)	**-27.6 (0.3)**	3.6 (0.2)	-1.0 (0.5)
		2	**-0.7 (0.6)**	-28.0 (0.7)	**3.7 (0.1)**	**-0.6 (1.0)**
		3	-1.3 (0.2)	-28.1 (0.4)	3.6 (0.1)	-0.9 (0.2)
		4	-1.2 (0.5)	-27.8 (0.5)	3.5 (0.1)	-0.7 (0.4)
B	HIL	1	-1.3 (0.2)	**-27.6 (0.3)**	**3.7 (0.1)**	-1.2 (0.4)
		2	**-0.8 (0.3)**	-28.2 (0.3)	3.5 (0.1)	**-0.4 (0.4)**
C	HIT	1	-1.2 (0.1)	**-27.6 (0.3)**	**3.6 (0.1**)	-1.2 (0.3)
		2	**-0.9 (0.4)**	-28.2 (0.3)	3.5 (0.1)	**-0.4 (0.4)**
D	VL	1	**-0.8 (0.3)**	-28.1 (0.3)	**3.6 (**0.1)	**-0.2 (0.4)**
		2	-1.3 (0.2)	**-27.7 (0.3)**	3.5 (0.1)	-1.4 (0.3)
E	VT	1	**-1.0 (0.3)**	-28.1 (0.3)	**3.7 (0.1)**	-0.5 (0.4)
		2	-1.1 (0.2)	**-27.7 (0.3)**	3.5 (0.1)	**-1.1 (0.3)**
F	TS	1	-1.5 (0.2)	-28.0 (0.3)	**3.7 (0.1)**	-1.3 (0.3)
		2	**-0.6 (0.2)**	**-27.9 (0.3)**	3.5 (0.1)	**-0.3 (0.4)**
G	BD	1	-1.1 (0.2)	**-27.3 (0.2)**	3.6 (0.1)	-1.1 (0.4)
		2	**-1.0 (0.4)**	-28.5 (0.2)	**3.7 (0.1)**	**-0.5 (0.4)**

*Higher S/N ratio values are indicated in bold and values in bracket are indicated as one standard deviation.

A.3 Multiple Linear Regression (MLR) for SPR, AR and Dilution

A.3.1 Semi-penetration Ratio (SPR)

The MLR equation for SPR is given in Equation A1. The predicted SPR values were plotted vs. the measured values, as shown in Figure A1. A relatively low value of R^2 (67.4%) indicated the MLR prediction did not fit SPR model. Test 8 value does not follow the fit, but the complementary results (triangles) fit good.

$$SPR = 0.076 + 0.274 \cdot HIL - 0.20 \cdot VL + 0.20 \cdot TS \quad (A1)$$

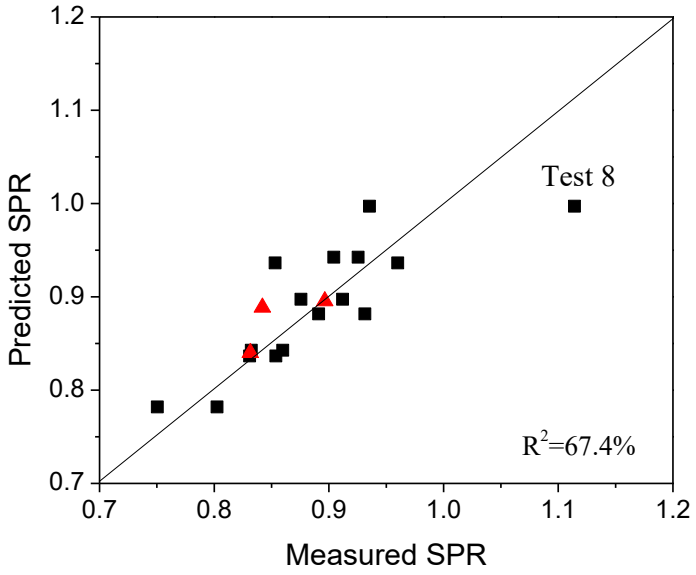

Figure A.1 Measured and predicted values for SPR.

A.3.2 Aspect Ratio (AR)

The MLR equation for AR is given in Equation A2. The predicted AR values were plotted vs. the measured values (Figure A2). A similarly low value of R^2 (72.6%) with SPR model indicated the MLR prediction for AR model is less precise. Test 8 value is not close to the ideal trend line (the straight line) in both Figures A1 and A2, which indicates the Test 8 value appears to be an outlier for bead ratio model.

$$AR = -0.091 + 0.41 \cdot HIL + 0.44 \cdot HIT - 0.041 \cdot VL + 0.021 \cdot TS \quad (A2)$$

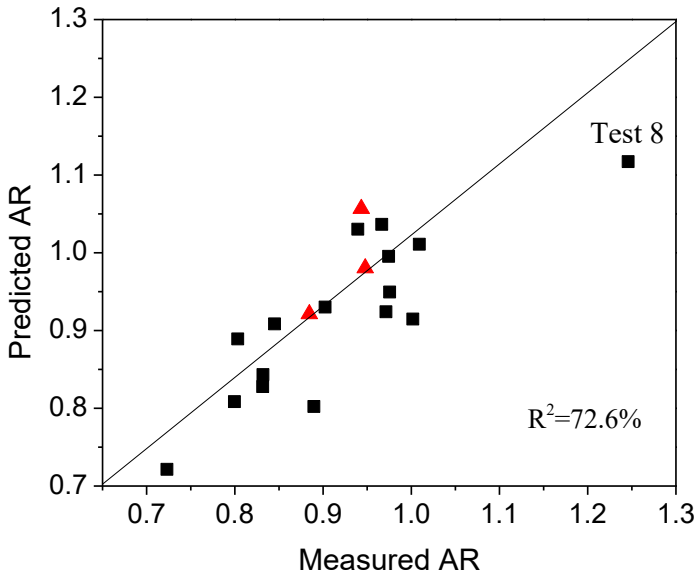

Figure A.2 Measured and predicted values for AR.

A.3.3 Dilution

The MLR equation for dilution is given in Equation A3. The predicted dilution values were plotted vs. the measured dilution values (Figure A3). The MLR prediction for dilution model is less accurate due to the relatively low value of R^2 (68.1%). The complementary results do not fit the trend line in Figure A3.

$$\text{Dilution} = 0.27 + 0.11 \cdot \text{HIL} + 0.006 \cdot \text{VT} \quad \text{(A3)}$$

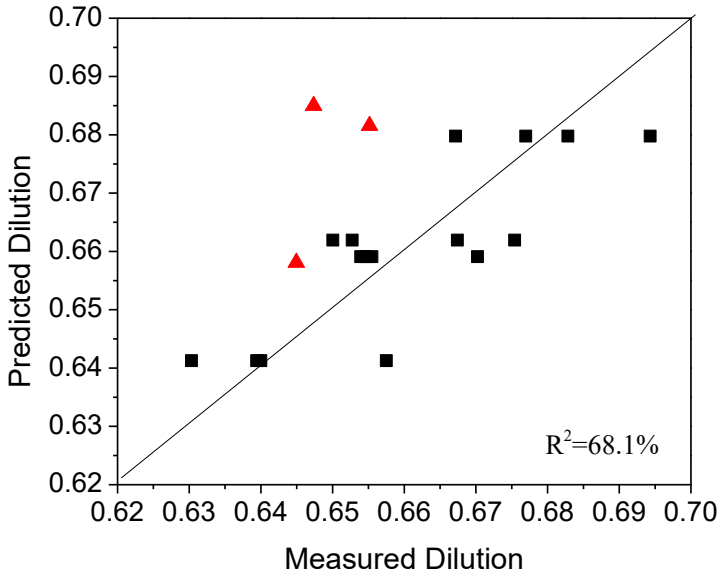

Figure A.3 Measured and predicted values for dilution.

A.4 Three Order Multiple Regression Analysis (TOMRA)

TOMRA analyzed the effect of the statistically significant parameter and interactions of those parameters on the response factors (geometry characteristics and micro-hardness profiles). The developed empirical equations predicted the geometric characteristics and micro-hardness profiles following the form in Equation A4.

$$y = C_0 + \sum_{i=1}^{7}(C_i \cdot x_i) + \sum_{i=1}^{7}(C_{ii} \cdot x_i^2) + \sum_{i=1}^{7}\sum_{i>j}^{7}(C_{ij} \cdot x_i \cdot x_j) + \sum_{i=1}^{7}(C_{iii} \cdot x_i^3) + \sum_{i=1}^{7}\sum_{j>i}^{7}\sum_{k>j}^{7}(C_{ijk} \cdot x_i \cdot x_j \cdot x_k) \quad \text{(A4)}$$

where y is the response factors (geometry characteristics and micro-hardness profile) which were predicted by the controllable variables x_i (welding parameters) and different interactive combinations; C_i, C_{ii}, C_{ij}, C_{iii}, and C_{ijk} are the coefficients in the empirical equations. TOMRA equations for HRA, RA, CGHAZ area, SPR and the WM and CGHAZ micro-hardness are shown in Equations A5 to A9.

$$\text{CGHAZ micro-hardness} = 112 + 1.86\cdot \text{CWFS} + 298\cdot \text{HIL} - 13.31\cdot \text{VL} + 1.44\cdot \text{TS} - 0.0327\cdot \text{CWFS}^2 - 5.89\cdot \text{HIL}\cdot \text{TS} + 0.264\cdot \text{VL}\cdot \text{TS} + 0.000169\cdot \text{CWFS}^3 \quad \text{(A5)}$$

$$\text{WM micro-hardness} = 18 - 0.398\cdot \text{CWFS} + 137\cdot \text{HIT} + 11.79\cdot \text{VT} - 4.02\cdot \text{TS} + 0.00251\cdot \text{CWFS}^2 - 8.02\cdot \text{HIT}\cdot \text{VT} + 3.12\cdot \text{HIT}\cdot \text{TS} \quad \text{(A6)}$$

$$\text{HRA} = -284 + 9\cdot \text{VL} + 8\cdot \text{VT} + 29\cdot \text{BD} - 0.3\cdot \text{VL}\cdot \text{VT} - 0.9\cdot \text{VL}\cdot \text{BD} - 0.8\cdot \text{VT}\cdot \text{BD} - 0.002\cdot \text{HIL}\cdot \text{VT}\cdot \text{BD} + 0.02\cdot \text{VL}\cdot \text{VT}\cdot \text{BD} + 0.004\cdot \text{CWFS}\cdot \text{HIT}^2 + 0.00003\cdot \text{CWFS}\cdot \text{BD}^2 + 0.4\cdot \text{HIL}^2\cdot \text{HIT} \quad \text{(A7)}$$

$$\text{RA} = 61 - 0.014\cdot \text{HIL}\cdot \text{VL}\cdot \text{BD} + 0.021\cdot \text{HIT}\cdot \text{TS}\cdot \text{BD} - 0.0013\cdot \text{VT}^2\cdot \text{BD} \quad \text{(A8)}$$

$$\text{CGHAZ Area} = 0.56 + 8.2\cdot \text{HIL}\cdot \text{HIT} + 0.9\cdot \text{HIL}\cdot \text{BD} + 0.9\cdot \text{HIT}\cdot \text{BD} - 0.78\cdot \text{HIL}\cdot \text{HIT}\cdot \text{BD} - 0.0006\cdot \text{VL}\cdot \text{VT}\cdot \text{BD} \quad \text{(A9)}$$

The significant parameters and interactions in Equations A5 to A9 were selected based on the level of significance (P value of 90% confidence level) using Minitab 19. The remaining parameters and interactions for each geometric result were eliminated due to the statistically insignificance. The calculated values for HRA, RA, CGHAZ area, micro-hardness of CGHAZ and WM are plotted against the observed values, as shown in Figure A4. The observed correlations for geometric results exhibited the better fit than the trend in CGHAZ and WM micro-hardness profiles. Overall, the range of R^2 value is from 81.6% to 97.9% which indicates the precise prediction of TOMRA with less error for each observed trend (Figure A4).

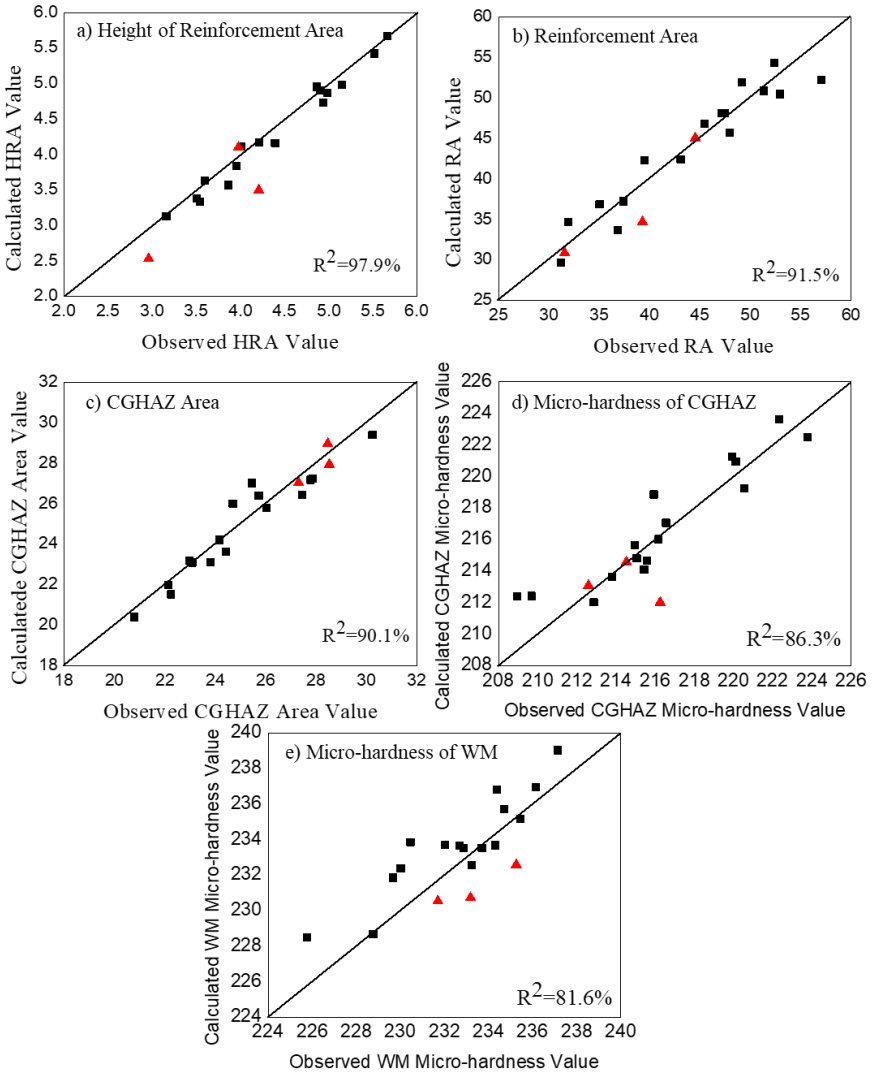

Figure A.4 Observed and calculated values for the (a) HRA, (b) RA, (c) CGHAZ area, (d) micro-hardness of CGHAZ and (e) micro-hardness of WM with the complementary tests results (triangles).

A.5 Effective Contribution

The effective contribution of each parameter depended on the sum of squares which was the deviations from the total average value of population. The effective contribution is calculated by Equation A10.

$$\text{Ƥ}\% = \frac{SS_i}{SS_t} \cdot 100\% \qquad \text{(A10)}$$

where Ƥ is the percentage contribution of each parameter to the response characteristics and SS_i and SS_t are the sum of squares for each parameter and the total sum of squares, respectively. The contribution evaluated the importance of parameters on each weld characteristic and the WM and CGHAZ micro-hardness. The significant contribution for each weld measurement is shown in Figure A5.

The effect of BD on the CGHAZ, BTA, RA, and HRA, exhibited an approximate 50% effective contribution. Conversely, the BW, AR, SPR and dilution shown less contribution (< 5%). This part of the results provides a quantitative assessment for both statistically significant and insignificant parameters, which is consistent with the discussion in Chapter 4.

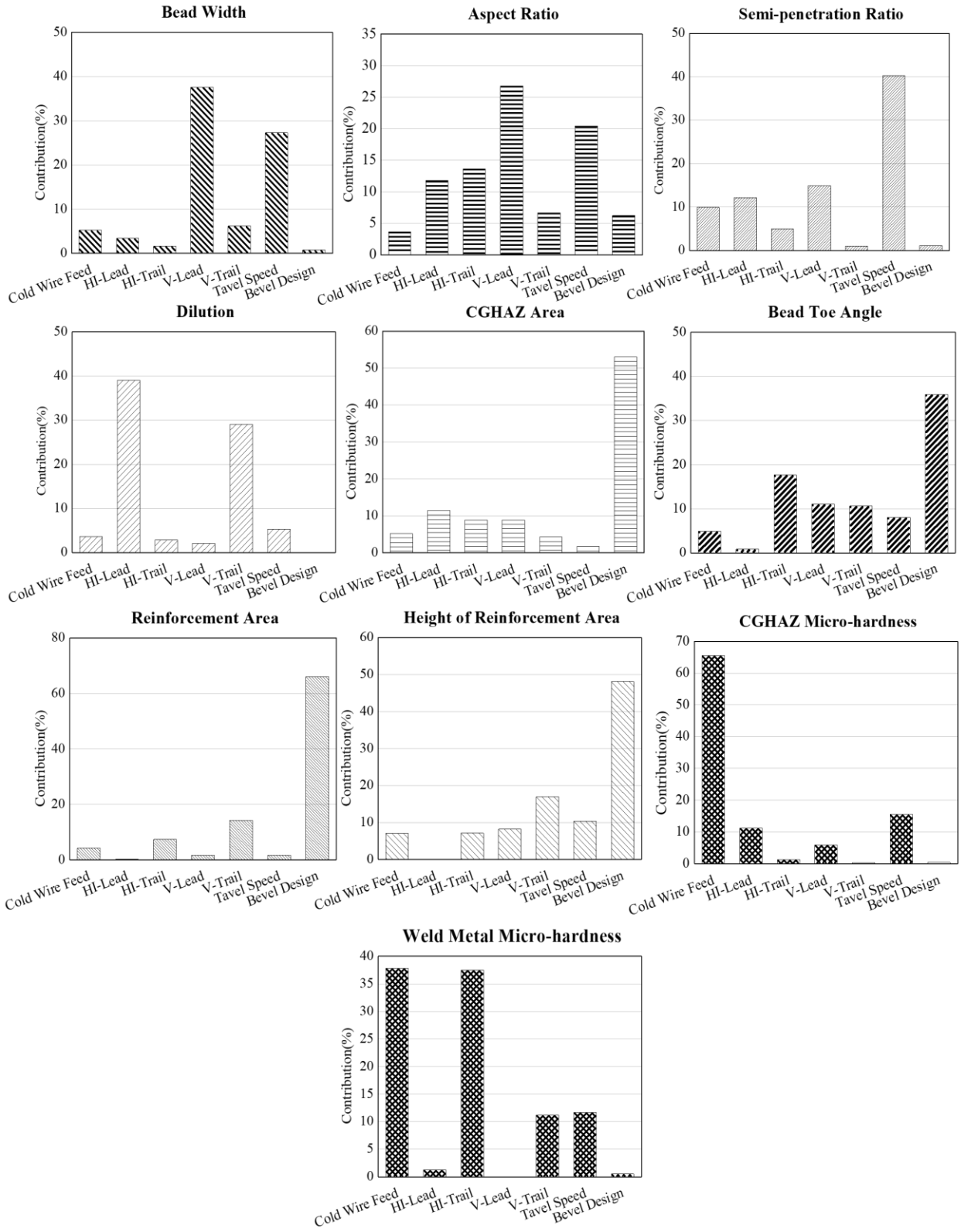

Figure A.5 Effective contribution of CWTSAW process parameters for geometric characteristics, dilution and the WM and CGHAZ micro-hardness.